

SAND 93-7041

GRI-93/0119

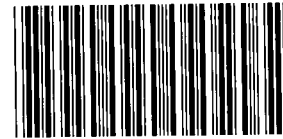


RECORD COPY
C.1

Annual Report

Development of Stimulation Diagnostic Technology

Prepared by:
Sandia National Laboratories



8595225

SANDIA NATIONAL
LABORATORIES
TECHNICAL LIBRARY

Gas Research Institute

Tight Sands and Gas Processing Research Department
February 1993

118p.

GRI-93/0119

SAND93-7041

DEVELOPMENT OF STIMULATION DIAGNOSTIC TECHNOLOGY

ANNUAL REPORT
(January 1991-December 1992)

Prepared by
N. R. Warpinski, J. C. Lorenz,
G. E. Sleaf and B. P. Engler

Sandia National Laboratories
Division 6114
P.O. Box 5800
Albuquerque, New Mexico 87185

For
GAS RESEARCH INSTITUTE
Contract No. 5089-211-2059

GRI Project Manager
Steve Wolhart
Tight Gas Sands Field Evaluation

February 1993

REPORT DOCUMENTATION PAGE	1. REPORT NO. GRI 93/0119	2.	3. Recipient's Accession No.
4. Title and Subtitle Development of stimulation diagnostic technology		5. Report Date 3/10/9 Preparation	6.
7. Author(s) N.R. Warpinski, J.C. Lorenz, G.E. Sleafie & B.P. Engler		8. Performing Organization Rept. No. SAND 93-7041	
9. Performing Organization Name and Address Sandia National Laboratories Division 6253 P.O. Box 5800 Albuquerque, New Mexico 87185		10. Project/Task/Work Unit No.	11. Contract(C) or Grant(G) No. (C) 5089-211-2059 (G)
12. Sponsoring Organization Name and Address Gas Research Institute 8600 Bryn Mawr Avenue Chicago, Illinois 60631		13. Type of Report & Period Covered Annual Report	
15. Supplementary Notes Second annual report for this project		14.	
16. Abstract (Limit: 200 words) <p>To apply Sandia's expertise and technology towards the development of stimulation diagnostic technology in the areas of in situ stress, natural fracturing, stimulation processes and instrumentation systems. The approach to stimulation diagnostics is to integrate in situ stress measurements (including microfracs, anelastic strain recovery, circumferential velocity analysis, and coring-induced fractures) with natural fracture characterization, stimulation analyses (including Fracpro, other models, finite-element analyses, and various pressure analyses), and fracture diagnostics in order to validate hydraulic fracture concepts, models and diagnostic capabilities. The focus of this year's efforts has been on the planning and development of the M-Site experiment facility for hydraulic fracture diagnostic development. A microseismic suitability test was conducted at the site with very positive results. In four small fracture treatments, over 1000 microseisms were recorded, with most of these events having analyzable polarization and p- and s-wave arrivals. In the area of in situ stress, comparative studies are being made to evaluate stress measurement techniques, and an in situ stress topical report is being prepared. Natural fracture studies of the Frontier formation are progressing; the genesis and stratigraphic controls on two fracture sets have been hypothesized.</p>			
17. Document Analysis a. Descriptors <p>Tight gas sands, hydraulic fracturing, in situ stress, natural fractures, fracture diagnostics, fracture modeling</p> b. Identifiers/Open-Ended Terms <p>anelastic strain recovery, circumferential velocity analysis, Frontier formation, coring induced fractures, hydraulic fracture pressure analysis, seismic fracture diagnostics, electrical fracture diagnostics, inclinometer fracture diagnostics</p> c. COSATI Field/Group			
18. Availability Statement Release unlimited	19. Security Class (This Report) unclassified	21. No. of Pages	
	20. Security Class (This Page)	22. Price	

GRI DISCLAIMER

LEGAL NOTICE This report was prepared by Sandia National Laboratories as an account of work sponsored by the Gas Research Institute (GRI). Neither GRI, members of GRI, nor any person acting on behalf of either:

- a. Makes any warranty or representation, express or implied, with respect to the accuracy, completeness, or usefulness of the information contained in this report, or that the use of any apparatus, method, or process disclosed in this report may not infringe privately owned rights; or
- b. Assumes any liability with respect to the use of, or for damages resulting from the use of, any information, apparatus, method, or process disclosed in this report.

Title	Development of Stimulation Diagnostic Technology
Contractor	Sandia National Laboratories GRI Contract Number: 5089-211-2059
Principal Investigator	N. R. Warpinski
Report Period	January 1992-December 1992 Annual Report
Objective	To apply Sandia's expertise and technology towards the development of stimulation diagnostic technology in the areas of in situ stress, natural fracturing, stimulation processes and instrumentation systems.
Technical Perspective	Large quantities of natural gas exist in low permeability reservoirs throughout the US. Characteristics of these reservoirs, however, make production difficult and often uneconomic. Matrix rock permeabilities are often submicrodarcy, and natural fractures are commonly marginal, being anisotropic and easily damaged. Stimulation is required for these types of reservoirs, with hydraulic fracturing being the primary stimulation option. Understanding stimulation behavior is difficult, however, because of the complex nature of most of these reservoirs. Integrating knowledge of the matrix rock, natural fractures, in situ stresses with stimulation models and diagnostics is required if stimulation effectiveness is to be determined and enhanced.
Results	A major focus has been on initial planning for the M-Site experiment, where hydraulic fracturing will be evaluated and design models and fracture diagnostics will be validated and improved. Important issues have been defined and new diagnostics, such as inclinometers, identified. An initial suitability test has been conducted and all results are positive. In the area of in situ stress, circumferential velocity analysis is proving to be a useful diagnostic for stress orientation. A catalogue of techniques, with their capabilities and limitations is being prepared. Natural fracture studies of the Frontier formation are progressing; two fracture sets have been found and their relation to tectonic events have been hypothesized. The results of the Fracture Propagation Modeling Forum have been compared and an SPE paper written.

**Technical
Approach**

The approach to stimulation diagnostics is to integrate in situ stress measurements (including microfracs, anelastic strain recovery, circumferential velocity analysis, and coring-induced fractures) with natural fracture characterization, stimulation analyses (including Fracpro, other models, finite-element analyses, and various pressure analyses), and fracture diagnostics in order to validate hydraulic fracture concepts, models and diagnostic capabilities. To do this effectively, Sandia will participate with other GRI contractors on appropriate field experiments.

TABLE OF CONTENTS

1.0	RESEARCH OBJECTIVES	1
2.0	SUMMARY OF ALL PREVIOUS WORK PERFORMED	3
3.0	SPECIFIC OBJECTIVES OF THE CURRENT YEAR	4
4.0	WORK PLANS FOR THE CURRENT YEAR	5
5.0	IN SITU STRESS	6
5.1	Anelastic Strain Recovery (ASR) Analyses	6
5.2	Circumferential Velocity Anisotropy (CVA) Analyses	8
5.3	Overcoring of Archived Core	10
6.0	NATURAL FRACTURES	11
6.1	Fractures in the Frontier Formation, Western Edge...	11
6.2	Observations on Core from the UPRC Fabian Ditch...	15
6.3	Relationship between Natural Fractures & Diagenesis	16
6.4	Green River Basin Field Trip	19
7.0	STIMULATION	20
7.1	Fracture Propagation Modeling Forum	20
8.0	M-SITE EXPERIMENT	24
8.1	Site Location	24
8.2	Site Advantages	24
8.3	Site Suitability Experiment	25
8.4	Fracturing Services	25
8.5	Planning	26
9.0	FRACTURE DIAGNOSTICS FIELD EXPERIMENTS	27
9.1	M-Site Suitability Tests	27
9.2	Part A - Background Noise and Wellbore Condition	27
9.3	Part B - Microseismic Monitoring	29
9.4	Number of Signals Observed	30
9.5	Maps of Microseisms	31
9.6	Description of Microseisms	31
9.7	Spectral Content of the Microseisms	34
9.8	Conclusions of Seismic Suitability Assessment	34
9.9	Recommendations for Future Monitoring	34
10.0	OTHER DIAGNOSTIC ACTIVITIES	36
11.0	REFERENCES	37

12.0	MAJOR ACHIEVEMENTS	38
13.0	MAJOR PROBLEMS	39
14.0	CONCLUSIONS	40
15.0	OBJECTIVES AND WORK PLANNED FOR NEXT YEAR FIGURES	41

- Figure 1. Fabian Ditch #4-34 ASR sample #1
- Figure 2. Fabian Ditch #4-34 ASR sample #3
- Figure 3. Schematic of microcracks in core
- Figure 4. Ford Motor Co. #80 velocity results, 3367 ft
- Figure 5. Ford Motor Co. #80 velocity results, 3385 ft
- Figure 6. Fabian Ditch #4-34 CVA measurement for ASR sample 1
- Figure 7. Fabian Ditch #4-34 CVA measurement for ASR sample 2
- Figure 8. Fabian Ditch #4-34 CVA measurement for ASR sample 3
- Figure 9. Fabian Ditch #4-34 CVA measurement for ASR sample 4
- Figure 10. Fabian Ditch #4-34 CVA measurement for sample 5
- Figure 11. Fabian Ditch #4-34 CVA measurement for sample 6
- Figure 12. Results of overcoring of archived core
- Figure 13. Map of north-south fractures that intersect a scan line on a bedding surface
- Figure 14. Isopach of Upper Cretaceous strata in, southwestern Wyoming (from Weimer, 1961)
- Figure 15. Strain associated with asymmetric subsidence of Upper Cretaceous strata in southwestern Wyoming
- Figure 16. Strain associated with curvature of basin floor due to lithospheric flexure
- Figure 17. Deposition and burial of the Frontier Formation relative to episodes of thrusting. Thrust timing from Wiltschko and Dorr, 1983
- Figure 18. Length comparison for 2-D models
- Figure 19. Pressure comparison for 2-D models
- Figure 20. Efficiency comparison for 2-D models
- Figure 21. Length comparison for 3-layer cases
- Figure 22. Height comparison for 3-layer cases
- Figure 23. Pressure comparison for 3-layer cases
- Figure 24. Length vs time for 3-layer Newtonian fluid
- Figure 25. Height vs time for 3-layer Newtonian fluid
- Figure 26. Pressure vs time for 3-layer Newtonian fluid
- Figure 27. Length comparison for 5-layer cases
- Figure 28. Height comparison for 5-layer cases
- Figure 29. Pressure comparison for 5-layer cases
- Figure 30. Length vs time for 5-layer Newtonian fluid
- Figure 31. Height vs time for 5-layer Newtonian fluid
- Figure 32. Pressure vs time for 5-layer Newtonian fluid
- Figure 33. Perforation event - all traces
- Figure 34. Perforation event - hodograms
- Figure 35. Perforation event - all traces, expanded view
- Figure 36. Histogram of events correlated with pressure during breakdown
- Figure 37. Histogram of events correlated with pressure during step-rate test
- Figure 38. Histogram of events correlated with pressure during KCl minifrac
- Figure 39. Histogram of events correlated with pressure during gel minifrac
- Figure 40. Plan view of microseism locations
- Figure 41. Side view of microseism locations
- Figure 42. Microseism traces for event 33, unfiltered
- Figure 43. Hodogram for event 33, unfiltered
- Figure 44. Hodogram for event 33, filtered
- Figure 45. Microseism traces for event 34, unfiltered
- Figure 46. Hodogram for event 34, unfiltered
- Figure 47. Hodogram for event 34, filtered

- Figure 48. Microseism traces for event 4, unfiltered
- Figure 49. Hodogram for event 4, unfiltered
- Figure 50. Microseism traces for event 4, filtered
- Figure 51. Hodogram for event 4, filtered
- Figure 52. Spectral content for event 34, horizontal channel #1 (x)
- Figure 53. Spectral content for event 34, horizontal channel #2 (y)
- Figure 54. Spectral content for event 34, vertical channel (z)
- Figure 55. Spectral content for event 25, horizontal channel #1 (x)
- Figure 56. Spectral content for event 25, horizontal channel #2 (y)
- Figure 57. Spectral content for event 25, vertical channel (z)

TABLES

- Table 1 Rock and reservoir data
- Table 2 Treatment data
- Table 3 2-D results at end of pump
- Table 4 3-layer results at end of pump
- Table 5 5-layer results at end of pump
- Table 6 Receiver (MWX-2) and perforation (MWX-3) locations
- Table 7 Receiver (MWX-3) and perforation (MWX-2) locations
- Table 8 Orientation results for part B
- Table 9 Microseismic distance and orientation results

1.0 RESEARCH OBJECTIVES

The objective of this project is for Sandia National Laboratories to apply its expertise and technology towards the development of stimulation diagnostic technology. Stimulation diagnostic technology, as defined here, contains different areas such as (1) in situ stresses, (2) natural fracture characterization, (3) stimulation modeling, (4) hydraulic-fracture diagnostics, and (5) the design and conduct of field experiments. Integration of these areas can yield a more complete analysis of hydraulic fracture behavior and effectiveness in the reservoir.

In situ stresses, both the direction and the magnitudes, are of vital importance to the production of gas from low permeability reservoirs. Stress data are required for advanced design and analysis of fracture treatments, for completion information, and for understanding of the production mechanisms in tight reservoirs. The specific objective of the in situ stress task is to integrate core, log, and injection stress data into a complete picture of the stress in the reservoir, and to develop a "catalog" of techniques, each with a set of validated procedures, which can be brought to bear on the problem of stress determination.

Many of the tight reservoirs in the US, particularly in western basins, produce primarily from marginal natural fracture systems. Understanding the natural fracture system and the effects of stress, pore pressure, water saturation, etc. are important for any rational decisions on completion and stimulation of wells in these reservoirs. The specific objectives of the natural fracture task are to obtain description and distributions of the fracture systems from core, logs and outcrops, determine the importance of the fracture systems, and integrate these data for use in completion/stimulation design and production operations.

Effective hydraulic fracture stimulation requires a comprehensive design model that can adequately predict fracture behavior and reservoir performance. GRI has such a model (Fracpro) that can be used for design, analysis, and real-time control. Confident use of such models requires validation in realistic physical situations, a difficult task since the created fractures are not very accessible. The specific objectives of the stimulation modeling task are to perform analyses of injections using pressure analyses, finite element models, simple fracture models, and other resources in order to obtain a comparison with Fracpro and to aid in its validation.

Information on fracture behavior is currently available only through the use of indirect fracture diagnostic techniques, but these techniques are far from being routine field procedures, nor do they have the universal confidence of industry. The specific objectives of this task are to examine seismic and electrical diagnostic techniques, develop advanced concepts, and advance the validation of such techniques.

Field experiments are an integral part of GRI's Tight Gas Sand Project and the means by which models, diagnostics, and other procedures can be tested, refined, and verified. The specific objectives of this task are to participate in any constructive capacity in the design and analysis of M-Site experiments, and other future experiments where Sandia capabilities can enhance the results.

2.0 SUMMARY OF ALL PREVIOUS WORK PERFORMED

During the previous year, work efforts focused on (1) the application of core-based methods for in situ stress measurement, (2) the evaluation of natural-fracture systems in the Frontier formation on the Moxa Arch and other locations, (3) analysis and comparison of stimulation models, (4) the design of the Hydraulic Fracture Test Site (HFTS), and (5) development of instrumentation for the HFTS and other experiment locations.

Efforts to develop, apply, and document the basics of core-based stress measurement techniques concentrated on circumferential velocity anisotropy, anelastic strain recovery, overcoring of archived core samples, and coring-induced fractures. Several sets of data were taken and compared during the year.

Evaluation of natural fracture systems occurred at a Davis formation site and the Frontier formation in the Moxa Arch region, which is the primary focal point for this study. Field studies showed that natural fractures in the Frontier at this location have widely varying azimuths.

Stimulation studies and analyses consisted of efforts to publish the results of the Fracture Propagation Modeling Forum and model runs of HFTS parameters.

Much effort was expended for the planning of the HFTS experiment, including a lead role in the modeling R&D team and development of inclinometers for fracture analysis and stress measurement purposes. In addition, data from many sites were analyzed and modeled to assess site suitability.

3.0 SPECIFIC OBJECTIVES OF THE CURRENT YEAR

Specific objectives of the current year are:

1. Investigate the accuracy and reliability of the various stress measurement techniques being used by GRI and industry, as well as new ideas and techniques. This investigation will lead to the compilation of a final report cataloging all of the stress measurement techniques, their specific problems, and their applicability to different rocks and environments.
2. Continue the characterization program of the natural fractures in the Frontier formation near the Moxa Arch area.
3. Provide a neutral analysis of hydraulic fracture stimulations on GRI experiments and document the Fracture Propagation Modeling Forum results.
4. Provide analyses, ideas and concepts of fracture diagnostics for GRI experiments. Areas of interest are seismic and electrical.
5. Provide design and analysis support for GRI experiments, particularly the M-Site experiments.

4.0 WORK PLANS FOR THE CURRENT YEAR

Work plans for the current year are subsets of all five tasks associated with this project. These include:

1. Perform the necessary stress analyses for SFE-4, including anelastic strain recovery, circumferential velocity, microfrac, and any other warranted procedure. Complete a catalogue or user's manual of stress measurement techniques.
2. Perform stress analyses on other cooperative wells as appropriate.
3. Determine natural fracture characteristics from core, log, outcrop, etc. on the Frontier formation or on cooperative wells or other experiments as appropriate.
4. Perform stimulation analyses on designated experiments.
5. Complete a paper documenting the Fracture Propagation Modeling Forum results.
6. Conduct a site suitability experiment at the M-Site location. This suitability test is primarily aimed at determining if the chosen location is suitable for microseismic monitoring.
7. Begin planning for the M-Site experiments, including design and analysis tasks.

5.0 IN SITU STRESS

Knowledge of the directions and magnitudes of in situ stress are of vital importance to the production of gas from low permeability reservoirs. Stress data are used in the design and analysis of hydraulic fracture stimulations and are necessary for the understanding of parameters affecting production. However, in situ stresses are difficult to measure, and there is no commonly accepted practice for determining the stresses. As a result, there is often a lack of confidence in stress data from any one technique. In light of this reality, it is common sense to develop as many ways as possible to determine stress parameters.

Sandia is currently working on integrating information from anelastic strain recovery (ASR), differential strain curve analysis (DSCA), circumferential velocity anisotropy (CVA), coring-induced fractures, log-derived wellbore effects, overcoring of archived core and microfrac stress measurements in order to obtain an integrated program to provide the best possible stress measurement.

Activities during the year centered on the Frontier formation, analysis of Berea core from an eastern well, and overcoring of archived core.

5.1 Anelastic Strain Recovery (ASR) Analyses

The orientation of the maximum horizontal in situ stress, and thus the hydraulic fracture orientation, can often be determined from various types of core analyses. Types of measurements include anelastic strain recovery¹⁻³ (ASR), differential strain curve analysis⁴ (DSCA), and circumferential velocity analysis (CVA). ASR is a particularly appealing technique because it is a measurement of the strain relief of the original in situ stresses due to drilling. Since this strain relief is likely to be an irreversible process, ASR provides the most accurate measurement of this process. DSCA, on the other hand, requires a reapplication of the stresses by some other path, which may lead to inaccuracies in the analysis. CVA is performed after the strain relief is over, and is an indirect measurement of the relaxation. ASR is hindered, however, by the fact that it is a complicated technique that must be carefully performed, analyzed, and diagnosed.

ASR consists of selecting samples at the drill site, instrumenting them with clip-on displacement gages as quickly as possible, and monitoring the subsequent relaxation of the core for 1-2 days. Three gages, spaced 45° apart, are placed around the horizontal plane, while one axial gage is optionally placed on the core. The axial gage serves no purpose for fracture azimuth, but it can be useful for estimating stress magnitudes. One service company uses a 60° spacing for the horizontal gages, which results in a different equation for the fracture azimuth.

The orientation of the maximum stress (the hydraulic-fracture azimuth) is the direction of the maximum strain recovery; recovery occurs due to microcracking in response to the unloading of the in situ stresses. More unloading, and therefore more strain recovery, occurs in the direction of the maximum horizontal stress than it does in the direction of the minimum stress. The direction of the maximum strain recovery can be quickly computed by using the strain-rosette equations, yielding

$$\theta = \frac{1}{2} \tan^{-1} \left[\frac{\varepsilon_{45^\circ} - (\varepsilon_{0^\circ} + \varepsilon_{90^\circ})}{\varepsilon_{0^\circ} - \varepsilon_{90^\circ}} \right]$$

The angle, θ , has to be determined by inspection, as it is always less than or equal to 45° , and it is the angle with respect to the largest of the ε_0 or the ε_{90} strains.

There are many complications that can occur with ASR (or DSCA or CVA), so it should never be used alone. If the rock is extremely tight, pore pressure may be trapped within the sample and cause contractions in the core as it slowly escapes. Pore pressure contractions are usually larger than the strain recovery, and are due to a volumetric shrinkage of the core as the pore pressure is reduced. Pore pressure effects can be accounted for, but they add another uncertainty to the analysis.³

Rock fabric, as due to tectonic cracks, bedding, burrows, and other aligned features, is probably the most serious difficulty in performing these measurements. ASR, DSCA, and CVA will all result in a large response to many types of fabric. In using these techniques, it is always important to inspect the core carefully, both before and after monitoring, to ensure that fabric is not affecting the results. Thin sections can also be useful. Employing more than one these procedures is often a good double check.

5.1.1 Frontier UPRC Fabian Ditch #4-34 tests

Anelastic Strain Recovery (ASR) measurements were made on four samples from the UPRC Fabian Ditch #4-34 well, with two samples taken from each of the longer core runs. Figures 1 and 2 show the raw strain data for the two best sets of data, ASR samples #1 at 11573.5 ft and ASR sample #3 at 11625 ft. In both cases the strains are less than 20 microstrains, which is typical of the electrical and thermal noise that is usually obtained on such an experiment. It is just as likely that the decrease in strain shown in these two figures is due to cooling of the sample as it is to any strain relaxation. Relaxations that are this small should never be considered reliable. Furthermore, the orientation data were useless so a stress orientation can not be calculated.

The main question for this test is why the recovery strains are so small. Strain relaxation is a delicate process that probably occurs as a combination of stress corrosion cracking and relief of pore pressure and surrounding mud pressure. If the core is mishandled or otherwise beaten, the relaxation microcracks tend to release at once and little further recovery occurs. In this case, the core exhibited a tremendous amount of damage due to chattering and spiraling of the scribe knives; in some cases it was so bad that the core was entirely encircled by damage. The only other time that such a battered core has been observed, there was also a total lack of ASR response. As a result of these problems, there were no results obtained from ASR measurements on this well.

5.2 Circumferential Velocity Anisotropy (CVA) Analyses

Measurements of the circumferential velocity anisotropy (CVA) of a core sample are useful indicators of the *in situ* stress orientation or of the rock fabric, if one exists. These measurements were initially used as a diagnostic for strain-relaxation stress-measurement techniques, such as Anelastic Strain Recovery (ASR) and Differential Strain Curve Analysis (DSCA), but they have been found to be useful stress indicators without any other relaxation work.

The theoretical velocity distribution for a preferentially oriented population of microcracks has been worked out by Sayers,⁵ yielding a velocity distribution given by

$$V(\theta) = V_{\text{avg}} + A \cos(2\theta + \varphi) + B \cos(4\theta + \varphi)$$

In this equation, the velocity at any orientation, $V(\theta)$, is a function of the average velocity through the sample plus a 2θ and a 4θ component. The phase angle, φ , is simply the offset angle that makes $V(\theta)$ a maximum at $2\theta + \varphi = 0^\circ$ (assuming B is much smaller than A).

Acoustic waves will be slowed primarily in the direction in which they cross the most cracks. Thus, the orientation of the minimum velocity, $2\theta + \varphi = 180^\circ$, is the direction in which the most cracks are crossed. This orientation of microcracks can now be related to the *in situ* stresses. Since the microcracks are due primarily to relief of the *in situ* stresses, and more microcracks will open up against the largest principal stress, the minimum velocity orientation should be aligned with the maximum stress direction (the hydraulic fracture direction). A schematic of this behavior is shown in Figure 3.

In actual practice there are a number of factors which can cause problems with the CVA technique. In some rocks, there is very little microcrack development, or the microcracks have little effect on the velocity, so that the anisotropy is small. A good example is a high porosity rock, where additional microcracks have a minimal effect on velocity through the highly voided rock. When velocity variations are on the order of 2-3% or less, the inferred stress orientation should be considered unreliable.

A second major problem for the CVA technique is the prior existence of a rock fabric, due to cracks, layering, oriented grains or crystals, or many other factors. Such a fabric can often produce a velocity anisotropy that overwhelms the microcracks velocity anisotropy. However, fabric usually has a completely different velocity character than relaxation microcracks, and this becomes very apparent in fitting the theoretical curve to the data. For relaxation microcracks, the theoretical fit is generally good, and the sinusoidal character of the anisotropy is evident. For the cases with fabric, there is generally a poor fit of the theoretical curve, and the velocity data have a blocky structure. This difference provides a qualitative diagnostic for fabric problems.

A third problem is the damage zone around the core surface, which can often cause significant velocity slowing. Velocity surveys are often run on the as-received core, but if the data are not satisfactory, then the surface of the core is ground down about $\frac{1}{8}$ in and the velocity survey is rerun. This procedure often improves the quality of the data.

5.2.1 Berea Ford Motor Co. #80 tests

Circumferential velocity analyses (CVA) have been conducted on five sandstone cores from the Ford Motor Co. # 80 well. Initially, measurements were made on the as-received core, but there was no significant anisotropy in velocity. This often happens because the outside layer of the rock will have a skin damage due to the cutting process. To remove the skin, all five cores were ground down about $\frac{1}{16}$ in circumferentially, and then they were retested. Three of the samples had a bimodal velocity distribution that is typical of fabric (we also found out later that these three samples do not have orientation information). No further action is contemplated on these three core samples.

One sample, taken from a depth of 3367 ft and shown in Figure 4, had a reasonable response and a minimum velocity orientation of 175° from the principal scribe line (PSL). With the master orientation line (MOL) at 233° at this depth and a MOL and PSL divergence of 24° , the sum of these clockwise rotations gives an azimuth of 72° for the maximum stress.

A second sample, taken from a depth of 3385 ft and shown in Figure 5, has a natural fracture cutting across one edge of the core. This natural fracture has prevented us from obtaining velocity data where the signals have to cross the fracture. Thus, there are no data between about 50° and 100° for this sample. The rest of the data, however, suggest that the minimum velocity orientation is about 170 - 180° ; this is the same orientation as the natural fracture strike (170°). Thus the stress field appears to be aligned with the natural fracture in this core. There is no absolute orientation for the velocity distribution or the natural fracture because there is no orientation data at this depth.

In summary, there is only one sample in which there is good velocity orientation data, and it has an orientation of $N72^\circ E$. However, this technique is only reliable when there are data from a few samples. This core, for example, appears to be from a depth at which a connection was made, as there are two PSL's over about two inches of core and they differ by about 10° . Thus, the orientation on this core sample is accurate to only about ± 15 - 20° . From Figure 4, the velocity azimuth has about the same uncertainty, giving a total uncertainty of 20 - 30° .

5.2.2 Frontier UPRC Fabian Ditch #4-34 tests

Circumferential Velocity Anisotropy (CVA) measurements were performed on all four ASR samples from the UPRC Fabian Ditch #4-34 well, as well as two additional samples.

The CVA results for ASR sample #1 (11571.5 ft) are given in Figure 6. The solid line is the least-squares fit of the theoretical distribution which has a $\cos 2\theta + \cos 4\theta$ form. Although the distribution looks acceptable, the anisotropy is only 2%, an amount that is too small to be certain that the data are reliable. We usually recommend an anisotropy of at least 3%.

The CVA results for ASR sample #2 (11573.5 ft) are shown in Figure 7. In this case the anisotropy is 4%, but the poor fit of the theoretical model is a strong suggestion that the anisotropy is due to fabric.

The CVA results for ASR sample #3 (11624 ft) are given in Figure 8. The anisotropy is only 1% and no information can be obtained.

The CVA results for ASR sample #4 (11625 ft) are shown in Figure 9. There is no anisotropy for this sample.

CVA results were also obtained for samples at 11588.5 ft (sample #5) and 11598.5 ft (sample #6). These are shown in Figures 10 and 11. For sample #5, the blocky structure of the data suggests that fabric is present. There are quite a few cross-beds within that sample that may cause this fabric. The anisotropy for this sample is about 3%. Sample #6 has an anisotropy of about 2% and cannot be used for stress data.

It is curious that the velocity anisotropy from this well is so poor, as sandstone samples from SFE-4 had well-developed anisotropy. It is quite possible that the battering of the core was so severe that many grain boundaries were damaged, not just those that would have cracked due to stress relief alone. The end result would be very little anisotropy and no information on stress orientation.

5.3 Overcoring of Archived Core

Several overcore tests of archived core were conducted in 1992 in an attempt to develop a technique to use archived core for stress measurements. The final test in the series used a sample from SFE-4 that also had an ASR test and a velocity anisotropy measurement conducted on it. A careful test procedure was followed, with temperature compensation on the strain gages in order to look for a time-dependent response, as well as the initial elastic response. Figure 12 shows the results of the elastic response compared to the velocity data. On this sample, the velocity data showed that the maximum stress orientation, the fracture azimuth, was N20°E. The elastic response shows a minimum in strain recovery at N112°E, or a maximum at N22°E. Thus, the maximum strain recovery again lines up with the hydraulic fracture azimuth.

We obtained considerable time-dependent strain recovery, which is consistent with the elastic data, but it will require additional effort to determine if the time-dependent response is in any way related to magnitudes of stress.

6.0 NATURAL FRACTURES

Many of the tight sandstones, particularly those in western U.S. basins, have matrix permeabilities of a few microdarcies or less. Economic production from such reservoirs is impossible unless natural fractures or other mechanisms provide additional permeability. Well testing of many of these microdarcy or submicrodarcy reservoirs often yields effective permeabilities of tens or hundreds of microdarcies, substantiating the hypothesis that most of these reservoirs are fractured. Outcrop, log and core studies have also shown the presence of natural fractures. Knowledge of the characteristics and importance of the natural fractures is important because it may affect the stimulation or other completion plan.

6.1 Fractures in the Frontier Formation, Western Edge of the Green River Basin, Wyoming

6.1.1 Field Observations

The Frontier Formation is fractured in all outcrops exposed near Kemmerer, Wyoming. Field work suggests that there are at least three sets of regional fractures present. Any or all fracture sets may occur at any given outcrop. Where abutting relationships can be measured, a roughly north-south trending fracture set is the first-formed set. These fractures are present in most outcrops, and are the most common ones. Mapping of bedding surfaces (Fig. 13) shows fractures that are relatively planar, and that probably do not interconnect except across minor en echelon offsets along individual fracture trends. Fracture spacing may vary from outcrop to outcrop, from bed to bed, and even within a bed. Observed average fracture spacing in different outcrops ranges from a low of only a few inches between fractures, to a high where few fractures are present in the outcrop. Fracture swarms occur locally, commonly within beds where there are few fractures outside of the swarm. Many of the fracture planes terminate vertically against, or are offset by, sedimentary heterogeneities within the sandstones.

The younger fracture sets trend approximately east-west and northeast-southwest. They commonly terminate or are slightly offset against fractures of the north-south set, although locally they carry straight across the first-formed fractures. There are also outcrops which contain only the younger east-west fracture set, with little or no indication of previous north-south fracture-forming stress.

All of the regional fracture sets are apparently independent of and predate the folding of the strata. However, there are several examples of small-scale shear offset and of slickensided fracture faces that suggest local reactivation of fractures during structural deformation. Local fracture sets in the more intensely deformed strata (which dip up to 90° and are even slightly overturned in places), may be related to structural deformation.

Fractures farther south, in the structurally more complex area of Coalville, Utah, display a commensurately more complex pattern. Deciphering the fracture history of this particular area will be a slow and painstaking exercise.

6.1.2 Modeling Basin Stresses and Fracture Formation

The Frontier outcrops studied are situated within and at the eastern edge of the Idaho-Wyoming fold and thrust belt. A fold and thrust belt is created by lateral compression, and fracture sets can be formed parallel to strong compression.⁶ Therefore it was not initially apparent why the first-formed fractures in the Frontier sandstones should trend north-south, since these fractures strike normal to the most obvious source of lateral compression and thus to the fracture trend one would predict from a cursory analysis.

However, these strata were deposited in a section of the Cretaceous foredeep that had a smaller width-to-depth ratio than most of the basins adjacent to the fold and thrust belt. Isopachs (Fig. 14) show that over 18,000 ft of Upper Cretaceous strata were laid down in a basin that was only 40 miles from edge to depocenter.^{7,8} As the basin subsided, strata were stretched in the east-west direction due to lengthening during asymmetric subsidence. During this process, the east-west compressive stress was diminished. (An actual tensile stress was not created, but rather the compressive stress in this direction was decreased as lateral elongation of the strata east to west occurred).

The strata were lengthened east to west during burial and asymmetric subsidence, and this lengthening can be modeled as the lengthening of the leg of a triangle as it is stretched to the length of the hypotenuse (Fig. 15). A critical strain of about 0.3% and a stress of about 200 MPa are necessary to fracture similar sandstones under laboratory conditions. However, under true geologic conditions, slow strain rates, stress corrosion, elevated temperatures, etc.), strata will fracture at lower stress levels especially if formation pore pressures were high. Burial rates of at least 200 m/m.y. were common for the thickened strata in this basin, and elevated pore pressures were probably common.

If subsidence is modeled as a triangle, an east-west strain of just over 0.2% is calculated in the Frontier strata by the end of Cretaceous time. However, the hypotenuse of the triangle, along the line of the subsiding strata, was not a straight line. Because the lithosphere was being elastically flexed by the weight of the overlying thrust plates, it bowed upward in front of the thrust, adding a curvature component to the lengthening of the line and thus to the strain. This component of strain can be calculated to be about 0.06% (Fig. 16). This lengthening, added to the lengthening due to stretching of the leg of the triangle, becomes a total strain of at least 0.26%, or nearly the amount of strain needed to fracture samples in the laboratory. In the absence of other complications, this 0.26% strain would probably be sufficient to have caused north-south fractures in the Frontier under geologic conditions.

East-west tectonic compression associated with the fold belt probably tended to decrease the east-west basin-subsidence strain at some stratigraphic levels, while at the same time adding a component of north-south extensional strain. However, thrusting was not a continuous event. Rather, several major thrust events took place during and after deposition of the Frontier Formation (Fig. 17, with individual thrust events given by the first letter of their names, as in reference 11), with episodes of continued subsidence between events. Moreover, thrust-induced stress may not have been applied uniformly to the vertical stratigraphic column: most stress was applied to the shallower strata as new thrust sheets formed. Deeper strata below the main decollement were probably subject to a lesser, drag-induced stress from the overriding thrust plate.

Therefore, the stress conditions at the western edge of the Green River basin varied significantly with time. During active thrusting, north-south extension associated with east-west

compression was dominant, and locally was of sufficient magnitude to create east-west fractures. Between thrust events the lithosphere adjusted isostatically and flexurally to the supracrustal thrust-sheet loads by rapid subsidence at the edge of the thrust. During this time, east-west extension was the dominant strain. From the evidence of the dominant north-south fracture system, east-west extension must have been more common, and often of greater magnitude, than north-south extension, but local exceptions occurred.

Another factor, the full significance of which has not yet been fully evaluated, is the presence of the Uinta Mountain thrust system along the southern margin of the Green River basin. The amount of northward thrusting, and thus the magnitude of the north-south stress system imposed on the strata in the basin by the thrusting, is unclear. However, the timing of thrusting, (late Campanian to early Paleocene⁹), was concurrent with, and the stresses derived from thrusting were aligned with, the maximum burial/asymmetric-subsidence stresses described above.

The Uinta Mountain thrust system is a deep-seated, "thick-skinned" thrust system (as compared to the "thin-skinned" fold and thrust system to the west), and the stresses derived from it were apt (1) to have been of significant magnitude, and (2) to have affected strata to a significant depth in the adjacent basin. Therefore, stresses from this source may have controlled fracturing in the deeper, more central parts of the Greater Green River basin, locally overwhelming the shallower, fold-and-thrust-belt derived compressive stresses from the west.

Evidence for this seemingly implausible switching of stresses over relatively short distances and/or time periods may be present in the variability of fracture patterns. As described, north-south fractures are the most common, and are the first-formed set where present. However, east-west fractures are also found (1) without associated north-south fractures, and (2) crossing north-south fractures with little indication of any interaction. This suggests that different stratigraphic layers were susceptible to fracturing at different times, due to variable conditions of pore pressure, cementation, etc. Moreover, the times at which different layers were fracture-susceptible apparently coincided with different events of east-west and north-south strain.

Hansen and Bonilla¹⁰ suggested that a similar duality of contemporaneous stress orientations (also of latest Cretaceous age), is recorded by the larger structures at the northern edge of the Uinta Mountains. In this area, north-south compression is indicated by the Uinta thrust fault that forms the northern boundary of the Uinta Mountain block. However, penecontemporaneous east-west compression is also suggested by north-south trending anticlines in the Mesozoic strata north of this fault, and by probable left-lateral offset along the fault.

The rapid switching of regional Laramide stress fields and tectonic plate motions to produce such an anomalous record is improbable. Rather, we suggest that both the east-west compressive stress produced by the fold and thrust belt, and the north-south compressive stress driving the Uinta Mountain thrust, were ultimately derived from the same, uniform, plate-scale tectonic system. Relatively minor readjustments of the position and attitude of the fault-bounded Uinta Mountain tectonic block, in response to the prevailing, probably east-west regional stress field, led to (1) northerly thrusting along the Uinta Mountain thrust, (2) indentation of the Uinta Mountain block into Mesozoic strata at the southern edge of the Green River basin, and ultimately, (3) a derivative but significant north-south compressive stress in the local strata. This occurred contemporaneously with east-west compression derived from

the fold and thrust belt. Thus the relative magnitudes of the east-west and north-south horizontal stresses in the basin at any time were probably a function of the relative rates of tectonic activity in the two areas.

Frontier strata near Kemmerer have been folded, transported 10-12 miles eastward, and exposed by erosion since deposition and burial. This may account for some cross fracturing normal to the regional sets, local structurally-produced fractures, and some reactivation of the regional fractures in shear. In fact, it is probably remarkable that a more complex fracture pattern is not present in these strata.

Many of the north-south fractures might be inferred to be hinge-line fractures, produced by flexure at the hinges of the large scale folds, except that the folds are box folds and the fractures occur on the limbs, not at the crests or troughs of folding. Moreover, the fractures commonly strike 10-20° oblique to a fold axis, and do not change strike in sympathy with changes of fold-axis strike. Therefore, this possibility is discounted as a general explanation for the observed outcrop fracture patterns.

6.1.3 Summary

The field work and modeling to date have suggested a plausible mechanism to explain the observation of apparently anomalous north-south, first-formed regional fractures, in sandstones of the Frontier Formation at the eastern edge of the fold and thrust belt of western Wyoming. These fractures are inferred to be the product of east-west extension during rapid and anomalously deep subsidence in the narrow foredeep basin. Stresses in this orientation are likely to have been enhanced by deep-seated indentation stresses derived from the Uinta Mountain thrust system to the south. Secondary east-west fractures resulted from intermittent east-west compressional stress, related to the fold and thrust belt to the west. Such secondary fractures were apparently formed slightly later than, but locally nearly contemporaneously with, the north-south fractures.

6.1.4 Utility

According to this model, subsurface Frontier reservoirs from the Moxa Arch west should contain dominant north-south fractures, and locally, subordinate east-west fractures. Subsurface data available at present (e.g., the SFE 4 well), are not conclusive due to core orientation ambiguities. Our knowledge of the present in situ stress state is also incomplete. Since stresses will control the relative permeability of the different fracture systems, it is difficult to predict which fracture system is the best target for deviated drilling. However, if horizontal stresses are isotropic, areas where both fracture sets are present would be the best targets.

East of the Moxa Arch, east-west fracturing or north-south fracturing may predominate in the subsurface in the absence of local structure, depending on the relative magnitudes and depths of effectiveness of the stresses derived from the various compressive stress sources in and around the basin. The westward thrusting of the Rock Springs Uplift will have complicated the local stress/fracture pattern.

6.2 Observations on Core from the UPRC Fabian Ditch #4-34 Well

Although scribe-line control and the orientation survey were not consistent enough to provide the detailed stress information that were desired from this core, several observations are worth reporting.

The demarcation between the upper fluvial and lower marine facies is picked at 11,594.5 ft depth. Above this depth, the fluvial facies is heterogeneous, with abundant sub-horizontal bedding discontinuities and much shale. Below, the marine interval is more homogeneous, although it still displays three distinct depositional facies and contains three thin horizontal clay-drape heterogeneities, potential barriers to vertical matrix and/or fracture permeability, within the 32 ft cored.

The major gas show on the mud log correlates exactly with a 23-ft thick interval of completely burrowed, fine to medium-grained marine sandstone that extends from 11,611-11,634 ft. (Although the base of the core is at 11,628 ft, the bottom of the zone is placed at 11,634 ft from both coring rates and high gas-volumes shows; thus 11,634 ft is most likely the base of the interval).

What is of interest is that this facies is commonly not fractured in outcrop examples, presumably because burrowing has mixed ductile clays and organic components with the sand, allowing ductile rather than brittle (fracture) deformation of such units. Thin sections will be made of the core and of the outcrop sandstones in order to decide whether this comparison is real or only apparent, and thus to predict whether this gas-bearing facies would be expected to be fractured in the subsurface despite the apparent absence of fractures in this core.

The ASR samples were taken from this interval because it is relatively homogeneous and because it was the last unit cored (the ASR measurement is time-dependant). The absence of a measureable ASR response also argues for a relatively ductile rock. The velocity anisotropy samples, however, were taken from sandstones containing little clay, and when tested may indicate more definitive stress-related responses, if a stress anisotropy is in fact present at depth.

If this facies is ductile and therefore not fractured, gas recovery from this unit will be dependant entirely on its porosity and permeability, which will be presented in the final core report by Terra Tek.

A similar facies (the 5.5 ft between 11,601.5 and 11,606 ft) was not associated with mud-log gas or rapid coring rates, perhaps because the interval is somewhat finer grained and not as heavily burrowed. This interval and the seven feet of overlying well-sorted sandstone are more likely to contain fractures, but are apt to have lower matrix porosity and permeability. Therefore the mud log would not have recorded a gas show across this interval unless a significant fracture was actually intersected.

A preliminary conclusion would be that the marine interval that is not associated with the most significant mud-log gas shows (11,594.5-11,606 ft) would be the best candidate for a hydraulic fracture stimulation. In this interval, there is a better chance for the existence of natural fractures, and therefore for intersecting those fractures with a stimulation fracture. The obviously gas-prone, heavily burrowed interval from 11,610-11,634 ft may produce of its own accord.

6.3 Relationships between Natural Fractures and Diagenesis

As noted earlier, there are several different fracture trends in outcrops of the Frontier Formation in the Green River basin.¹¹ Adjacent beds locally even contain different fracture sets. The reason(s) for this are not immediately apparent: bed thickness, structural context, and depositional environment have been considered as possible controlling factors, but none of these factors have presented consistent relationships with the varying fracture orientations.

A plausible relationship exists between fracture orientation and the petrophysical properties of the rock, properties which controlled the susceptibility of the rock to fracturing through time, and which are in turn a product of its diagenetic history. Petrologic study shows that similar petrophysical properties in different depositional facies resulted from parallel diagenetic sequences. On the other hand, in several cases different diagenetic sequences apparently produced similar rock properties, and hence similar fracture characteristics within otherwise disparate rocks.

The correlation between fracture properties and diagenetic facies may provide a predictive tool for the subsurface evaluation of natural-fracture potential in reservoirs, even if core from wells did not intersect fractures for direct evaluation. This can be illustrated with core from the Union Pacific's Fabian Ditch #4-34 well.

Samples from a limited number of sandstones from Frontier outcrops, and from different depositional environments and different fracture facies, were thin-sectioned and compared petrographically for this study. Probable petrophysical properties were inferred from this examination. Actual petrophysical properties might eventually be measured in the laboratory to give definitive correlation points, although many of the inferred properties were time- and history- dependant and cannot be measured in the present-day rock.

6.3.1 Diagenesis and Fracture Facies

Outcrop examination suggests that north of Kemmerer, WY, there are four separate fracture facies in local sandstones of the Frontier Formation. These are:

1. Beds containing north-trending fractures
2. Beds containing northeast-trending fractures
3. Beds containing both of the above sets of fractures
4. Beds without significant fracturing

Within each separate group, grain size, sorting, depositional environments, and porosity vary enough that none of these factors alone is likely to account for the observed differences in fracture orientations. Moreover, mineralogic composition of the sand grains in all of the sandstones is similar, thus grain composition is unlikely to be a controlling factor.

The most important variable within the samples seems to be the diagenetic sequence, including several types and episodes of cementation and dissolution. However, matrix material such as clays and organic components that were introduced during initial deposition may be contributing factors.

6.3.1.1 Fracture Facies 1

Rocks containing primarily north-trending fractures consistently exhibit evidence for early quartz cementation by silica overgrowths on quartz grains and later dissolution of much of the silica phase, leaving a relatively high-porosity rock. In contrast to other fracture facies, there is little evidence for a later calcite cementation phase within rocks of this group.

This observation is consistent with the proposed origin of the north-trending fractures early in the history of the strata.¹² Early silica cementation would have created brittle properties in the rocks, making them susceptible to fracturing contemporaneously with east-west extension of the strata during subsidence, and creating an essentially north-south fracture set.

The absence of the younger, north-east trending fracture set in these strata may then be attributed to non-brittle properties during later, thrust-related stress events. Relative ductility resulted from the dissolution of much of the early silica, combined with the absence of the later calcite cementation phase.

6.3.1.2 Fracture Facies 2

Rocks containing only the north-east trending fractures display the inverse diagenetic sequence, displaying little or no evidence for the early silica cementation phase, but commonly containing significant amounts of later calcite cementation. Calcite fills most of the porosity of these samples. Thus these samples are inferred to have been poorly cemented and relatively ductile during the stress phase which locally resulted in north-trending fractures, yet they were brittle and susceptible to fracturing during the later stress episodes that produced north-east trending fractures.

6.3.1.3 Fracture Facies 3

This facies characteristically contains both the older north- and the younger northeast-trending fracture sets. Thus it is not surprising to find that the samples from this facies typically display both the early silica and later calcite cement phases (separated by the silica dissolution phase). These samples are inferred to have been brittle due to cementation during both stress phases. These rocks also have relatively low porosity.

Depositional environment may have influenced the diagenetic sequence to a degree; commonly these samples are from the cleaner depositional facies such as the hummocky cross-stratified shallow marine/lower shoreface facies where clays were rarely deposited. However, the sands include significant amounts of rock fragments, and were never clean orthoquartzites.

No natural fractures were intersected by the core from the Fabian Ditch 4-34 well. However, thin sections of the unburrowed, hummocky cross-bedded sandstone core from this well are petrographically similar to the outcrop sandstones that contain fracture facies 3. Therefore it is probable that this facies is fractured in the subsurface, and that the core merely missed the reservoir fractures.

6.3.1.4 Fracture Facies 4

This "fracture facies" is characterized by the general absence of fractures in outcrop, and includes rocks from a diversity of depositional facies. Notably, it includes sandstones that

were deposited in the same environment as the hummocky strata noted in group 3, but which were subsequently intensely burrowed, mixing a significant percentage of rock fragments, organic material, and primary clay into the resulting rock. It also includes thick, white, amorphous sandstones believed to be upper shoreface deposits. The porosity of these samples ranges from very low to very high.

The apparent ductility of some of these samples probably derives from the mixture of clay and organic material into the sandstone, whereas in others it may be due to a high percentage of ductile rock fragments that comprise the sand fraction. In still another example, ductility may be attributed to a very high porosity (30%), and the resulting limited grain to grain contact. In the Fabian Ditch #4-34 well, samples from two depositional facies probably fall into this group, one from a burrowed, shallow-marine environment, and the other from the fluvial depositional environment. In the former case, ductile rock fragments are common, and in the second case, grain to grain contacts are commonly buffered by intergranular detrital clay. Thus there appears to be a range of diagenetic sequences that produced rock properties that were not susceptible to fracturing, although these strata account for a small percentage of the Frontier Formation.

6.3.2 Conclusions

There are three diagenetic sequences in the Frontier Formation sandstones that seem to correlate with age and orientation of fracture sets seen in outcrops: 1) north-south fractures occur in sandstones that were cemented early with silica and that did not undergo later calcite cementation; 2) northeast fractures occur in sandstones that were not cemented with the early phase of silica overgrowths but that contain the later calcite cement; and, 3) both fracture sets are found in sandstones that contain both cementation stages. Finally, depositional environment operated to supply some of the sandstones, such as the heavily burrowed shallow marine and the fluvial deposits, with significant components of ductile material, and little fracturing took place in these rocks.

Similar diagenetic sequences occur in sandstone cores from the subsurface. It is suggested that, by analogy, the petrologic character of the sandstones may be used to infer probable fracture characteristics in the natural gas reservoirs despite the failure of the core to intersect fractures.

6.4 Green River Basin Field Trip

An oral presentation on the characteristics and origin of fractures in the Frontier Formation, co-authored by Laubach and Lorenz, was given at the Rocky Mountain Section meeting of the AAPG on September 15th in Casper, WY. A paper on the same topic was published in the Wyoming Geological Association 1992 Guidebook. This guidebook accompanied a field trip, held after the meeting, which examined the characteristics of the Frontier Formation where it outcrops around the edges of the Green River Basin. The outcrops that we have studied for fractures in this program were highlighted stops during the trip.

7.0 STIMULATION

Some form of stimulation, usually hydraulic fracturing, is required for the economic production of gas from tight reservoirs. A long-sought objective has been comprehensive hydraulic-fracture models that could be used for the design, analysis, and, ultimately, real-time control of the fracturing process. In order to help validate such comprehensive models, Sandia is tasked to (1) analyze appropriate field stimulation and minifrac data in order to obtain an independent assessment of fracture performance, and (2) conduct any advanced activities (e.g., finite element analyses, model comparisons, etc.) which provide independent confirmation of model validity. One of the primary activities of this task for 1992 was the compilation of Fracture Modeling Propagation Forum results

7.1 Fracture Propagation Modeling Forum

The primary tasks associated with the forum were to (1) compile and compare the varied model results that were developed at the forum, (2) prepare an SPE paper summarizing those results, and (3) prepare a GRI topical report that gives all of the calculated model output. Since all of the results are in a separate topical report, only a brief summary is included here.

7.1.1 Purpose

The study is a comparison of hydraulic-fracture models run using test data from the GRI Staged Field Experiment No. 3. Models compared include 2-D, pseudo-3-D, and 3-D codes, run on up to eight different cases. Documented in this comparison are the differences in length, height, width, pressure and efficiency. The purpose of this study is to provide the completions engineer a practical comparison of the available models so that rational decisions can be made about which model(s) is optimal for a given application.

7.1.2 Model Data and Test Cases

The relevant rock and reservoir information are shown in Table 1. Three different physical configurations were considered: a single layer, three layers, and five layers. Stress and rock property measurements were averaged over the appropriate depths for each interval to yield the physical data given in Table 1. Most importantly, the stress contrasts range from 1450-1650 psi, although the lower barrier is only 40 ft thick for the five layer configuration. Young's modulus and Poisson's ratio were obtained from sonic measurements, thus accounting for the elevated values of Young's modulus. Treatment data are shown in Table 2.

There were a total of eight possible cases each participant could model if they so chose. These were GDK, PKN, 3-layer, and 5-layer cases with separate runs for a constant Newtonian viscosity and a constant n' and k' power-law fluid. The PKN and GDK cases were run with a constant height (2-D) set at 170 ft. The 3-layer and 5-layer cases were run using a 3-D or a Pseudo-3-D model allowing fracture height to be determined by the model. Of particular interest was if the fracture broke through zone 4 in the 5-layer case.

Table 1 Rock and Reservoir Data

Interval	Depth (ft)	Zone Thickness (ft)	In Situ Stress (psi)	Poisson's Ratio	Young's Modulus	Frac Toughn \sqrt{i}
Single-Layer (2-D) Case						
1	9170-9340	170	5700	0.21	8.5×10^6	20
3-Layer (3-D) Case						
1	8990-9170	180	7150	0.30	6.5×10^6	20
2	9170-9340	170	5700	0.21	8.5×10^6	20
3	9340-9650	310	7350	0.29	5.5×10^6	20
5-Layer (3-D) Case						
1	8990-9170	180	7150	0.30	6.5×10^6	20
2	9170-9340	170	5700	0.21	8.5×10^6	20
3	9340-9380	40	7350	0.26	5.4×10^6	20
4	9380-9455	75	5800	0.20	7.9×10^6	20
5	9455-9650	195	8200	0.30	4.0×10^6	20

Table 2 Treatment Data

Bottom-hole temperature	246° F
Reservoir pressure	3600 psi
Spurt loss	0.0
Fluid leakoff height	entire fracture height
Fluid leakoff coefficient	$0.00025 \text{ ft}/\sqrt{\text{min}}$
Viscosity - Case A	200 cp
Viscosity - Case B	$n' = 0.5; K = 0.06$
Fluid volume	10,000 bbls
Injection rate	50 bpm
Proppant	none

7.1.3 Results

The complete set of results for the final fracture geometry from these model runs are shown in Tables 3-5 for the 2-D, 3-layer, and 5-layer cases respectively. Most of the results are based on the data in these tables. In addition, some time dependent results will be given in figures.

7.1.3.1 2-D Results

Considering first the 2-D results given in Table 3, the final half length for all of the 2-D models are shown in Figure 18. The well-known difference in length estimates between the PKN and GDK models is evident in these results, but some differences between different models in each group become apparent. Presumably, this difference is because of other options included in some models. The effect of the different rheologies is generally small. Besides the PKN and GDK models, GOHFER and ENERFRAC-1 and -2 are also shown.

The reduction in length between ENERFRAC-1 and ENERFRAC-2 is due to increased tip overpressure. Likewise, the reduction in length between MEYER-1 and MEYER-2 is due to options that were included in MEYER-2 which reflect the designers' incorporation of more complex physics into the fracturing process.

Table 3 2-D Results at End of Pump

200 CP	MODEL	LENGTH	HEIGHT	PRESSURE	W MAX	W AVG W	W AVG F	EFFIC
	SAH (GDK)	2542	170	62	0.848	0.849	0.605	85.5
	SAH (PKN)	4855	170	1094	0.502	0.394	0.289	72.3
	MARATHON	2584	204	1685	0.91	0.76	0.73	93
	MEYER1(GDK)	2659	170	70	0.79	0.79	0.62	83.1
	MEYER1(PKN)	4507	170	1188	0.55	0.43	0.32	72.2
	MEYER2(GDK)	2288	170	97	0.94	0.94	0.74	85.4
	MEYER2(PKN)	3803	170	1474	0.68	0.53	0.4	76.6
	SHELL(GDK)	2724	170	53	0.78	0.78	0.61	84
	SHELL(PKN)	4039	170	1377	0.59	0.46	0.37	75
	TEXACO-FP	1898	200	131.9		1.06		94.4
	TEXACO-FP	3587	200	1377		0.72		90
	CHEV(GDK)	1347	170	81.9	0.77	0.77	0.6	81.9
	CHEV(PKN)	2029	170	1380	0.63		0.36	73
	ADVANI	4595	170	1182	0.54	0.43	0.32	73.8
	HALLIB	2212	170	82	0.98	0.98	0.77	85.9
	CONOCO(GDK)	2716	170			0.767	0.6	82.5
	CONOCO(PKN)	3986	170			0.554	0.37	74.4
	ENERFRC-1	3866	170	1595	0.627	0.492	0.387	75
	ENERFRC-2	3556	170	1684	0.704	0.553	0.434	78
n', k'	MODEL	LENGTH	HEIGHT	PRESSURE	W MAX	W AVG W	W AVG F	EFFIC
	SAH (GDK)	2542	170	61.8	0.85	0.85	0.6	61.8
	SAH (PKN)	4629	170	1167.5	0.54	0.42	0.28	73.6
	MARATHON	2516	204	1824	0.98	0.82	0.75	93
	MEYER1(GDK)	2098	170	117	1.04	1.04	0.82	86.4
	MEYER1(PKN)	4118	170	1397	0.64	0.5	0.36	74.3
	MEYER2(GDK)	1808	170	161	1.24	1.24	0.97	88.3
	MEYER2(PKN)	3395	170	1774	0.81	0.64	0.46	79
	SHELL(GDK)	2142	170	89	1.03	1.03	0.81	89
	SHELL(PKN)	3347	170	1754	0.75	0.59	0.47	79
	ADVANI	4046	170	1474	0.68	0.53	0.38	76.9
	HALLIB	2031	170	97	1.07	1.07	0.84	86
	CONOCO(GDK)	2304	170		0.933	0.933	0.733	85.2
	CONOCO(PKN)	3656	170			0.622	0.415	76.5
	ENERFRC-1	3396	170	1880	0.738	0.58	0.456	78
	ENERFRC-2	3155	170	1986	0.817	0.641	0.504	81.7

Table 4 3-Layer Results at End of Pump

200 CP	3-LAYER							
	MODEL	LENGTH	HEIGHT	PRESSURE	W MAX	W AVG W	W AVG F	EFFIC
	SAH	3408	318	1009	0.65	0.35	0.3	77
	NSI	3750	903	283	0.56	0.32	0.25	66
	RES	1744	544	1227	0.9	0.54	0.36	80
	MARATHON	1360	442	1387	1.04	0.68	0.64	96
	MEYER-1	3549	291	987	0.58	0.35	0.29	70.3
	MEYER-2	2692	360	1109	0.72	0.41	0.34	74.3
	ARCO-STIM	3598	306	992	0.57	0.31	0.25	67
	TEXACO-FP	836	740	1561		1.333		89
	ADVANI	2089	357	1113	0.66	0.33	0.25	43
n', k'	3-LAYER							
	MODEL	LENGTH	HEIGHT	PRESSURE	W MAX	W AVG W	W AVG F	EFFIC
	SAH	3259	371	1093	0.75	0.38	0.31	77.6
	NSI	3289	329	1005	0.67	0.35	0.26	68
	RES	902	596	1428	1.1	0.74	0.49	62
	MARATHON	1326	442	1433	1.08	0.71	0.66	96
	MEYER-1	2915	337	1094	0.69	0.4	0.32	72.7
	MEYER-2	2120	413	1212	0.86	0.48	0.4	76.9
	ARCO-STIM	3235	353	1083	0.65	0.33	0.26	69
	ADVANI	2424	435	1171	0.74	0.34	0.21	47

Table 5 5-layer Results at End of Pump

200 CP	5-LAYER							
	MODEL	LENGTH	HEIGHT	PRESSURE	W MAX	W AVG W	W AVG F	EFFIC
	SAH	2905	394	960	0.72	0.42	0.31	80.1
	NSI	3709	361	852	0.63	0.38	0.25	66
	RES	1754	501	1119	0.83	0.6	0.4	82
	MARATHON	1224	476	1250	1.03	0.7	0.65	97
	MEYER-1	2962	328	669	0.5	0.36	0.28	70.5
	MEYER-2	2407	327	768	0.6	0.46	0.35	74.8
	ARCO-STIM	3399	394	944	0.64	0.36	0.24	68
	TEXACO-FP	934	605	934		1.32		89.6
	ADVANI	1594	438	1129	0.81	0.45	0.36	58.1
n', k'	3-LAYER							
	MODEL	LENGTH	HEIGHT	PRESSURE	W MAX	W AVG W	W AVG F	EFFIC
	SAH	2642	430	1035.5	0.82	0.46	0.31	81.8
	NSI	2765	388	935	0.71	0.42	0.25	70
	RES	1042	600	1358	1.18	0.9	0.6	87
	MARATHON	1156	476	1262	1.04	0.71	0.66	93
	MEYER-1	2535	330	766	0.6	0.46	0.37	73.7
	MEYER-2	1980	349	891	0.75	0.57	0.42	77.8
	ARCO-STIM	2926	405	968	0.7			70
	ARCO-TF	3124	449	1160	0.74			62
	TEX-FP	1089	578	1365		1.19		88.5
	TX-FPTIP	1168	614	1285		1.077		87.7
	ADVANI	1870	458	1151	0.85	0.47	0.34	64

The net pressures for the 2-D models, shown in Figure 19, follow a similar pattern to length, with the GDK models giving low pressures and the PKN models providing high net pressures. GOHFER is different in that it predicts short lengths, like the GDK models, but high pressures like the PKN models. The efficiencies for the 2-D calculations are shown in Figure 20. Values ranged from 70-95%.

7.1.3.2 3-Layer results

The 3-layer results (Table 4) show considerably more variability than the 2-D cases. In Figure 21, the fracture half length varies from less than 1000 ft for FRACPRO to greater than 3000 ft for the conventional pseudo-3-D models. The differences between MEYER-1 and -2 again show that the options available to the analyst can have a significant effect on the results. Many such options have probably been employed on the other models, but were not identified as such for this comparison.

The favorable comparison between ARCO and NSI running Stimplan, and a similar favorable comparison between TEXACO and RES running FRACPRO, show that consistent results can be obtained from a given model even if run by different organizations.

The fracture height comparison, given in Figure 22, shows that much greater height growth is obtained by FRACPRO than by other models. Net pressures, shown in Figure 23, are particularly high in FRACPRO and GOHFER. Efficiencies vary from 40% to greater than 95%, as given in Table 4.

Also of interest are the length, height, and pressure development with time, as shown in Figures 24-26 for the non-Newtonian rheology case. Height growth is extremely fast in FRACPRO, but much better contained in most of the other models.

7.1.3.3 5-Layer results

The 5-layer results (Table 5) are similar to the 3-layer comparison, except that the length in some models is shorter because the height breaks through the lower barrier. The half lengths are shown in Figure 27 and the fracture heights are given in Figure 28. Net pressures range from nearly 700 psi to greater than 1400 psi, as shown in Figure 29. Efficiencies range from about 60% to 97%.

Fracture lengths as a function of time are shown in Figure 30. The length development in this case is not uniform because height breakthrough into the lower barrier limits growth in some of the models. The height growth is shown in Figure 31 and the net pressure in Figure 32. By comparing these results with the 3-layer results of Figures 24-26, the effect of breakthrough into the lower low-stress region can be seen.

7.1.4 Discussion of results

The completion engineer now has a wide array of hydraulic models available for both design and analysis of hydraulic-fracture treatments. However, these models calculate widely different fracture geometries for the same input parameters, and it becomes

important to choose a model that meets the needs of that particular engineer. It is hoped that this comparison study provides sufficient information to make a studied choice.

It is clear that there are some models that predict results that are significantly different from the majority. Considering the 5-layer cases shown in Figures 27-29, FRACPRO calculates very short fracture lengths and high net pressures and large height. GOHFER also predicts short fracture lengths and high net pressures, but the height growth is not as severe. TRIFRAC, STIMPLAN, TERRAFRAC, and MFRAC-II are all in general agreement, with longer fractures, less height, and somewhat lower net pressures. Advani's model is midway between the two end cases.

MFRAC-II (in 2-D, 3-layer and 5-layer cases), ENERFRAC (in 2-D cases), and Texaco's FRACPRO cases (5-layer) were run in two different modes and thus provide a useful assessment of the importance of the options that are available to the fracture designer. In the original formulation of this study, the modelers were asked to run their models in both a base mode (no options) and then with a best-option mode, that is, a mode that reflected their expectations of the options needed to provide the closest simulation of true fracture behavior. Such options may have included tip effects, higher frictional pressure drops in the fracture, multiple fracture strands, enhanced toughness, or others.

In the three cases mentioned above, the modelers provided such a comparison, and these results can be used to estimate how significantly the engineer can modify the fracture design by trying to incorporate his estimate of the "best physics" possible for a given reservoir. Presumably, such an estimate would be guided by experience with the reservoir. For the 5-layer case with non-Newtonian viscosity, "best physics" results differed by about 22% for MFRAC-II, and 7% for FRACPRO run by Texaco. For the 2-D case with non-Newtonian rheology, ENERFRAC results differed by about 7%. Since many models have such options, these results should be a useful guideline for estimating the differences in model designs that can be obtained.

The 2-D models, both PKN and GDK, generally provide self-consistent results (Figures 18-20), and the differences between these types of models has been discussed in prior publications.^{13,14} Chevron's 2-D model, however, yields considerably shorter lengths than the other PKN and GDK models. GOHFER is also of note because it yields a length typical of the GDK models with the net pressure of the PKN models. Other differences in these 2-D models are minor.

This particular case was chosen because it was a realistic field situation for which detailed data were available. The committee and the modelers all recognize that other formations, with different stress and lithology data, may provide a considerably different comparison of the models. Good examples would be cases where there are minimal stress contrasts and where the stress contrasts are extremely large. It would be beneficial if future model comparison studies investigated those cases as well.

Finally, in assembling this comparison, the study committee has purposely attempted to avoid making any value comparisons between the various models. Thus, only the results and quantifiable comparisons (e.g, model A frac length is greater than model B frac length) are given.

7.1.5 Conclusions

A comparison study of many of the available hydraulic fracture models has been completed. This study provides information on the relative differences in the model for this one particular case.

These comparisons show that differences in calculated fracture lengths can be large, as much as a factor of three. Fracture heights, for the multi-layer cases can differ by more than 50%. Net pressures also differ by a factor of two.

Comparison runs of the same model with different options give a useful comparison of the importance of all of the additional physical mechanisms that are continuously being added to the models to explain the wide variety of pressure responses observed in different reservoirs. Such options give the completions engineer considerable flexibility, but also difficult choices of when various options should be used.

8.0 M-SITE EXPERIMENT

Three of the primary goals of GRI's tight-gas-sand program are (1) validation of hydraulic-fracture design models, (2) development of hydraulic-fracture length diagnostics, and (3) validation of all fracture-diagnostic technology. Validation implies a confirmation of the predicted results by actual measurement in the field, and thus requires an instrumented facility where fracture behavior can be measured. The effort to develop such a capability is named the M-Site Experiments. Sandia has been involved (along with CER Corp. and RES) with the definition of the test plan and the choice of a suitable location.

8.1 Site Location

The location for the first M-Site experiment is at the former Multiwell Experiment and Slant Hole Completion Test site in the Piceance basin near Rifle Colorado, using the CER MWX-2 and CER MWX-3 wells. There are two thick, untested intervals at approximately 4300 and 4500 ft depth that are optimum for hydraulic fracture validation experiments. In addition, a thinner interval at about 4900 ft has been selected for some initial suitability tests. Based upon previous work performed by Sandia (in conjunction with CER Corp., for DOE), these sands have reasonable stress contrasts (500-1500 psi), are low permeability, have small gas saturations (up to 20%), and are fairly continuous, particularly the upper sand. Such conditions are exactly the ones required for an optimum test site.

8.2 Site Advantages

In addition, there are several technical advantages associated with this site, based upon previous work. These include:

1. This is an established site with at least two wells available;
2. If a third well is needed, it does not have to be an expensive treatment well.
3. It is a site where it is already proven that microseismic signals will be generated-- thus, there is low technical risk on diagnostic issues.
4. There is extremely close spacing for high quality diagnostics.
5. The zones are shallow enough for tiltmeters and for electrical diagnostics.
6. The stress azimuth is already known; there are no questions about where to site wells or instrumentation.
7. Natural fractures are present, but mostly below 5500 ft.
8. Fracpro was run on the Fluvial E experiment at 5530 ft, so there is preliminary information on model behavior.
9. Through work in 10 separate intervals, there is absolutely no sign of any near-wellbore effects during fracturing experiments. Thus, fracture interpretation is simplified.
10. There are multiple intervals, some with water, some with less than 30% gas saturation..
11. The site is in an active producing and drilling area, and within an active and producing reservoir (fluvial Mesaverde).
12. The wells are available indefinitely; there is no rush to get on production.
13. There are thick extensive sandstone reservoirs in the upper fluvial and paralic.
14. Detailed rock properties and reservoir properties are already available.
15. Full core was taken through this zone in MWX-1. The core is stored at Sandia

8.3 Site Suitability Experiment

Because of the expensive nature of GRI's M-Site program, it was decided that site suitability could best be assured through an initial experiment to determine if the current wellbores were usable, if the site was sufficiently quiet for microseismic monitoring, if microseismic signals would be generated in sufficient numbers during a fracture treatment, and if the pressure behavior of the treatment was normal.

CER Corp prepared the site for diagnostic use and a fracture treatment, while Sandia contracted out for fracturing services and prepared an advanced seismic receiver for microseismic monitoring. The suitability tests were conducted in two parts during September and October of 1992. Details of these tests are given in section 9.0.

In summary, the results of the suitability tests were all positive; this is considered to be an excellent site for development and validation testing.

8.4 Fracturing Services

Sandia contracted with The Western Company for fracturing services for the M-Site suitability testing. The following summary describes the services that were obtained.

The fracturing service company was on site for approximately 2 days to perform the following operations:

1. Breakdown/ballout of 72 perforations using approximately 70 bbls of 40# cross-linked gel and ± 100 7/8-in ball sealers;
2. 100-bbl KCl step-rate injection (0.5-20 bpm rates) with extended shut-in period for closure measurements (1 hour shut-in period);
3. 300-bbl KCl minifrac at 30 bpm rate with extended shut-in (2-4 hrs);
4. 475-bbl minifrac using a 40# linear gel, pumped at a rate of 30 bpm with extended shut-in (2-4 hrs).

In addition, the service company provided the following data on the fracture treatment:

1. treatment pressure;
2. treatment rate;
3. fracturing Quality Control (e.g., base gel characteristics, volumes pumped, gel break times, etc.)

Finally, the site operator provided bottom-hole pressure data to the fracturing service company. The service company then integrated the bottom-hole pressure data with the other treatment data (as given in the above section) and returned all data to the site operator for use in real-time fracture analysis of the injections.

8.5 Planning

As a result of the positive suitability tests, planning for the M-Site experiments has begun. The most emphasis has been put on the design of the offset monitor well and the design of the overall data acquisition for the experiment. These efforts are just beginning this year.

9.0 FRACTURE DIAGNOSTICS FIELD EXPERIMENTS

An objective of this project is to develop new or improved capabilities for fracture diagnostics. The primary activity this year was the fielding of an advanced seismic receiver in the M-Site suitability tests.

9.1 M-Site Suitability Tests

The diagnostic part of the M-Site suitability experiment was conducted in two parts during September 21-23, 1992 and October 13-15, 1992. The purpose of these two sets of tests was to confirm that A) the background noise levels and the current wellbore conditions were acceptable for microseismic diagnostics experiments and B) analyzable microseisms would be generated in sufficient numbers during fracturing experiments so that hydraulic fracture geometry could be determined as a part of any experiment test plan.

In order to accomplish these objectives, a new generation seismic receiver, developed by Sandia, was fielded. Current seismic receivers used by industry exhibit significant resonances above about 200-400 Hz. The new receiver was designed using modal analysis and advanced accelerometer technology with the result that no resonances below 2000 Hz are present and the electronic noise floor is extremely low. This receiver provided a signal quality that is superior to any results obtained previously with a wireline receiver.

Part A consisted of background monitoring and mapping of perforations to determine if the site and the existing wellbores were adequate. Part B consisted of microseismic monitoring during a series of hydraulic fracturing tests, including a breakdown injection, a step-rate/shut-in test, a KCl minifrac and a linear-gel minifrac. All injections were conducted in MWX-3 while monitoring in MWX-2.

One decision was made prior to these tests that affected the type of results that could be obtained. Because of limited resources, a gyro-orientation tool was not coupled to the receiver, and therefore the receiver orientation would need to be determined by analyzing the polarization of perforations in an offset well. Thus, there is no absolute ground truth for the orientation and the total uncertainty of any event location will be unknown. Nevertheless, it was expected that the orientation uncertainty would be less than $\pm 10^\circ$.

9.2 Part A - Background Noise and Wellbore Condition Test

During the week of September 21, 1992, the first part of the suitability test was conducted. The two important questions to be addressed were 1) was the ambient noise level at the site (primarily due to production in two other wells on location) low enough that microseisms could be detected, and 2) were the current wellbores (MWX-2 and MWX-3) in sufficiently good shape that seismic signals would not be distorted or attenuated by poor cement bonding or behind-pipe gas bubbling (in microannuli).

On September 22, 1992, the seismic receiver was placed in MWX-2 at a depth of 4800 ft and a background noise test was performed. Although some 60 cycle noise problems

were occurring, the general noise background was about -150 db relative to $1 \text{ g}/\sqrt{\text{Hz}}$, extremely quiet compared to past microseismic experiments.

It should be noted here that there was a depth shift problem that was not reconciled until after these MWX-2 tests were completed. An uncertainty in depth in MWX-2 arose after apparently tagging bottom at what was thought to be 5006 ft. Although the wireline depth registered 4908 ft when bottom was apparently tagged, it was suspected that the depth counter on the 7-conductor wireline may not have been accurate. As a result, all receiver depths in this well were set at 100 ft + the wireline depth. However, after this series of tests was completed, other tools were run in the hole and it was determined that there was likely an obstruction in MWX-2 just below 4900 ft and the wireline depth was essentially correct. Thus all receiver locations in this well were incorrectly set 100 ft higher than actually desired.

With the receiver set at 4800 ft (and not 4900 ft, as desired), small decoupled perforations (about 3.5 gm) were shot in MWX-3 at several depths, as shown in Table 6, and the signals were detected with the receiver in MWX-2. During these tests, the sampling rate was 0.25 msec, which should have been sufficient for signal frequencies in the 400 Hz range, the frequency range typical of most previous microseismic experiments. The perforation shots were clearly seen in MWX-2.

Table 6 Receiver (MWX-2) and perforation (MWX-3) locations

Receiver Depth (ft)	Perforation Depth (ft)
4800	4900
4800	4950
4800	5000
4800	4850
4800	4800
4800	4750
4800	5050
4440	4540
4200	4310
4200	4360

The seismic energy associated with the perforations exhibited a broad band energy spectrum from 200 Hz to 1500 Hz (1500 Hz was the maximum capability of the recording system used on this test). Figure 33 shows an example perforation from the shot at 4900 ft with the receiver at 4800 ft. This figure includes traces from each of the accelerometers, with all three channels are scaled by the same factor. The first arrival of the p-wave is clear, and the primary energy is arriving on the y channel. Figure 34 shows an overlay of the two horizontal channels and the polarization plot, indicating the relative orientations in the horizontal and vertical planes. The hodogram clearly shows that the y channel is pointing almost directly at the incident signal. Thus, the orientation of the y channel is north, which is the orientation of MWX-3 (the perforation well) relative to MWX-2.

The only problem with these data is that the sampling rate is too slow relative to the event spectral content. Figure 35 shows an expanded view of the three separate channels. It can be seen in this figure that most cycles have only three-five points; this limited number of points is particularly a problem in the polarization plots where the hodogram of the first one or two cycles is used to determine orientation. (After the first cycle or two, other reflected, refracted, shear, or tube waves may begin to interfere.) Typically, only 6-10 points can be used for polarization analysis, which limits our ability to generate full statistics. Nevertheless, the available data shows 1) that the initial cycles of the events are highly polarized, so that event orientation can be determined, and 2) the first arrivals have a high signal-to-noise ratio.

The shear wave from these perforations is not easily determined, as can be seen in Figures 33-35, but this difficulty is probably a function of the source, rather than the medium, the receiver wellbore, or the receiver itself. The perforation was purposely decoupled from the wellbore to avoid putting holes in the pipe. As a result, shear waves are only formed by conversion when the fluid compressional wave inside the wellbore strikes the pipe, cement annulus, and rock. It is not expected that this shear wave would necessarily be distinct under such conditions.

On September 23, 1992, the configuration was switched, with the receiver run in MWX-3 and the perforations shot in MWX-2. Table 7 shows the shot and receiver locations for these tests. Results from this reverse configuration were essentially the same as the first case, with either MWX-2 or MWX-3 appearing to be acceptable for monitoring.

Table 7 Receiver (MWX-3) and Perforation (MWX-2) locations

Receiver depth (ft)	Perforation depth (ft)
4935	4995
4935	4975
4935	4955
4935	4935
4935	4915
4935	4895
4935	4875
4540	4540
4310	4310
4310	4310

In summary, part A of the suitability tests showed that the ambient noise levels at the site were low, that both MWX-2 and MWX-3 wellbores were suitable for microseismic monitoring, that clear first arrivals and well-defined polarizations could be obtained, and that higher sampling rates would be needed for the microseismic monitoring.

9.3 Part B - Microseismic Monitoring

The microseismic monitoring part of the experiment was conducted on October 13-16, 1992. The receiver was placed in MWX-2 at a depth of 4900 ft, just above the C sand, and several 3.5-gm decoupled perforations were shot in MWX-3 to orient the tool.

Perforation hodograms were similar to those observed in Part A, with the y channel again pointing nearly north. Table 8 gives the receiver depths and perforation depths during orienting. The first three depths did not provide acceptable quality microseisms, so the tool was moved and reclamped until a suitable location (4881 ft) was found.

Table 8 Orientation depths for Part B

Receiver Depth (ft)	Perforation Depth (ft)	Comments
4910	4910	Poor Hodogram
4897	4910	Poor Hodogram
4901	4910	Poor Hodogram
4881	4910	
4881	4970	Perforation Misfire
4881	4940	
4881	4880	
4881	4840	
4881	4810	
4881	4970	

Prior to monitoring microseisms during the minifracs, breakdown and step-rate tests, a new recording system (Sony audio-digital cassette recorder) with a greater bandwidth (0-5000 Hz) and dynamic range (90 db) was purchased. Microseismic activity was monitored continuously on this system (no event detector was used) and individual signals were selected during playback at a later time. A direct computer interface to the Sony was not available at the time these tests were conducted and analyzed, so playback was into a manually triggered EG&G recording device at a sampling rate of 0.05 msec. These raw data sets were used for determination of first arrivals, but any amplitude processing was performed using data that were low-pass filtered at 2000 Hz. This filtering procedure eliminated the accelerometer resonances at 2200 Hz.

9.4 Number of Signals Observed

Figures 36-39 show the number of signals obtained during the four injections, with each bar interval being 30 seconds. Only signals greater than 40 μg 's are included in these histograms. For reference, the background noise levels are a few μg 's, so these signals are at least ten times the noise level. After breakdown, as shown in Figure 36, there are approximately 20 microseisms per 30 second interval during the pumping, with the number of signals tapering off quickly after shut-in. Several hundred large signals were recorded during this short injection.

As seen in Figure 37, fewer signals were recorded during the step-rate test, with most of the signals observed during the high flow-rate periods. Approximately 300 signals were observed during this injection. The KCl injection, shown in Figure 38, also had fewer signals than the previous pump, with about 300 signals observed over a considerably longer time period. The gel minifrac, a slightly larger volume than the KCl minifrac, resulted in nearly double the number of microseisms as can be seen in Figure 39. The most important point is that conditions at this site are such that large numbers of

microseisms are generated by hydraulic fractures of even modest size (e.g., the breakdown or the step-rate test).

9.5 Maps of Microseisms

As mentioned previously, separate signals were chosen for analysis by playing back the Sony and manually triggering to an EG&G model 2401 recorder. A total of 67 different events were sampled in this manner, including events from all of the injections and the perforation of the treatment well. In general, the larger events were chosen because of their clear p-wave arrivals, but some smaller and some unusual signals were also selected. Initial analysis of Part B consists of determination of p-wave and s-wave arrivals for each signal and the polarization of the first one-two cycles of the p-wave.

Figure 40 shows a plan view of the locations of the subset of analyzable microseisms taken from the 67 events extracted from the continuous recording. This map shows the approximate locations of signals from all four injections; it should be stressed that these locations are approximate because of the orientation errors associated with using perforations as well as the uncertainty in locating the microseism. The apparent azimuth of the hydraulic fractures is about N65°E, about the same orientation as was determined in previous hydraulic-fracture experiments at this site. The half length of the east wing appears to be at least 200-300 ft, with a possibility of being over 400 ft (since there is only one data point at 400 ft, there is not good confidence in this data point). The east wing of the fracture is relatively well described, but the west wing has few points, possibly because of the distance but also possibly due to some attenuating effects of the formation (such as orientation of natural fractures). It is believed that the hydraulic fracture could be more completely described if additional microseisms are analyzed, but such an additional effort is outside of the scope of this suitability experiment.

A side view of the microseism locations is shown in Figure 41. Signals are observed within a 350 ft high band, but most of the signals are within a 200 ft high region. Because the velocity structure of the different layers within this region is not known, it is difficult to assess the uncertainty associated with this height map. Nevertheless, the ability to define a rough outline of one wing of the fracture (east wing) with such a limited data set (and all the uncertainties associated with using a single receiver and perforations for orientation) shows that hydraulic fractures can be mapped at this site.

9.6 Description of Microseisms

Examples of some of the observed microseisms and their notable features are given in this section. These results are useful for planning the type of instrumentation that will be required for full-scale microseismic monitoring at this site.

Figure 42 shows the three traces taken from event number 33 using the raw, or unfiltered data. In this example the signal clearly rises from the background at about 6.5 msec. Figure 43 shows an overlay of the three unfiltered traces and the polarization plot for the initial cycle and a half of the p-wave. The azimuth is 68° counterclockwise from the x axis (which is aligned with the east-west direction), with a standard deviation of 9° based on circular statistics. The vertical is down 9° with a standard deviation of 6°. The plot of the unfiltered data is best used for determining first arrivals.

Figure 44 shows the filtered data (low-pass filtered to 2000 Hz, as discussed previously) for this same event. The orientation from the hodogram is essentially the same orientation, with a slightly greater uncertainty. The s-wave, arriving at about 15 msec, was determined using three techniques. First, hodograms of the traces were searched for sections where the polarization shifted by approximately 90°; second, traces were searched for locations where amplitudes increased significantly; third traces were searched for locations where the frequency of the signal decreased significantly. Using some combination of the three techniques, it was generally possible to choose a well-defined s-wave arrival. In this example, there is a polarization shift, a frequency decrease, and an amplitude increase. Other events were not always so clear.

Given a difference in the p- and s-wave arrivals ($t_p - t_s$), the distance to the event can be calculated from the two equations,

$$d = V_p(t_p - t_o) \quad \text{and} \quad d = V_s(t_s - t_o),$$

where V_p and V_s are the p-wave and s-wave velocities. Eliminating t_o , the time of origination of the microseism, the distance can be found as

$$d = \frac{V_p V_s}{V_p - V_s} (t_p - t_s),$$

where the factor multiplying ($t_p - t_s$) is about 25 ft/msec for the sandstone and siltstone rocks. This factor is called the velocity factor in this report and in the figures. In Figure 44, the p-s separation is about 8.8 msec, yielding a distance of 221 ft from MWX-2. Thus, using the polarization and the p-s separation, the location of the microseism can be approximately determined.

Figure 45 shows event number 34 using the raw data. The unfiltered polarization plots are shown in Figure 46 and the filtered data in Figure 47. This event is an example of a microseism with greater uncertainty in the orientation (standard deviations of 16° and 18° in the horizontal and vertical planes, respectively), but a very clear s-wave arrival. In this microseism it can be seen that the unfiltered data provide a much clearer first arrival of the p-wave than the filtered data set. The orientation of this signal is 37° north of the x axis (east-west), with a p-s separation of 9.5 msec for a distance of 238 ft.

Figure 48 shows the three unfiltered traces from event number 4, a small signal that was detected during pumping when the background noise level was at its highest. The overlay of the unfiltered data is shown in Figure 49, where the first arrival of the signal is not as clear as in previous examples, nor are the hodograms as well polarized. The filtered results are shown in Figures 50 and 51, where it can be seen that the signals are much more difficult to process when noise levels are high or signal strength is low, or both. First arrivals of both the p and s waves are difficult to determine and polarizations have large uncertainties, in this case yielding standard deviations of 24° and 30° for the horizontal and vertical planes, respectively.

The plots in Figures 42-51 are examples of results taken from the 67 processed events. Table 9 gives the usable information from every event in which both p and s wave arrivals could be determined. Figures 40 and 41 were derived from the data in this table.

Table 9 Microseismic distance and orientation results

EVENT #	AZIMUTH (deg)	AZIMUTH STANDARD DEVIATION (deg)	INCLINATION (deg)	INCLINATION STANDARD DEVIATION (deg)	t_p-t_s (msec)	DISTANCE (ft)
1	-78	16	27	24	9.7	244
2	67	11	-12	18	7.2	181
4	54	24	-4	30	7.6	191
6	74	18	3	20	8.0	201
9	61	41	-30	34	6.7	169
11	41	38	8	19	7.5	188
12	-27	21	16	18	13.2	331
14	88	15	-14	26	7.5	188
15	65	22	-1	16	7.7	193
16	61	16	-12	21	8.7	218
17	55	27	-16	37	9.6	240
19	48	39	-21	32	7.4	186
20	75	22	-4	14	7.7	194
21	63	13	-7	24	7.5	188
22	68	34	-15	32	10.5	263
24	66	37	1	49	8.1	203
25	80	20	-15	14	9.5	238
28	67	38	9	22	7.1	178
29	-88	31	17	21	7.0	175
30	-83	14	16	31	11.5	288
32	58	29	1	14	7.9	198
33	66	14	-8	8	8.8	221
34	37	16	16	18	9.5	238
36	43	6	-80	59	10.2	256
38	80	7	-9	7	10.5	263
40	20	16	11	24	10.4	260
41	75	40	-15	28	9.2	231
42	76	28	-10	42	10.9	275
43	77	16	-12	8	7.6	190
44	77	37	-50	27	7.4	186
45	21	27	-10	23	11.6	290
46	51	35	-10	21	6.7	169
47	64	21	-11	17	9.0	225
48	4	14	16	14	16.8	421
49	-30	14	16	18	10.2	256
50	83	17	-1	17	12.5	313
51	77	20	-17	19	6.5	163
52	-88	18	41	21	11.4	285
53	57	11	-2	30	9.1	229
55	54	11	-3	9	7.7	194
56	46	29	-4	20	7.4	185
57	89	5	-9	4	11.7	294
61	59	11	1	9	7.5	188
62	66	32	-2	35	8.2	206
63	-85	9	18	18	10.9	273
65	-89	25	27	31	7.5	188
67	70	9	3	18	10.0	250

9.7 Spectral Content of the Microseisms

Spectra of both the noise and the microseisms were obtained for various events to determine if there was any characteristic frequency of the microseisms or other factor that may be important for microseismic monitoring at this site. Figure 52 shows the spectral response from 0-2000 Hz for the filtered x channel (east-west) data for event number 34 (shown previously in Figures 44-46). The noise spectrum is taken from the ambient background just prior to the event. Noise levels during pumping are elevated, but the microseism signal level is still 20-40 db greater, and both the noise and the microseism exhibit broadband frequency response. The same is true of the y-channel response, shown in Figure 53, and the z-channel response, shown in Figure 54, although the energy content of the z channel appears to drop off above about 1500 Hz.

Figures 55-57 show the x, y and z channels for the filtered data of event number 25, where all three channels exhibit a flat, broadband response out to 2000 Hz. Again, the microseism signal is 20-30 db above the ambient noise level. These results show that microseismic monitoring at this site, and probably any other location, will require a seismic receiver that is capable of acquiring signal information over a broad frequency range.

9.8 Conclusions of Seismic Suitability Assessment

The primary conclusion of the seismic suitability assessment is that this is a favorable site for hydraulic fracture diagnostic experiments. Technical reasons for this assessment are:

1. Both of the current wellbores (MWX-2 and MWX-3) are acceptable for seismic monitoring experiments. Noise conditions were low and signals were clearly obtained in both wellbores.
2. Even with ongoing production activities in two nearby wellbores (MWX-1 and SHCT-1), the background noise level at the site was extremely low.
3. Over 1000 microseismic signals were generated during the hydraulic-fracture injections. Thus, large numbers of signals are available for mapping the hydraulic fracture.
4. Many microseisms have clear first arrivals with high signal-to-noise ratios. This is the most important characteristic for determining distance to an event since triangulation techniques will be used for distance estimates.
5. Many microseisms had highly polarized p-wave arrivals, indicating that the orientation of the events can be determined. Coupled with the distance estimate, this experiment demonstrates that seismic signals can be located.
6. Many microseisms had both p- and s-waves that were well defined, demonstrating that event distance can also be determined from p-s separations, assuming that the velocity structure is known.
7. A rough map of the fracture could be made with a limited number of signals, and the orientation of the fracture agrees with the orientation of the stress field at this site.

9.9 Recommendations for Future Monitoring

The results of this site suitability assessment have implications for any additional work done at this site or other sites. Recommendations for future monitoring are:

Record continuously on a wide-band-width, wide-dynamic-range audio-digital recorder such as the Sony that was used in these tests.

Develop a high-sample rate, real-time event detector.

Use a gyro or other means for an accurate, ground-truth orientation of the receiver(s).

Take special precautions to assure a good quality clamp of the receiver(s).

Consider multi-station receiver arrays for improved range and azimuth measurements.

Develop techniques to automate the processing as much as possible. With so many microseisms, only a small fraction of them can be processed individually by an analyst.

Select and characterize weak signals which may have come a long distance, and thus provide information on the extremities of the fracture (if not already observed by the stronger signals).

10.0 OTHER DIAGNOSTIC ACTIVITIES

10.1 Gyro Adapter

In preparation for using the advanced seismic receiver for general diagnostic applications, it will be necessary to have orientation capabilities. At the present time, the only suitable method for providing orientation at many stations at different times is to use the Gyrodata orienting tool. This requires the addition of some electronics for switching between the gyro and the receiver and some method of connection.

10.1.1 Electronics

An electronic switch has been installed in the receiver to allow power to be applied to the gyro tool only or the receiver only. This is necessary because of the different power requirements for each tool, since the output is modulated on top of the input signal.

10.1.2 Interconnect

A 7-conductor change-over has been designed to provide a "hard" interconnect between tools. This interconnect should provide accurate absolute orientation numbers between tools, but the frequency response of the receiver may change with the gyro attached. A "soft interconnect has also been considered, which may not have the frequency response problems, but may not be as accurate for providing absolute orientation of the tool. In addition to the interconnect, the method for aligning the 7-conductor GO head so that accurate alignment has been achieved and a method for measuring the alignment (whatever it may be) have both been considered.

11.0 REFERENCES

- 1 Teufel, L. W., Determination of the Principal Horizontal Stress Directions from Anelastic Strain Recovery Measurements of Oriented Core: Application to the Cotton Valley Formation, East Texas," Proc., ASME Symposium on Geomechanics, Houston, TX, June 20-22, 1983.
- 2 Blanton T.L, "The Relation Between Recovery Deformation and In Situ Stress Magnitudes," SPE Symposium on Low Permeability, Denver, CO, pp 213-218, March 13-16, 1983.
- 3 Warpinski, N.R. & L.W. Teufel, L.W, "A Viscoelastic Constitutive Model for Determining In Situ Stress Magnitudes from Anelastic Strain Recovery of Core," SPE Production Engineering, Vol. 4, pp. 272-280, August 1989.
- 4 Strickland, F.G. and N.K. Ren, "Predicting the In Situ Stress State for Deep Wells Using Differential Strain Curve Analysis," SPE 8954, SPE Unconventional Gas Recovery Symposium, Pittsburgh, PA, pp. 251-258, May 18-20, 1980.
- 5 Sayers, C. M., "Stress-Induced Ultrasonic S-wave Velocity Anisotropy in Fractured Rock," Ultrasonics, Vol. 26, pp. 311-317, Nov. 1988.
- 6 Lorenz, J.C., Teufel, L.W., and Warpinski, N.R., "Regional fractures II: A mechanism for the formation of regional fractures at depth in flat-lying reservoirs," AAPG Bulletin, Vol. 75, pp. 1714-1737, 1991.
- 7 Weimer, R.J., "Uppermost Cretaceous rocks in central and southern Wyoming and northwest Colorado," Wyo. Geol. Assoc. 16th Annual Field Conf., p. 17-28, 1961.
- 8 Monley, L.E., "Petroleum potential of Idaho-Wyoming overthrust belt," AAPG Memoir 15, pp. 509-537, 1971.
- 9 Hansen, W.R., "Geology of the Flaming Gorge area, Utah-Colorado-Wyoming," U.S. Geological Survey Professional Paper 490, 196 p., 1965.
- 10 Hansen, W.R., and Bonilla, M.G., "Laramide faulting on the north flank of the Uinta Mountains in eastern Daggett County, Utah," Proceedings of the Colorado Scientific Society, Vol. 17, 29 p., 1954.
- 11 Wiltschko, D.V., and Dorr, J.A., "Timing of deformation in overthrust belt and foreland of Idaho, Wyoming, and Utah," AAPG Bulletin, Vol. 67, pp. 1304-1322, 1983.
- 12 Laubach, S.E., and Lorenz, J.C., "Preliminary assessment of natural fracture patterns in Frontier Formation sandstones, southwestern Wyoming," Wyoming Geological Association Guidebook, 43rd Field Conference, pp. 87-96, 1992.
13. Gidley, S.A. Holditch, D.E. Nierode, & R.W. Veatch, Editors, "Recent Advances in Hydraulic Fracturing," SPE Monograph Volume 12, Richardson, TX, June 1989.
14. Geertsma, J. & R. Haafkens, "A Comparison of the Theories for Predicting Width and Extent of Vertical Hydraulically Induced Fractures," ASME J. Energy Res. Tech., Vol. 101, 8-19, March 1979.

12.0 MAJOR ACHIEVEMENTS

Major achievements include:

1. Successful completion of the M-Site suitability experiment. The results of these tests were all positive and the M-Site appears to be well suited for hydraulic-fracture experiment whose objectives are to validate and improve diagnostic techniques and design models
2. Excellent performance of a new, accelerometer-based receiver for passive seismic monitoring. Signal to noise ratios were usually better than 100:1 at distances from 200-400 ft, the observed frequency content of the microseisms was broadband out to 1.5-1.8 kHz, and the signals were highly polarized with clear p- and s-wave arrivals.
3. Completion of the SPE paper on the results of the Fracture Propagation Modeling Forum. This paper will be presented at the Low Permeability Symposium in Denver. In addition, all of the results have been tabulated and plotted for inclusion in a complete GRI final report.
4. Continued analysis of core-based stress-measurement techniques have shown the value of Circumferential Velocity Anisotropy for determining stress azimuth and self-diagnosing problems such as fabric. A report is being prepared detailing these results, as well as features of all other core-based techniques.
5. Natural fracture studies in the Moxa Arch area of the Green River basin have shown that the fracture orientations are definitely related to basinal events, but the primary events have been the Uinta thrust and subsidence of the basin, not the shallow overthrust on the west.

13.0 MAJOR PROBLEMS

The major problem during the current year was:

1. UPRC's difficulty in obtaining oriented core made it impossible to obtain any stress orientation results in the Fabian Ditch #4-34 well. Both ASR and CVA were attempted, but the damaged nature of the core and the lack of orientation made it impossible to extract any meaningful results.

14.0 CONCLUSIONS

Preliminary conclusions of this project to date are:

1. The M-Site location is a suitable location for hydraulic fracturing experiments. The site has a low background seismic noise level, many microseisms are generated during hydraulic fracturing, the microseisms are analyzable both for polarization and p-s separation, and microseisms can be observed at significant distances. In addition, the current wellbores are suitable as observation wells or treatment wells.
2. Results of the Fracture Propagation Modeling Forum have shown that there are large differences in design models. Fracture lengths and heights may differ by more than a factor of two, and net pressures by 50%.
3. Additional effort must be invested in stress measurement techniques if the industry is to ever be able to reliably obtain important stress data. Nevertheless, the primary difficulty in using core-based techniques lies in obtaining high quality orientation data.
4. Natural fractures are important to production from the Frontier formation in many areas of the Greater Green River basin. Natural fractures in the Moxa Arch area are primarily due to the Uinta thrust and the subsidence of the Cretaceous foredeep.

15.0 OBJECTIVES AND WORK PLANNED FOR NEXT YEAR

For the next year, work will continue on the five project tasks with specific objectives of:

1. Complete a catalog of stress measurement techniques with the advantages, disadvantages, problems, etc of each technique described. This catalog would essentially be a user's guide to stress measurement capabilities for the industry.
2. Continue analyses of the importance of natural fractures in the Frontier formation in both the Moxa Arch area and in the deep part of the Green River basin. This program includes significant interactions with Union Pacific Resources.
3. Complete the final report on the Fracture Propagation Modeling Forum results.
4. M-Site activities will be the focus of activities next year, with detailed planning of the experiment and further analysis of the suitability results.
5. Sandia will continue to participate in any warranted GRI experiments in capacities of stress analysis, natural fracture characterization, stimulation design and analysis, fracture diagnostics, and other areas.

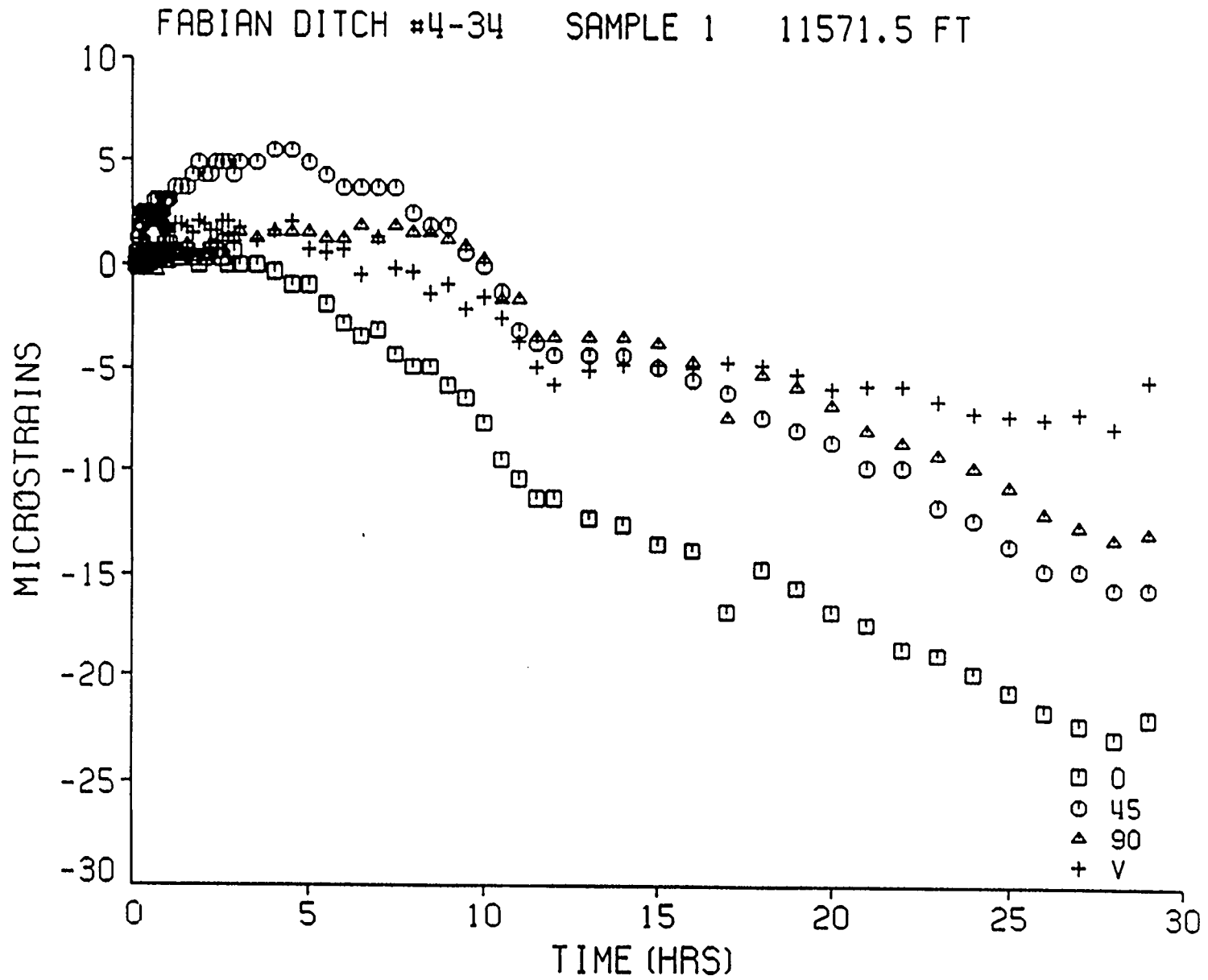


Figure 1. Fabian Ditch #4-34 ASR sample #1

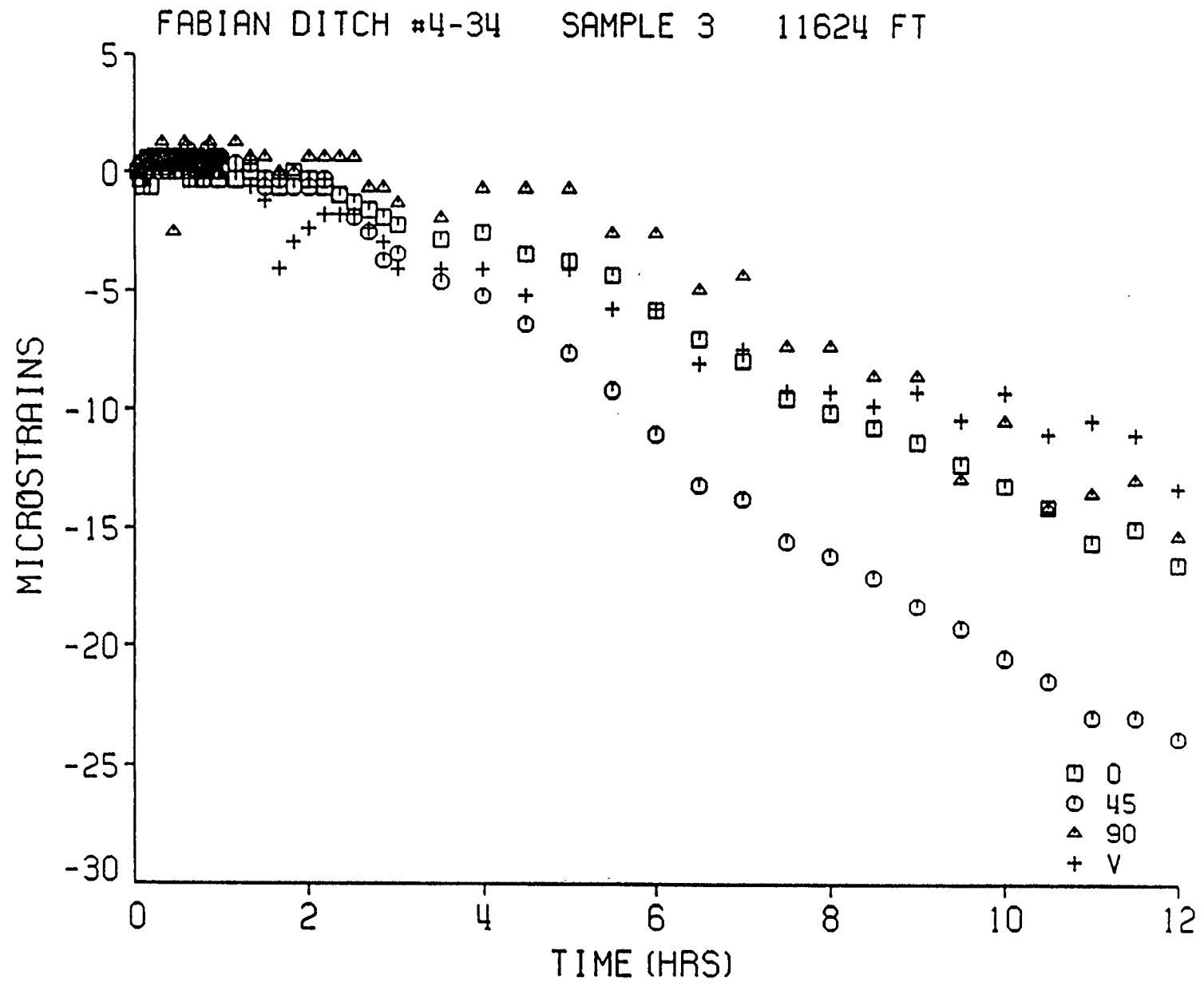
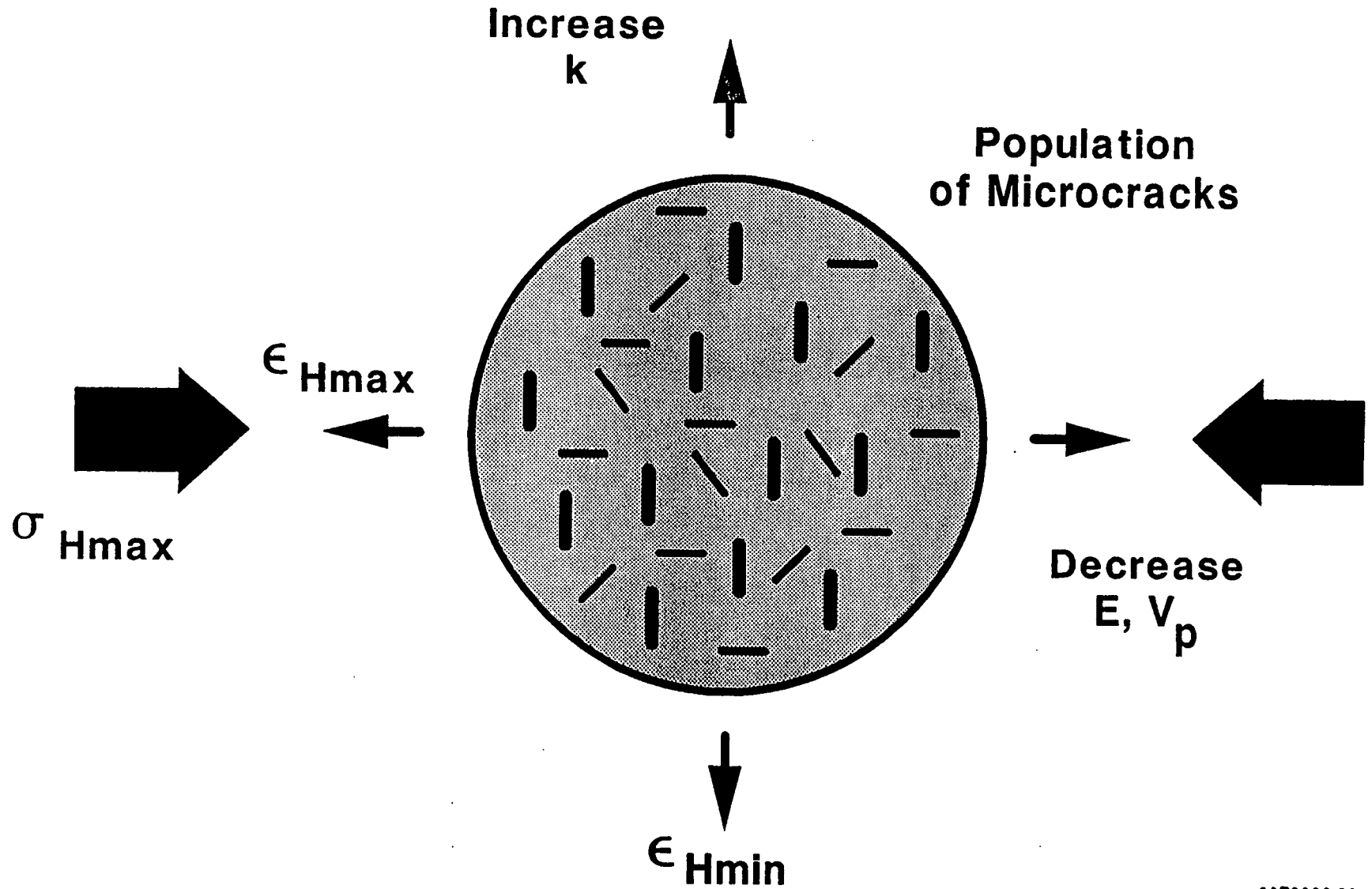


Figure 2. Fabian Ditch #4-34 ASR sample #3



90E6000.39

Figure 3. Schematic of microcracks in core

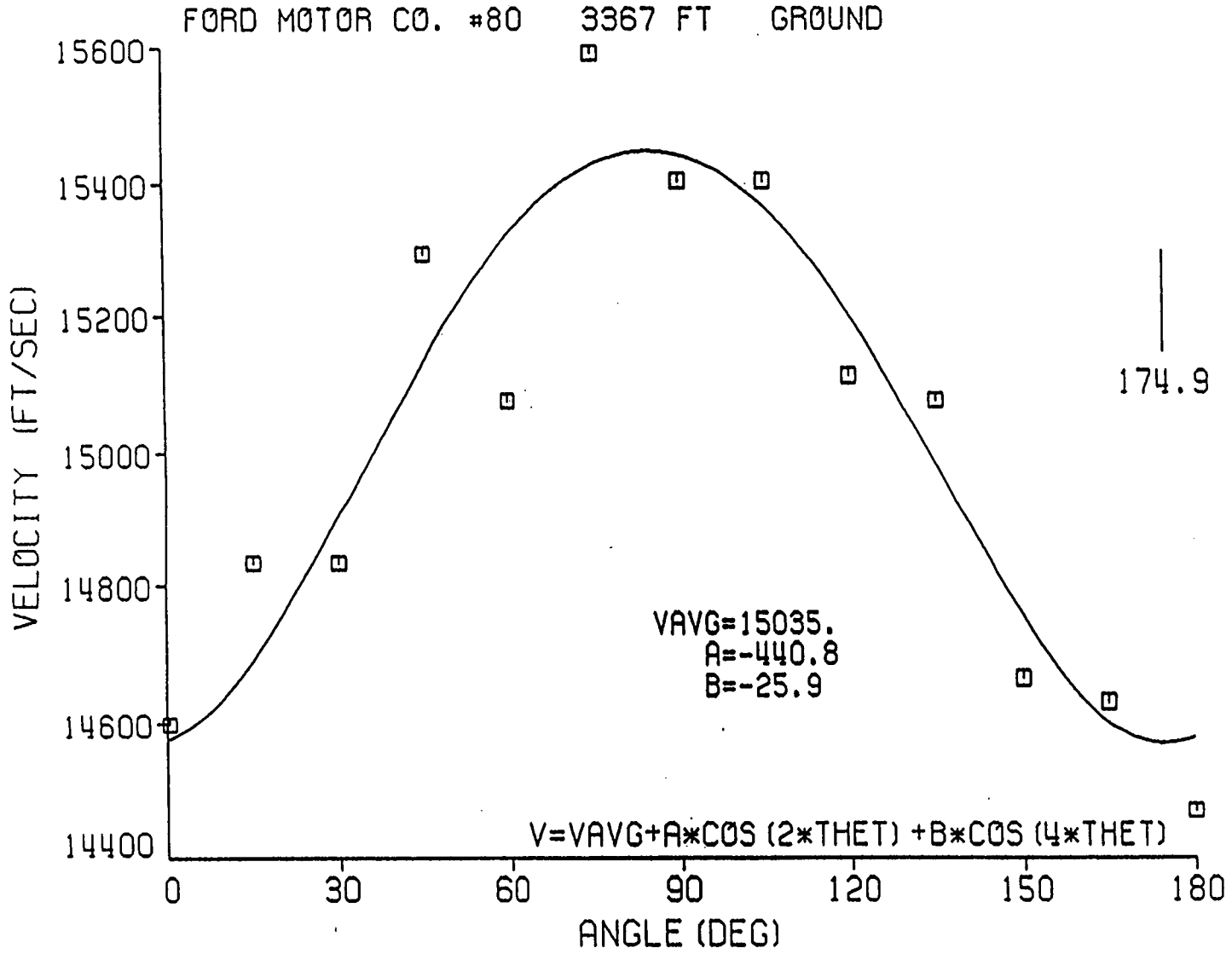


Figure 4. Ford Motor Co. #80 velocity results, 3367 ft

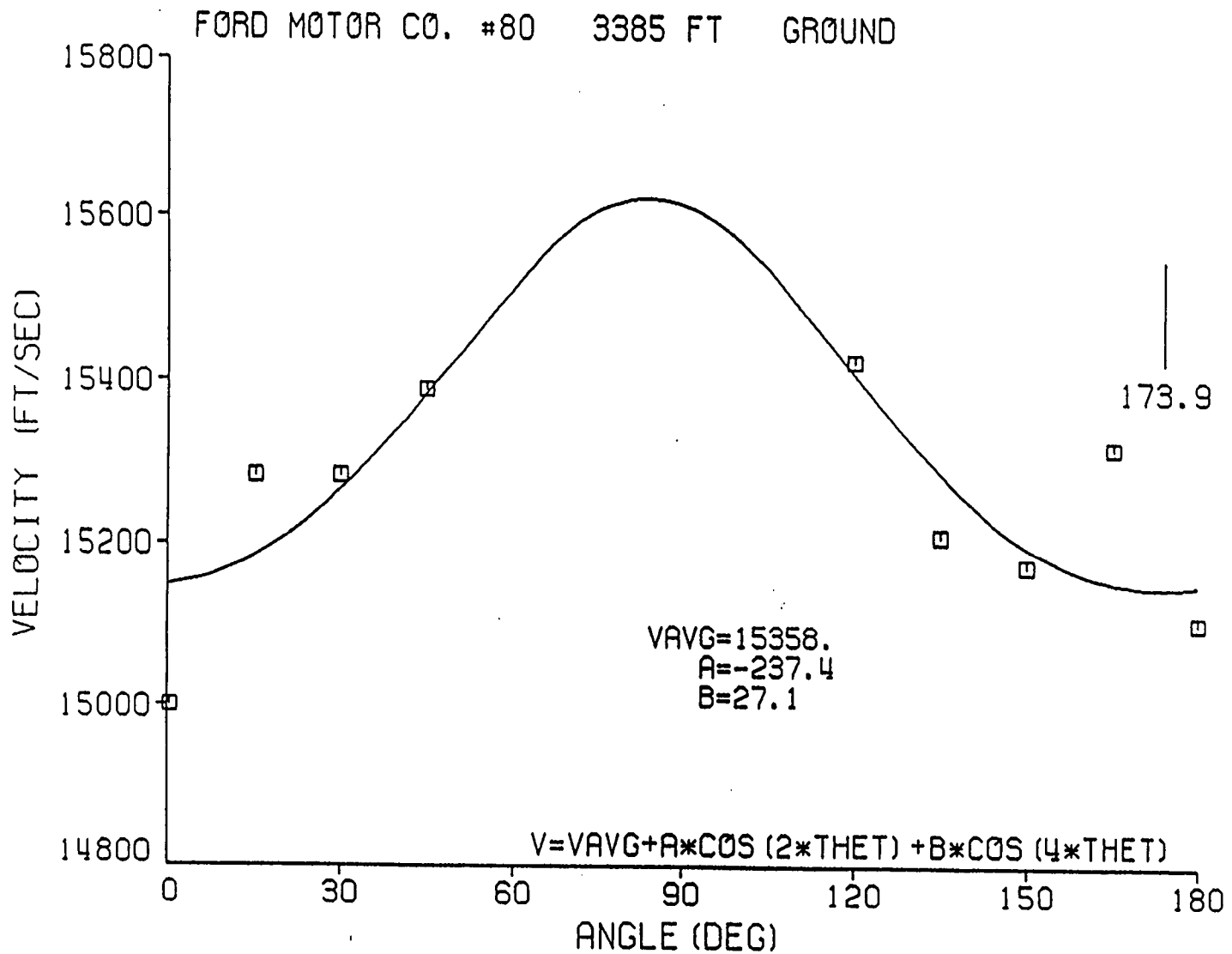


Figure 5. Ford Motor Co. #80 velocity results, 3385 ft

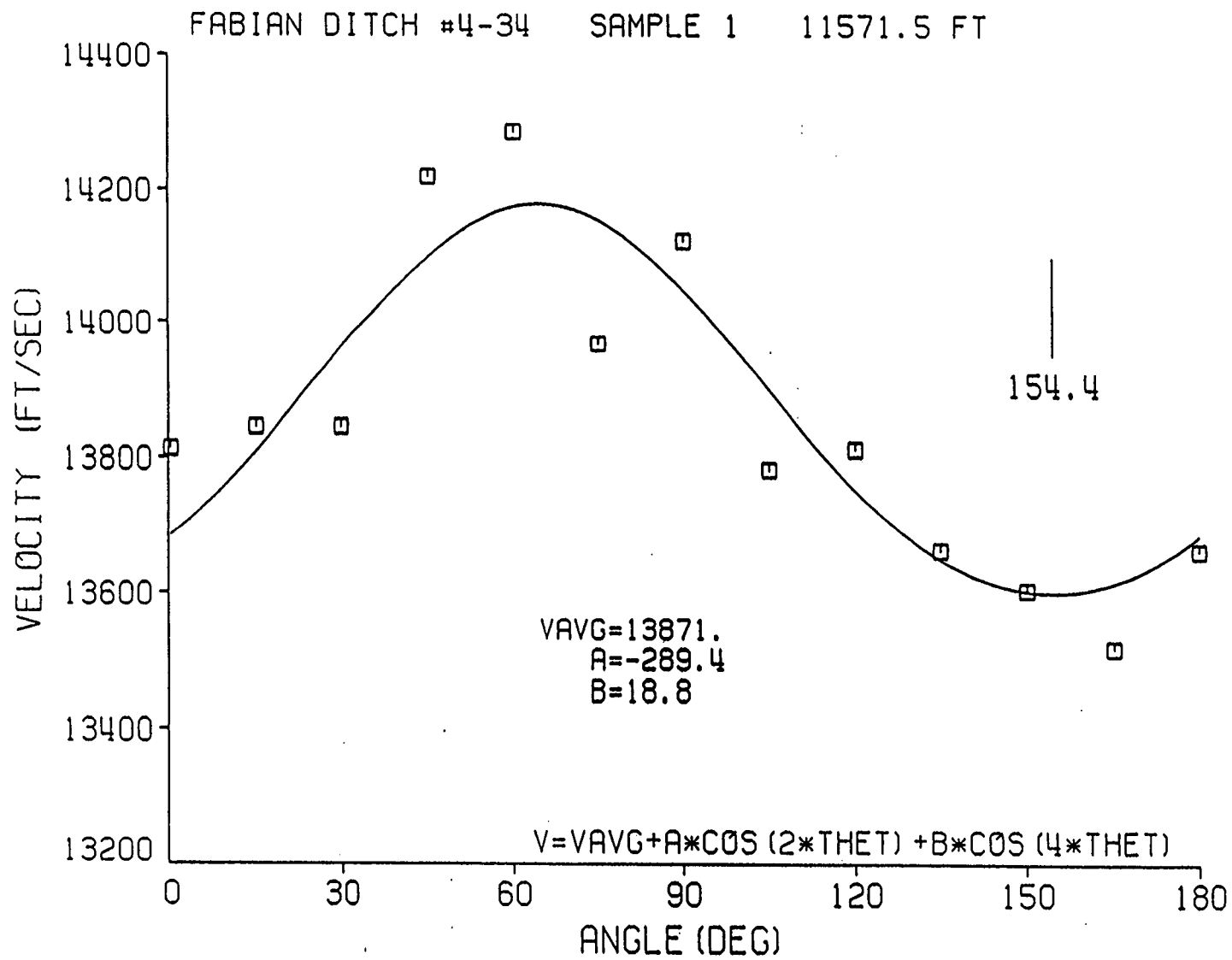


Figure 6. Fabian Ditch #4-34 CVA measurement for ASR sample 1

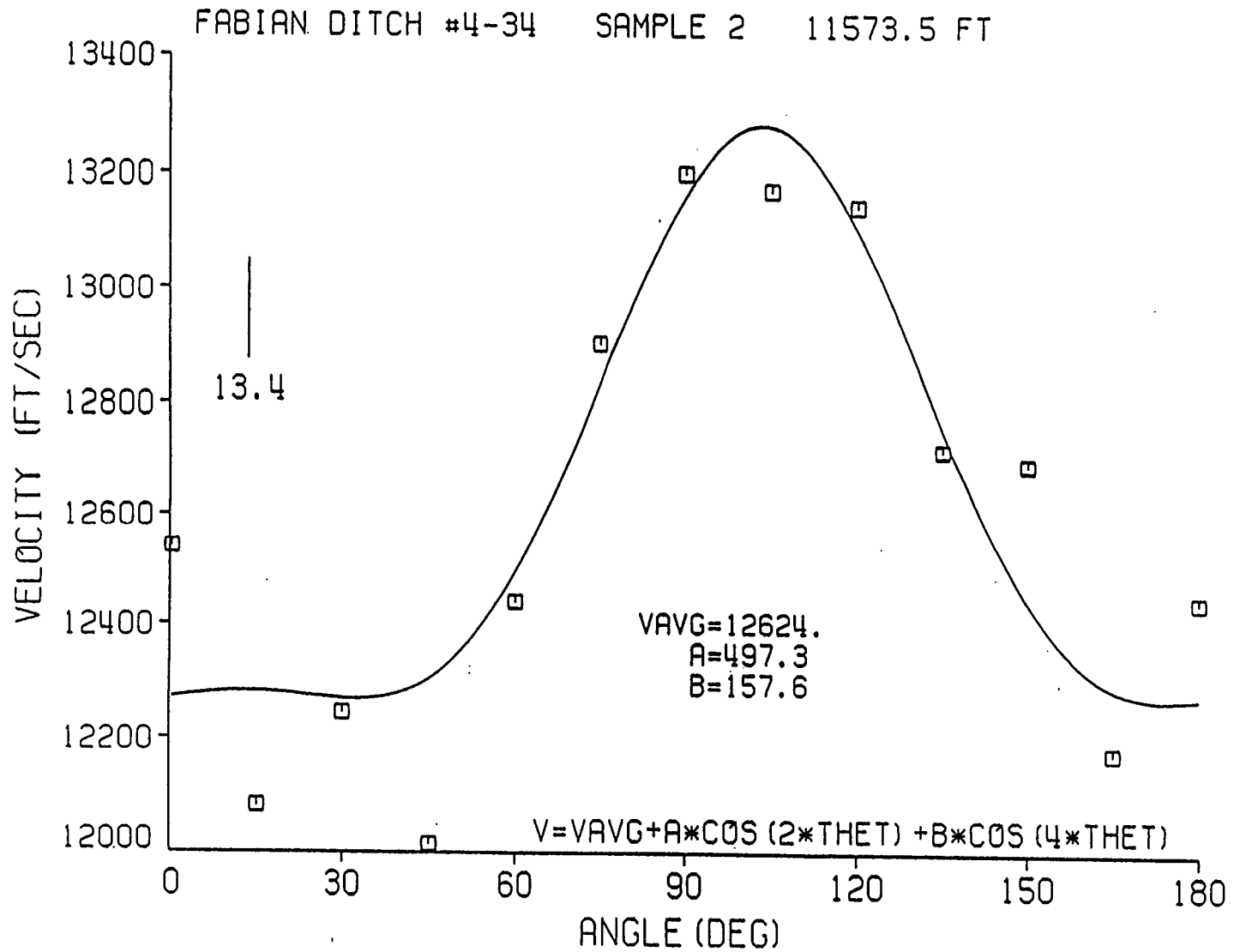


Figure 7. Fabian Ditch #4-34 CVA measurement for ASR sample 2

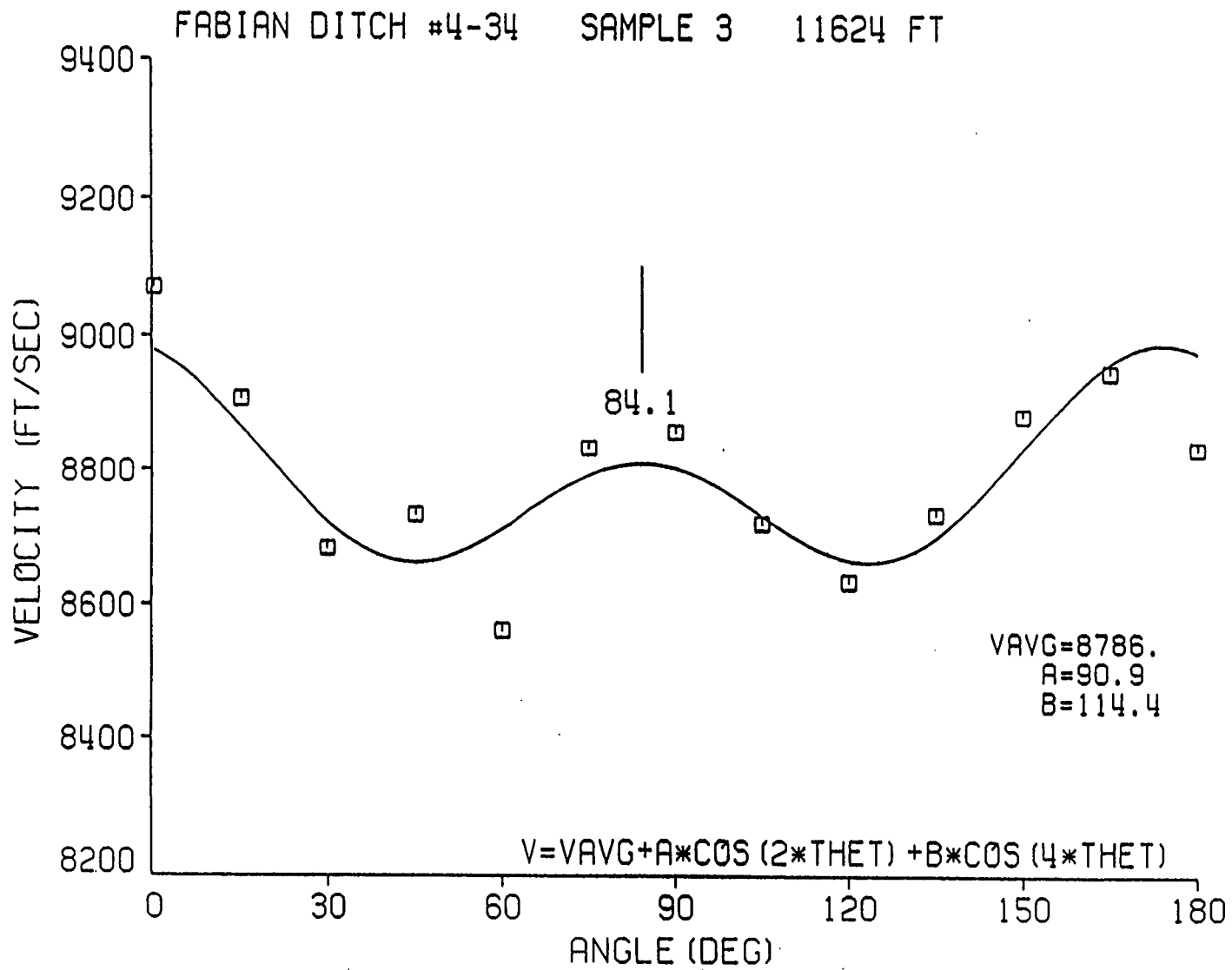


Figure 8. Fabian Ditch #4-34 CVA measurement for ASR sample 3

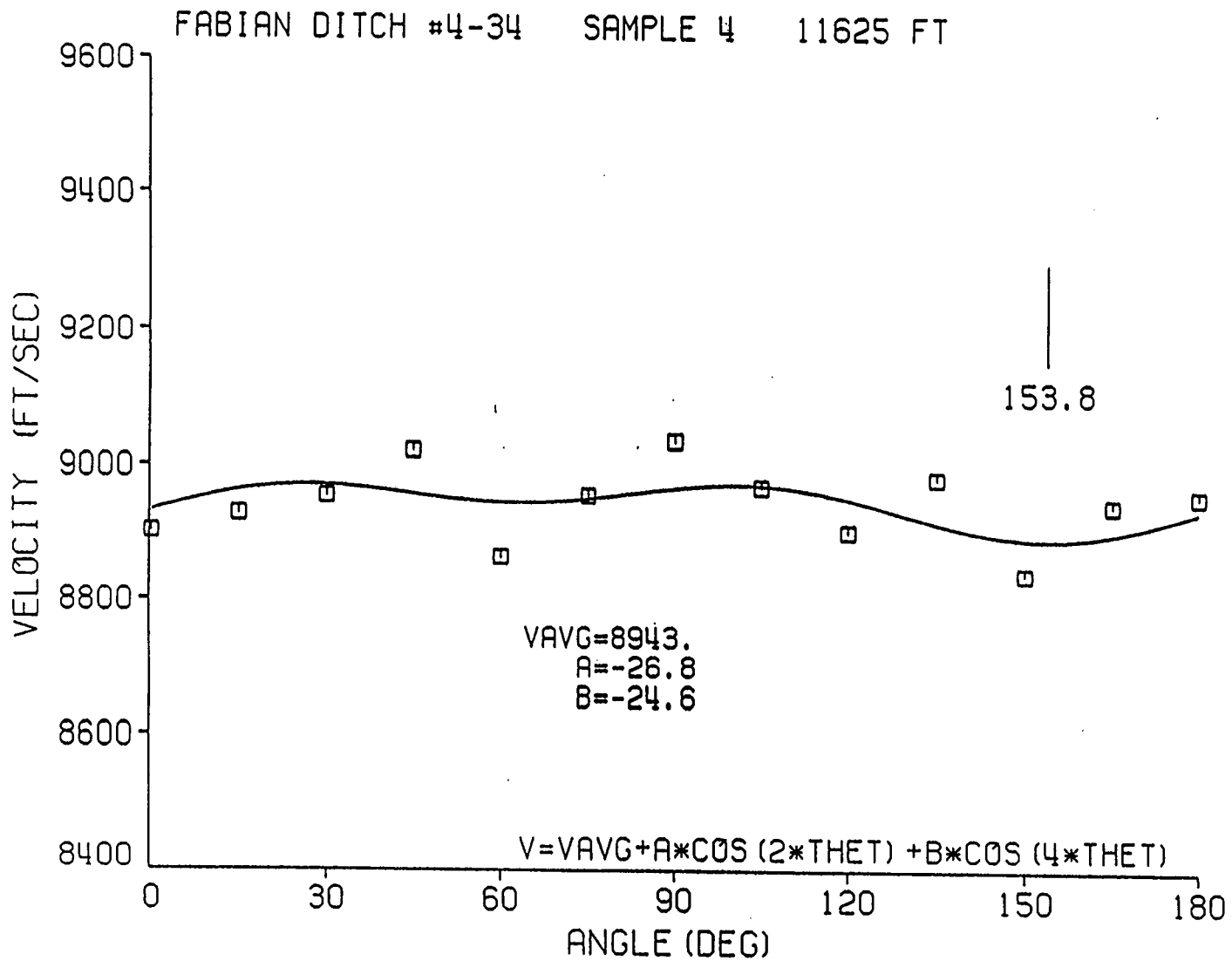


Figure 9. Fabian Ditch #4-34 CVA measurement for ASR sample 4

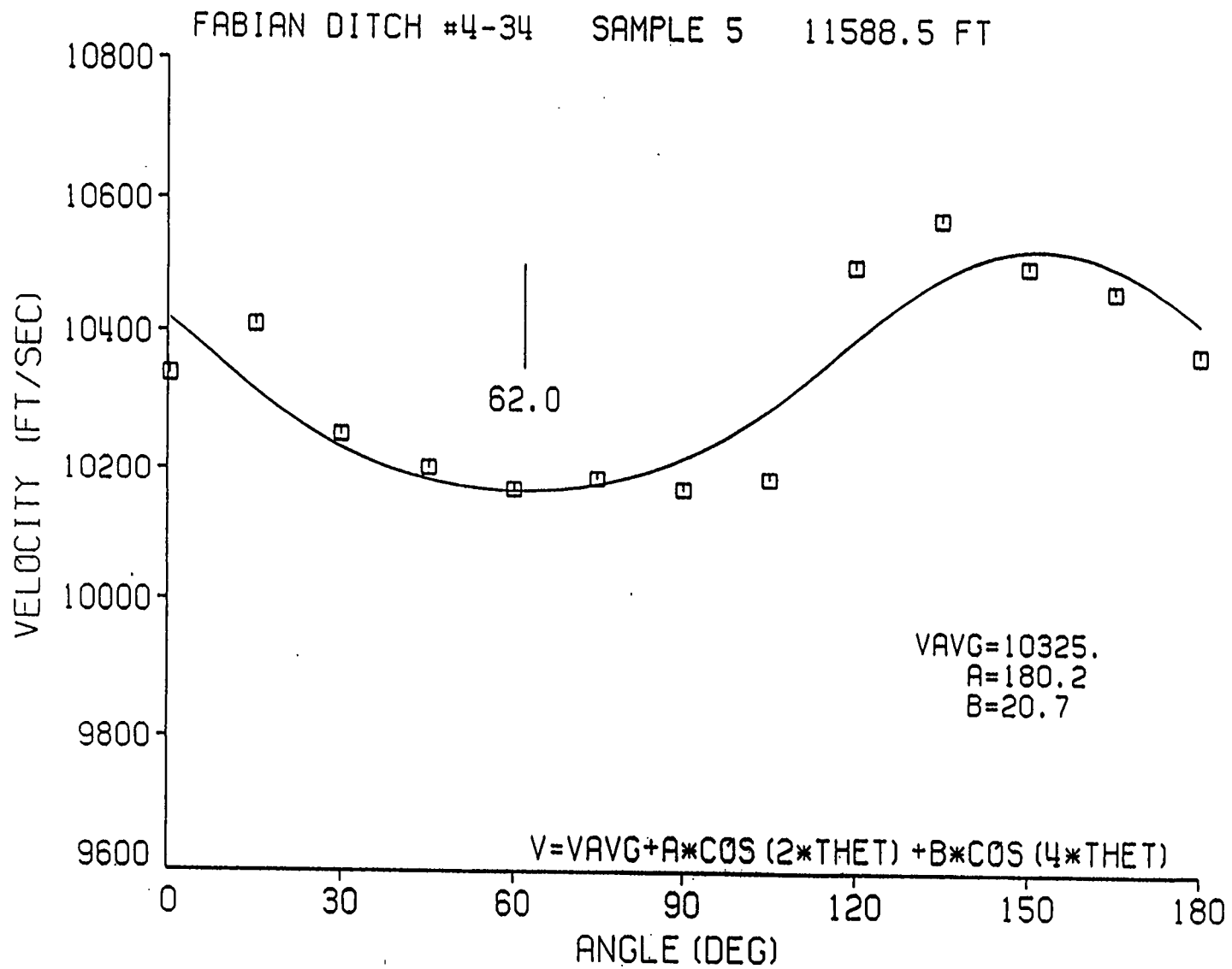


Figure 10. Fabian Ditch #4-34 CVA measurement for sample 5

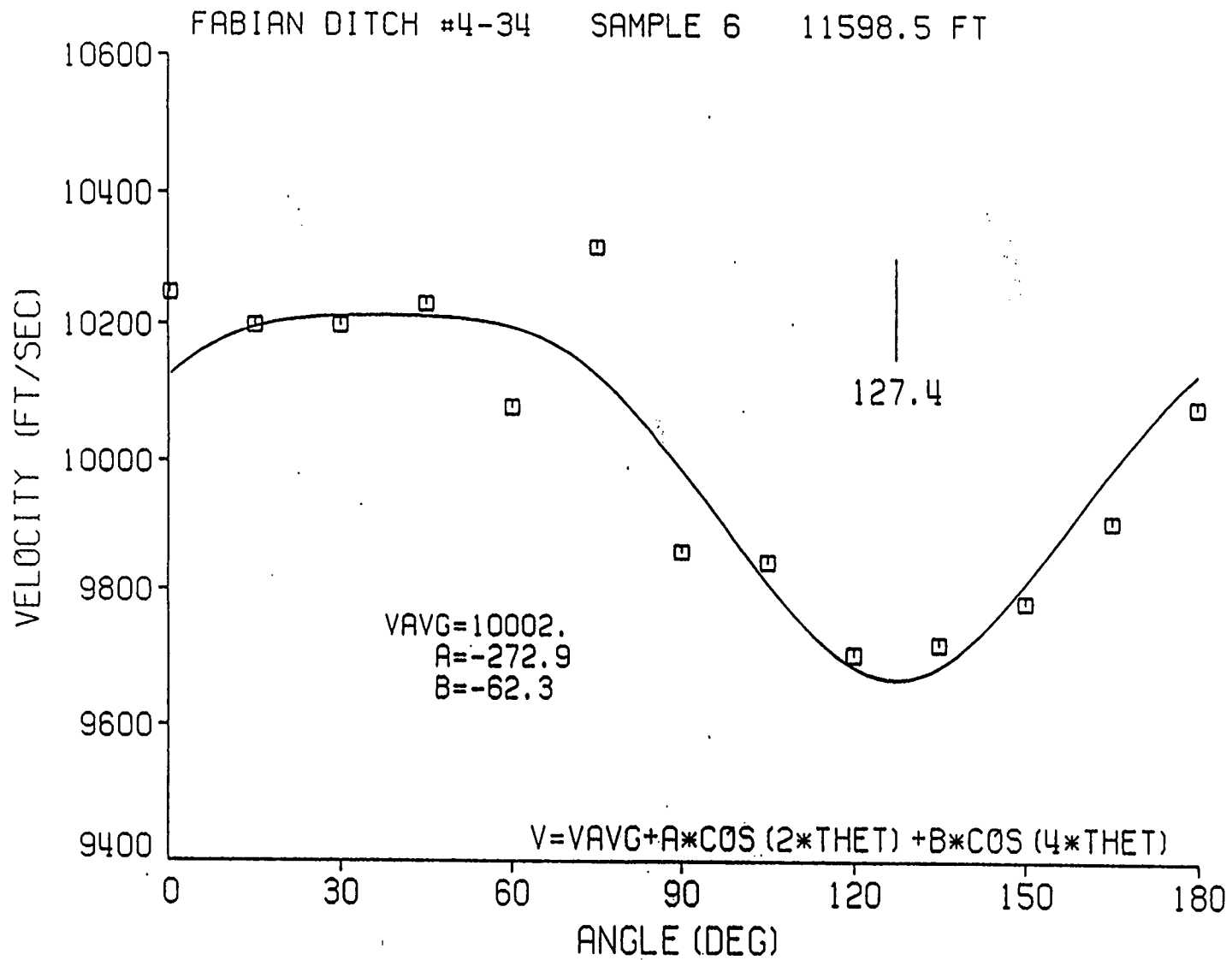


Figure 11. Fabian Ditch #4-34 CVA measurement for sample 6

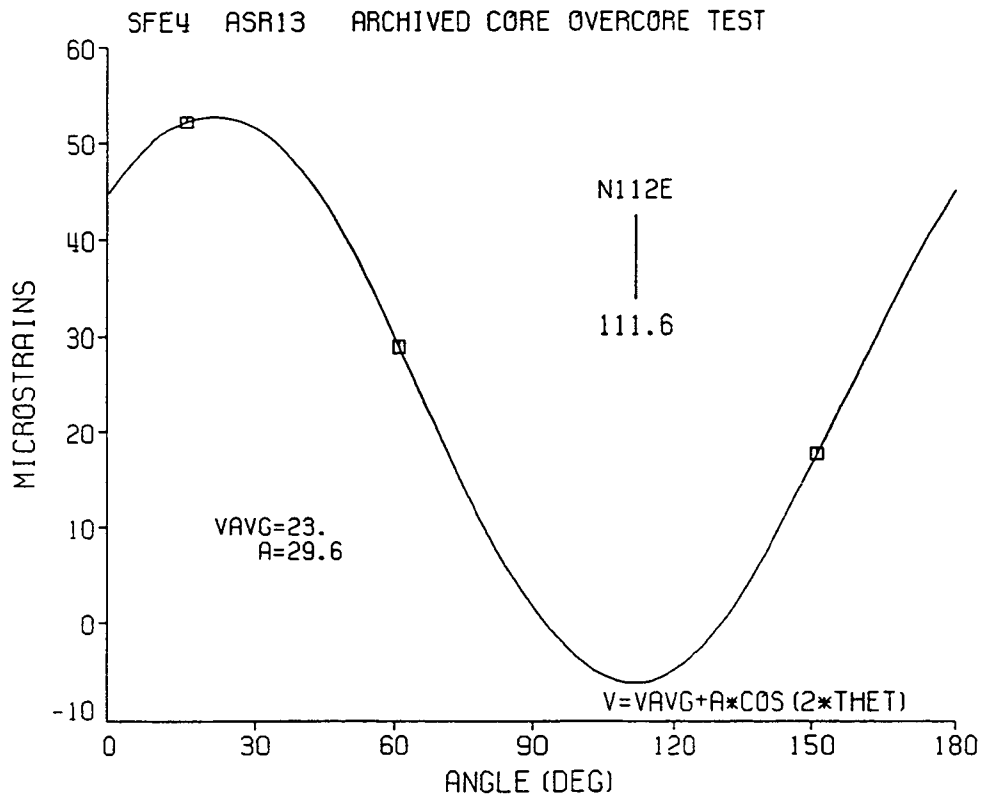
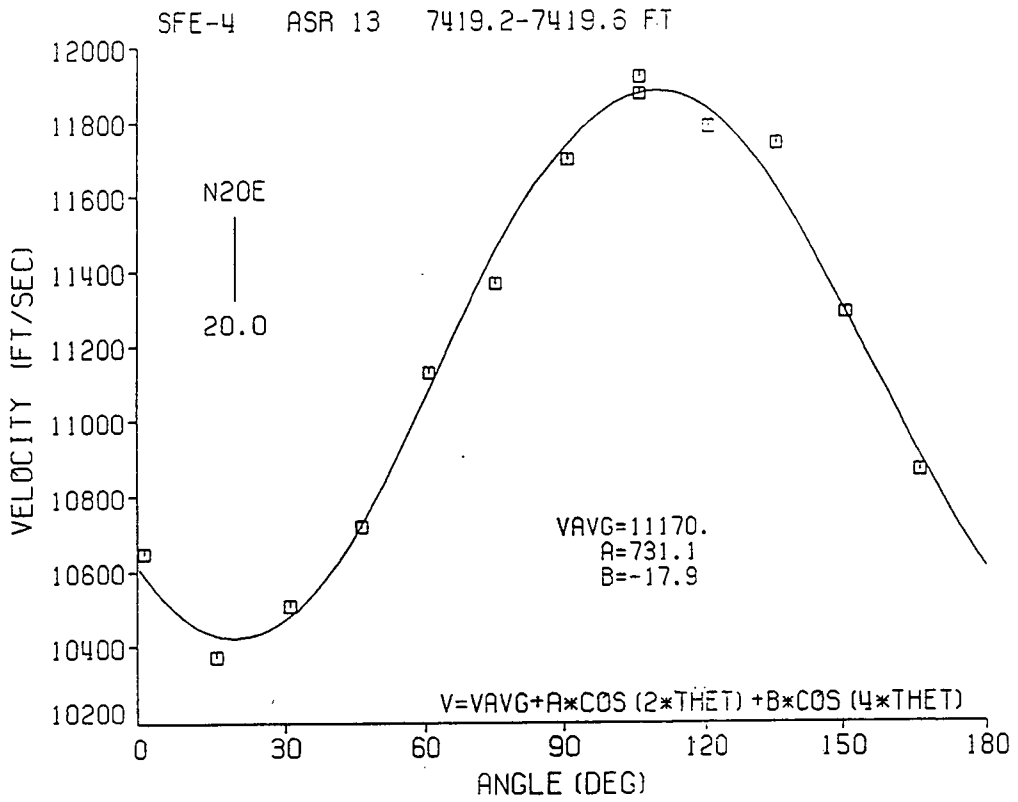
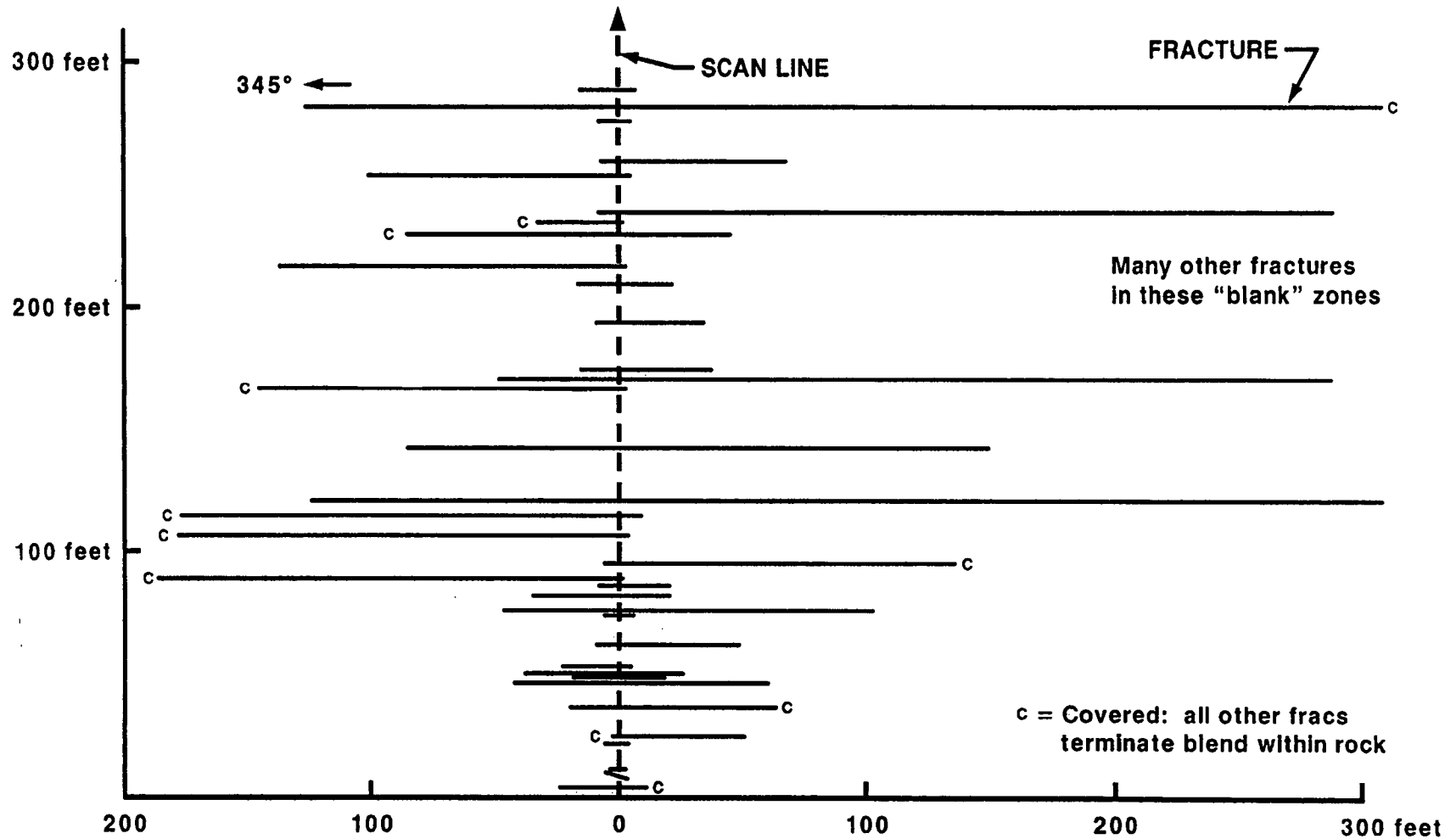


Figure 12. Results of overcoring of archived core

Extent of Fractures Intersecting Single Scan Line



92B6000.54

Figure 13. Map of north-south fractures that intersect a scan line on a bedding surface

Isopach of Upper Cretaceous Strata in the Foredeep East of the Thrust Belt

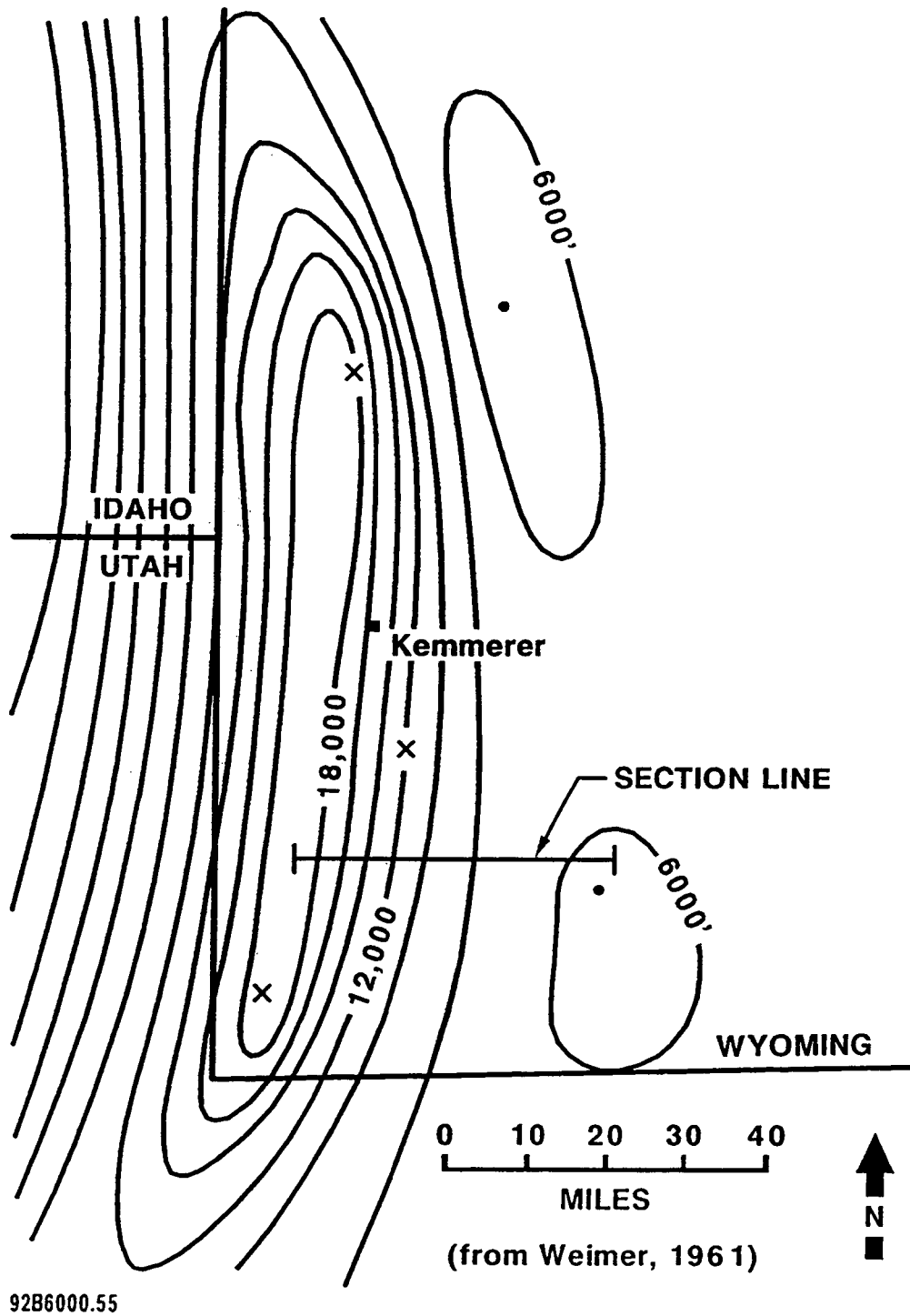
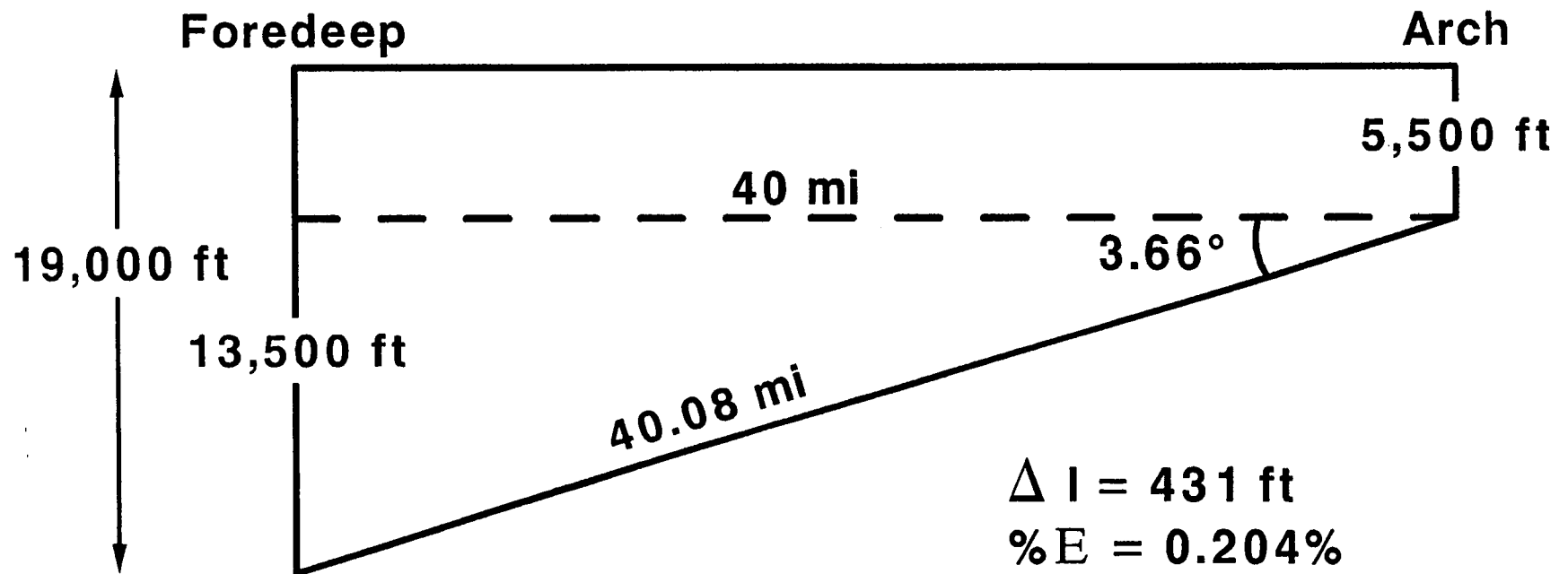


Figure 14. Isopach of Upper Cretaceous strata in, southwestern Wyoming (from Weimer, 1961)

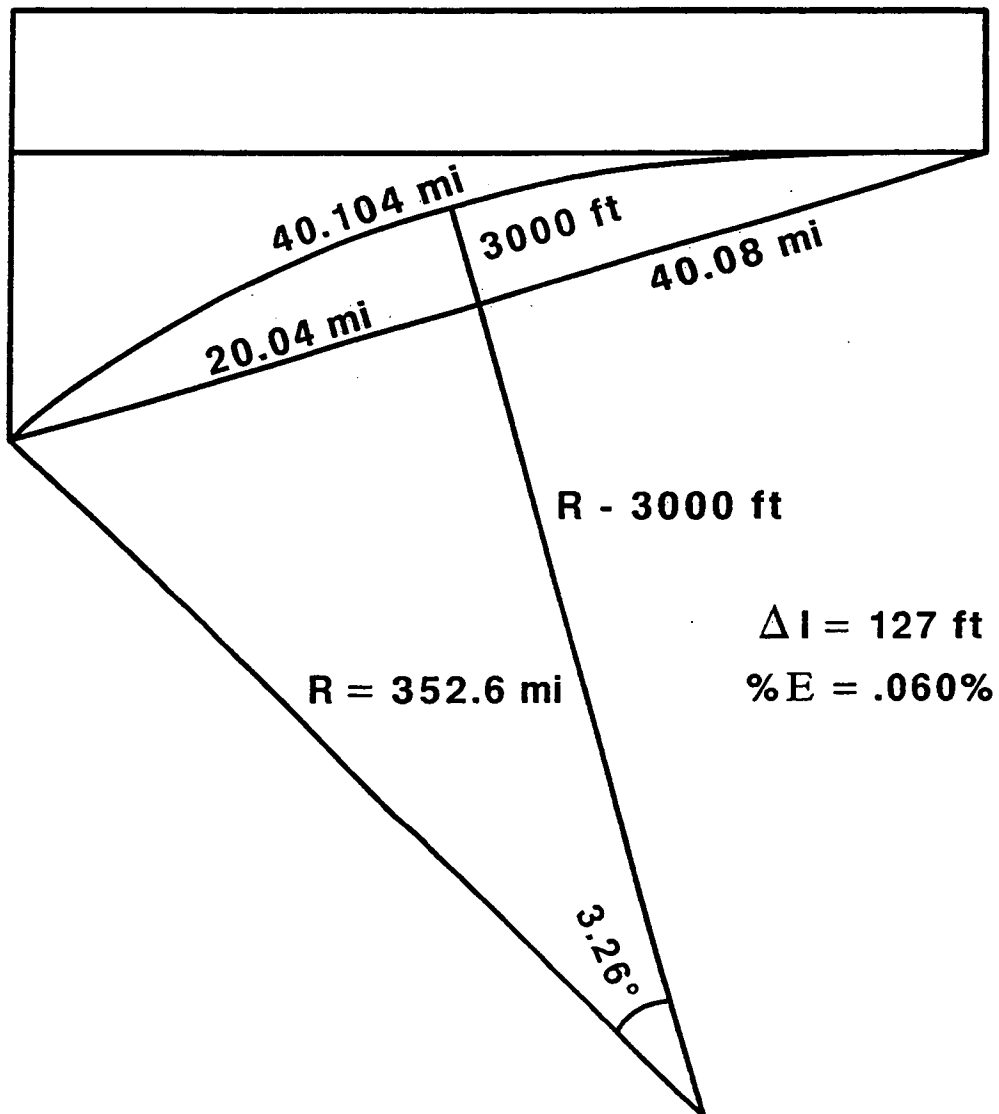
Strain from Lengthening Line to Hypotenuse



92B6000.57

Figure 15. Strain associated with asymmetric subsidence of Upper Cretaceous strata in southwestern Wyoming

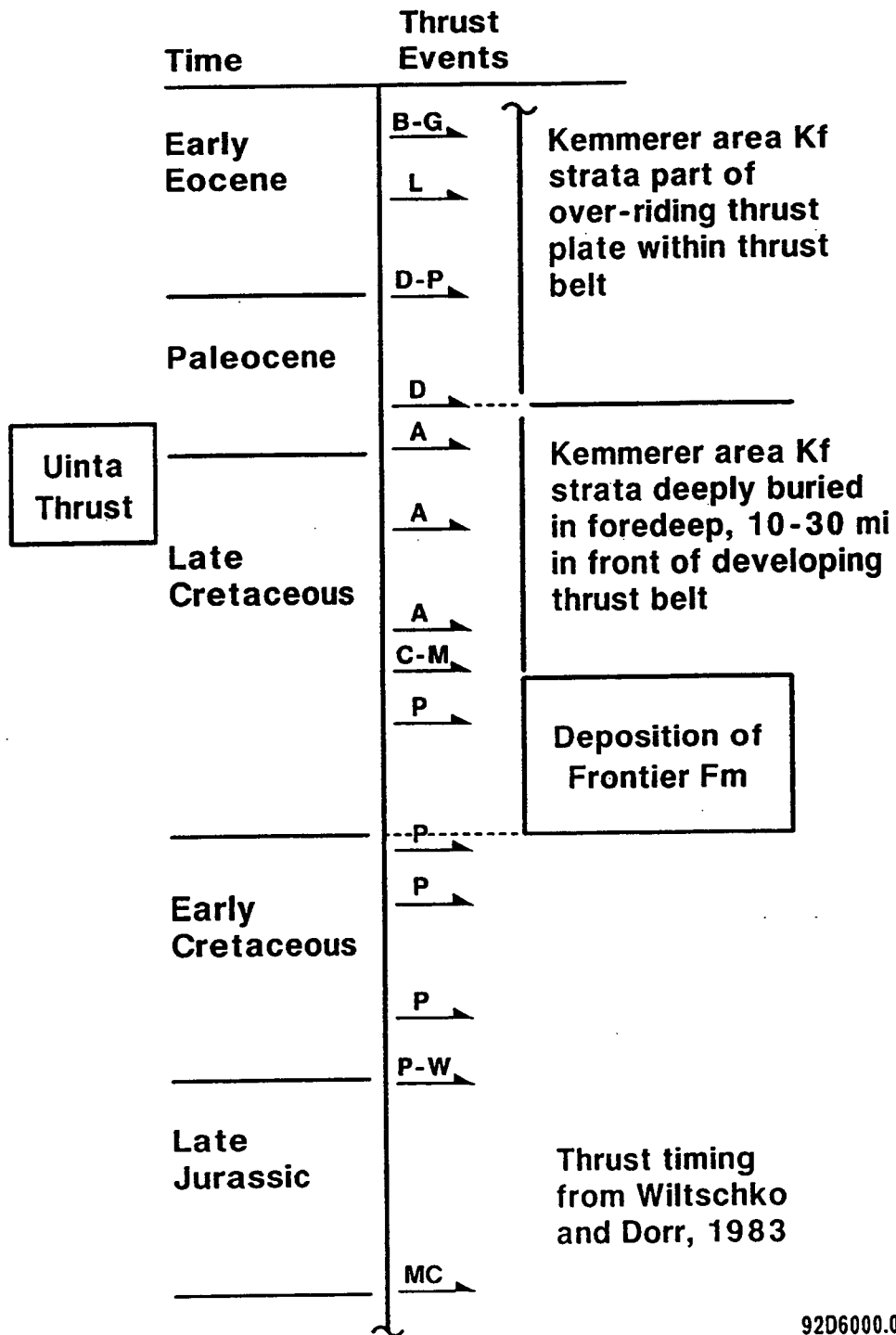
Strain from Lengthening Hypotenuse to Arc



92B6000.59

Figure 16. Strain associated with curvature of basin floor due to lithospheric flexure

Frontier Formation was Subjected to E-W Compression, Extension, and Flexure



92D6000.02

Figure 17. Deposition and burial of the Frontier Formation relative to episodes of thrusting. Thrust timing from Wiltschko and Dorr, 1983

FRACTURE HALF LENGTH CONSTANT HEIGHT MODELS

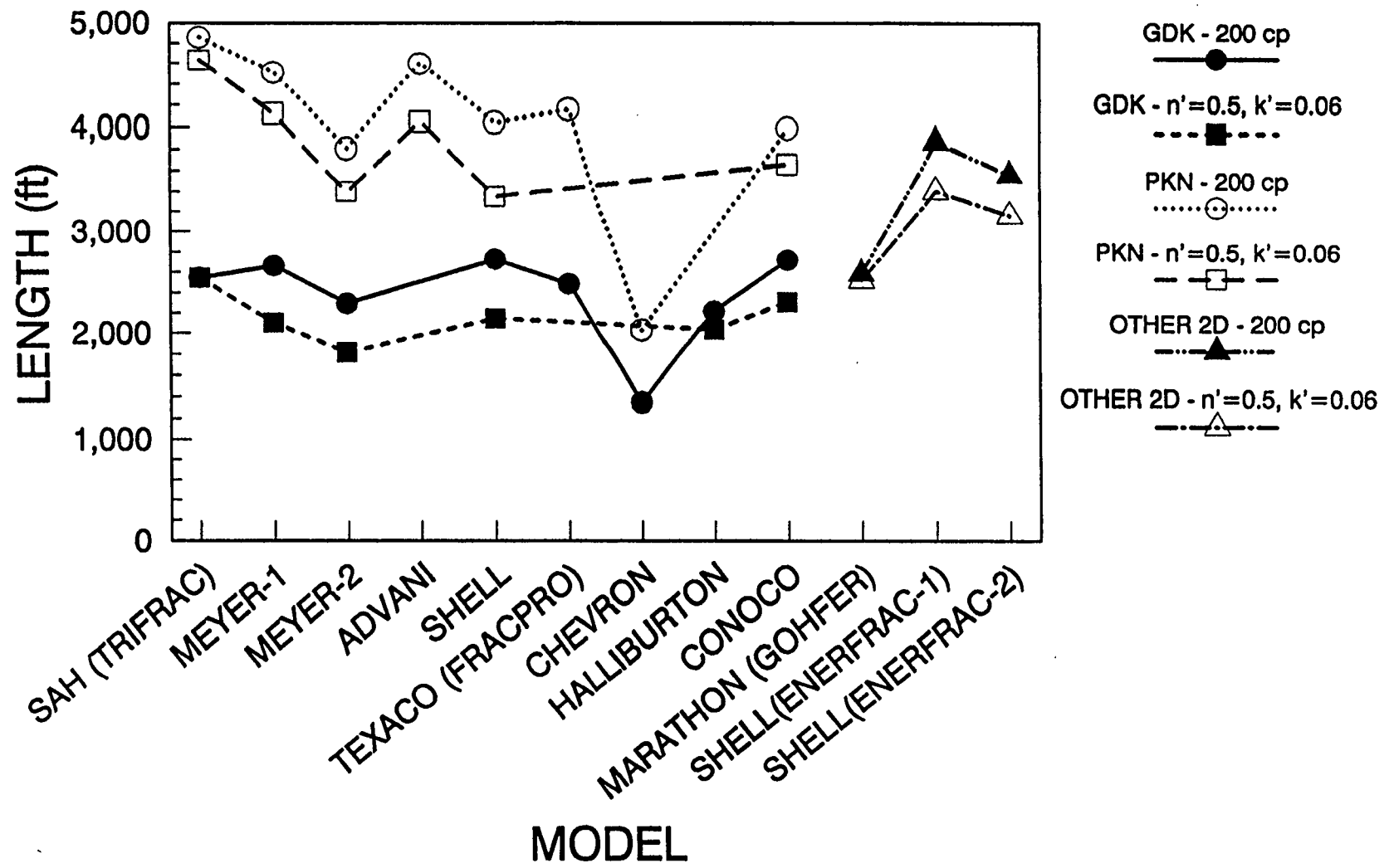


Figure 18. Length comparison for 2-D models

FRACTURE NET PRESSURE

CONSTANT HEIGHT MODELS

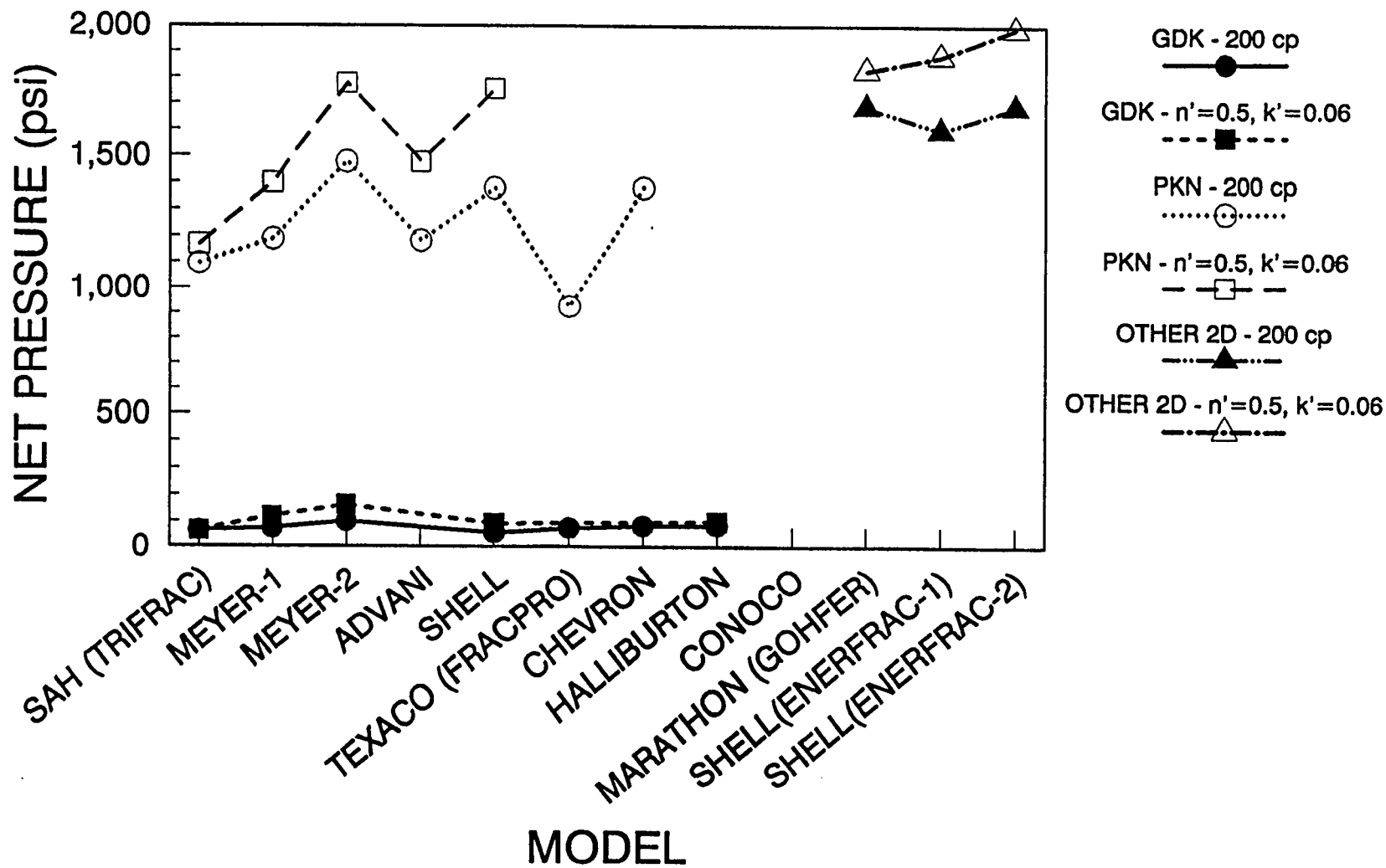


Figure 19. Pressure comparison for 2-D models

FRACTURE EFFICIENCY

CONSTANT HEIGHT MODELS

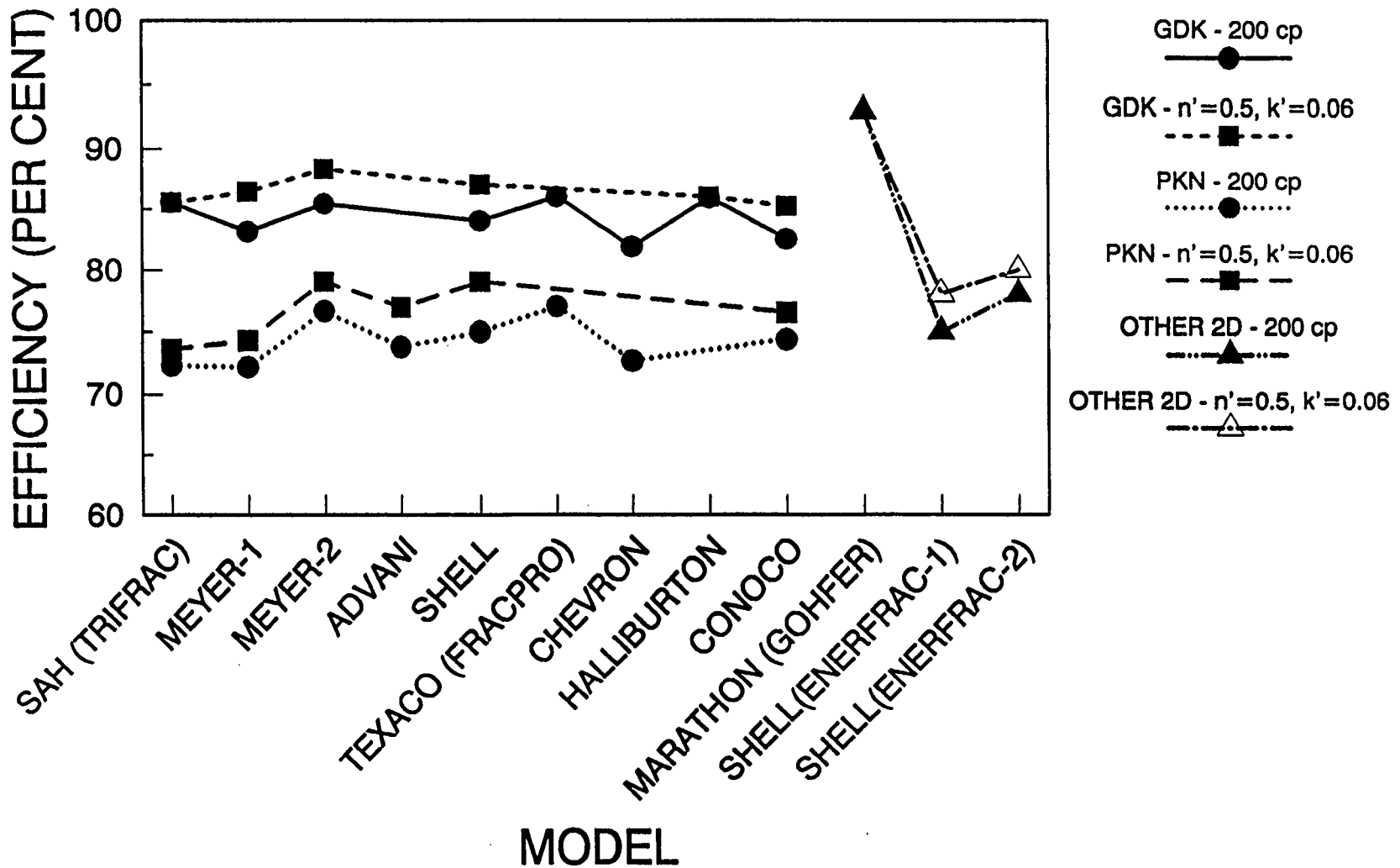


Figure 20. Efficiency comparison for 2-D models

FRACTURE HALF LENGTH

3-LAYER MODELS

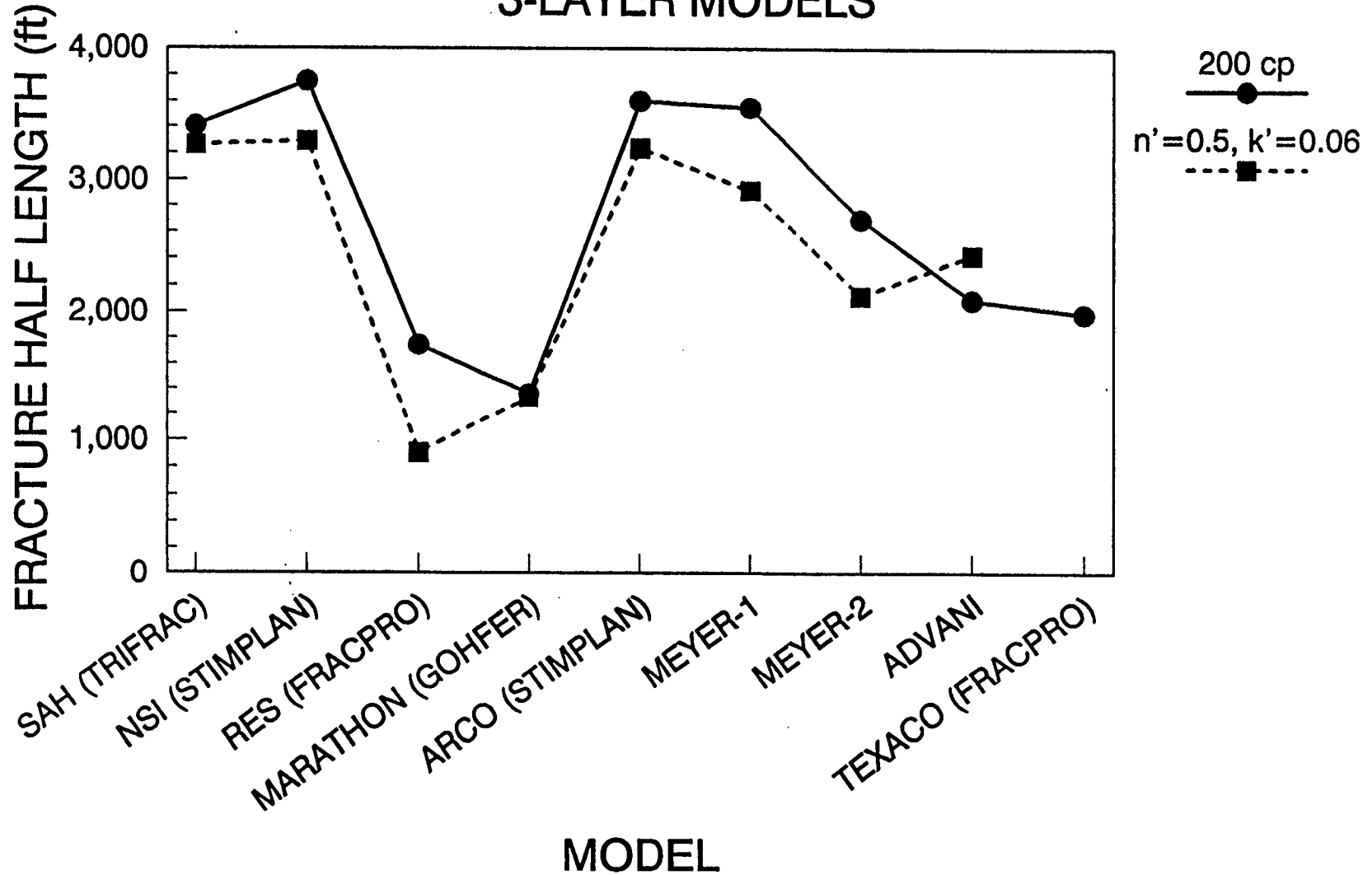


Figure 21. Length comparison for 3-layer cases

FRACTURE HEIGHT

3-LAYER MODELS

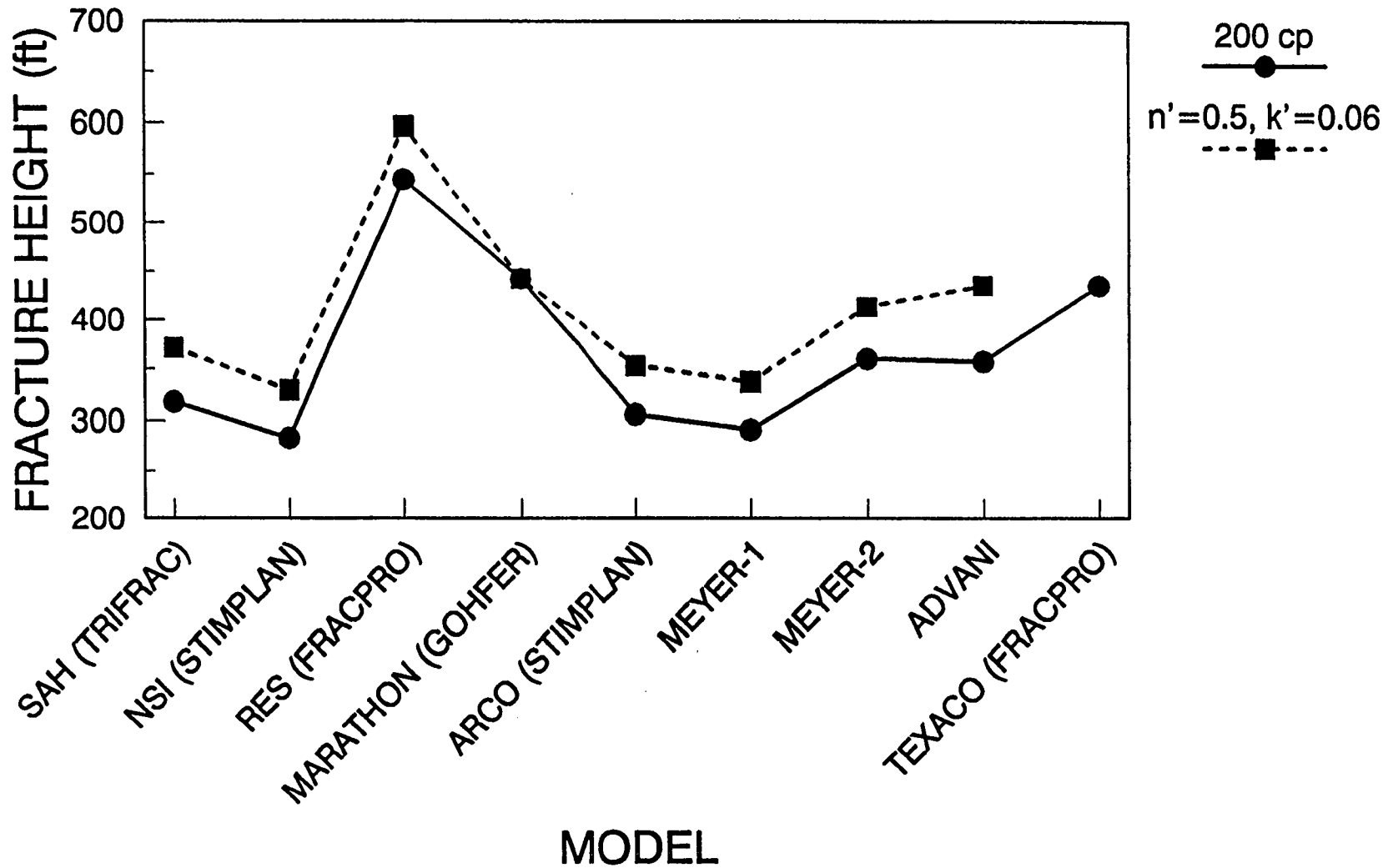


Figure 22. Height comparison for 3-layer cases

FRACTURE NET PRESSURE

3-LAYER MODELS

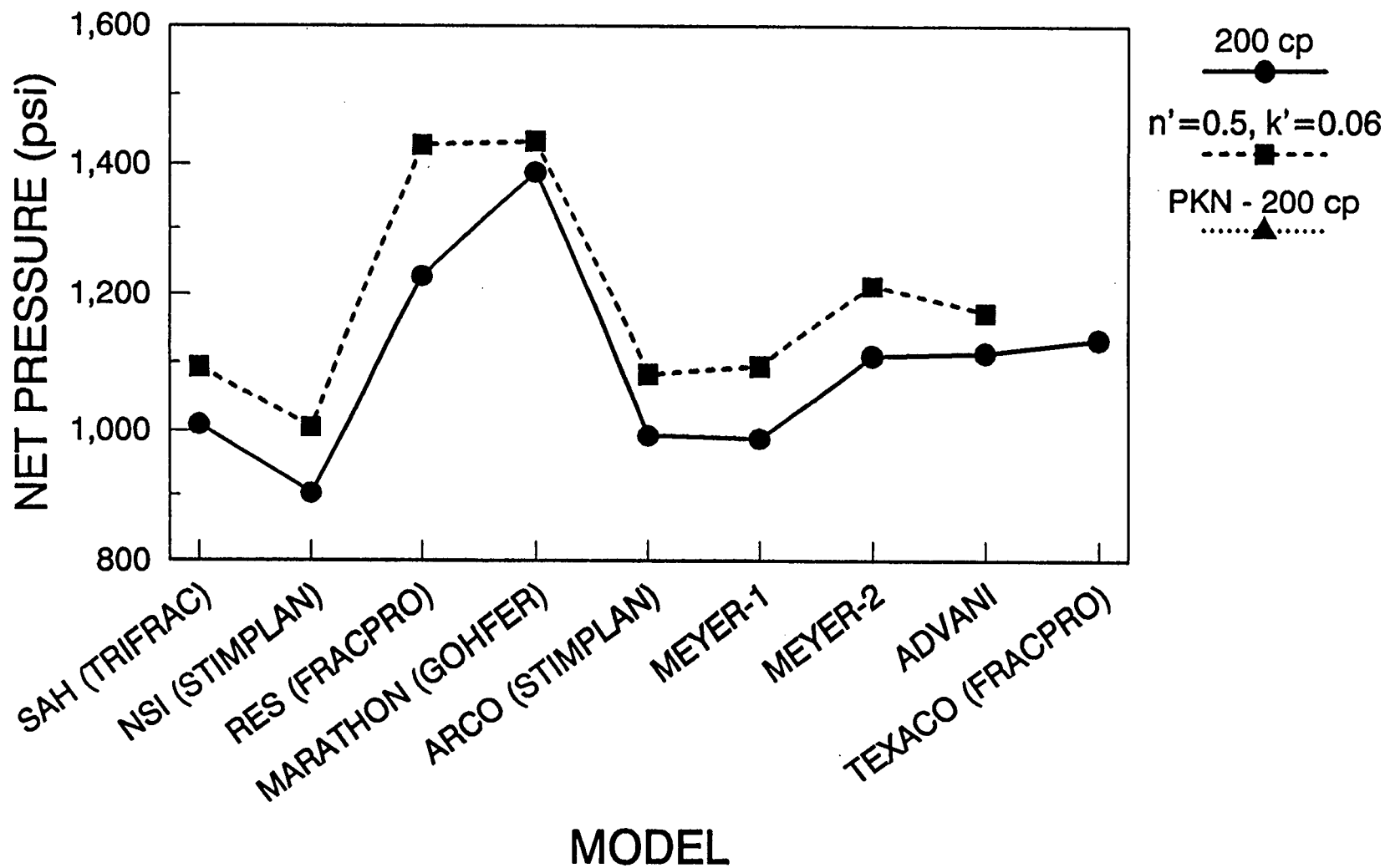


Figure 23. Pressure comparison for 3-layer cases

3-LAYER MODELS: 200 cp

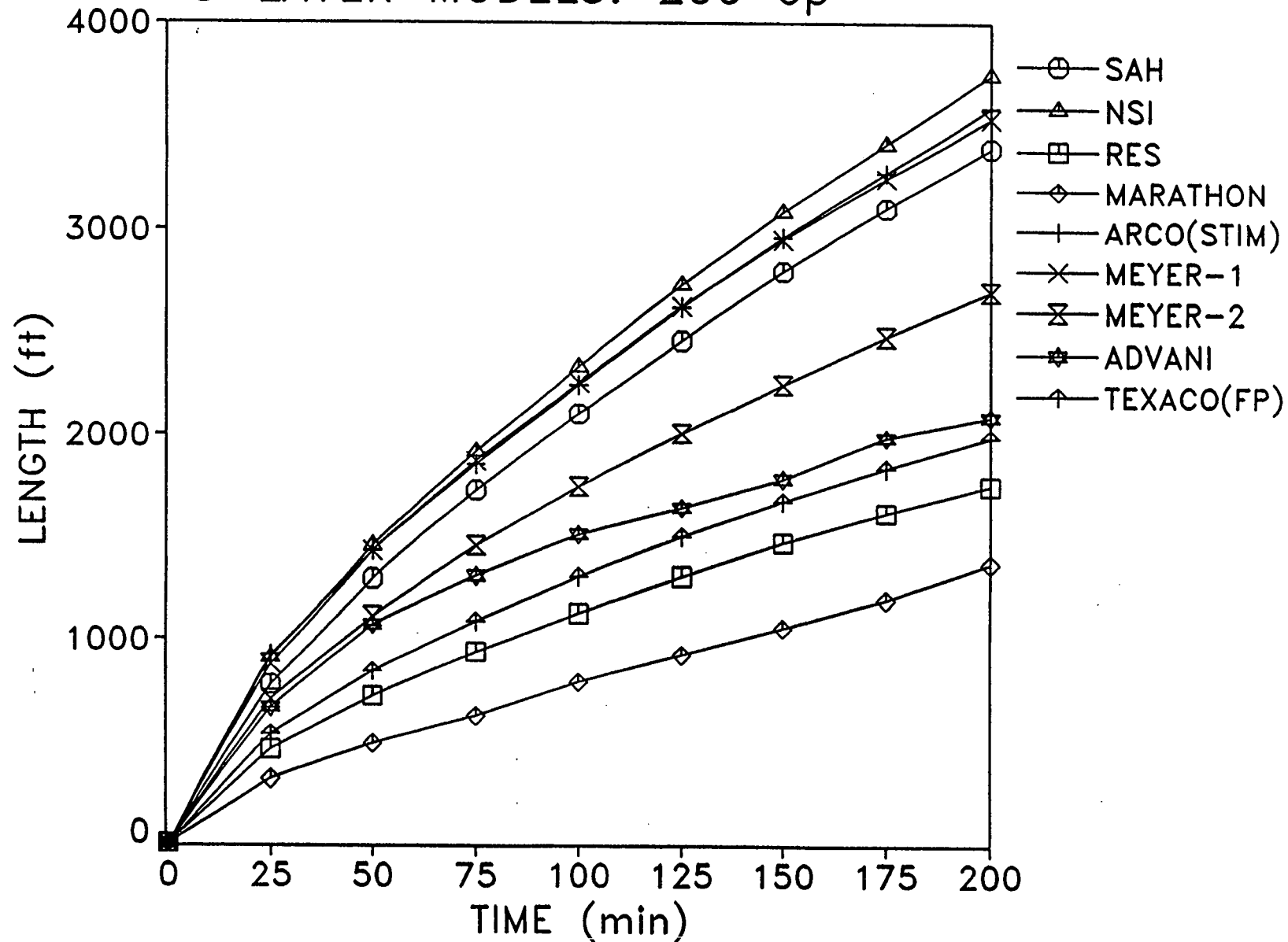


Figure 24. Length vs time for 3-layer Newtonian fluid

3-LAYER MODELS: 200 cp

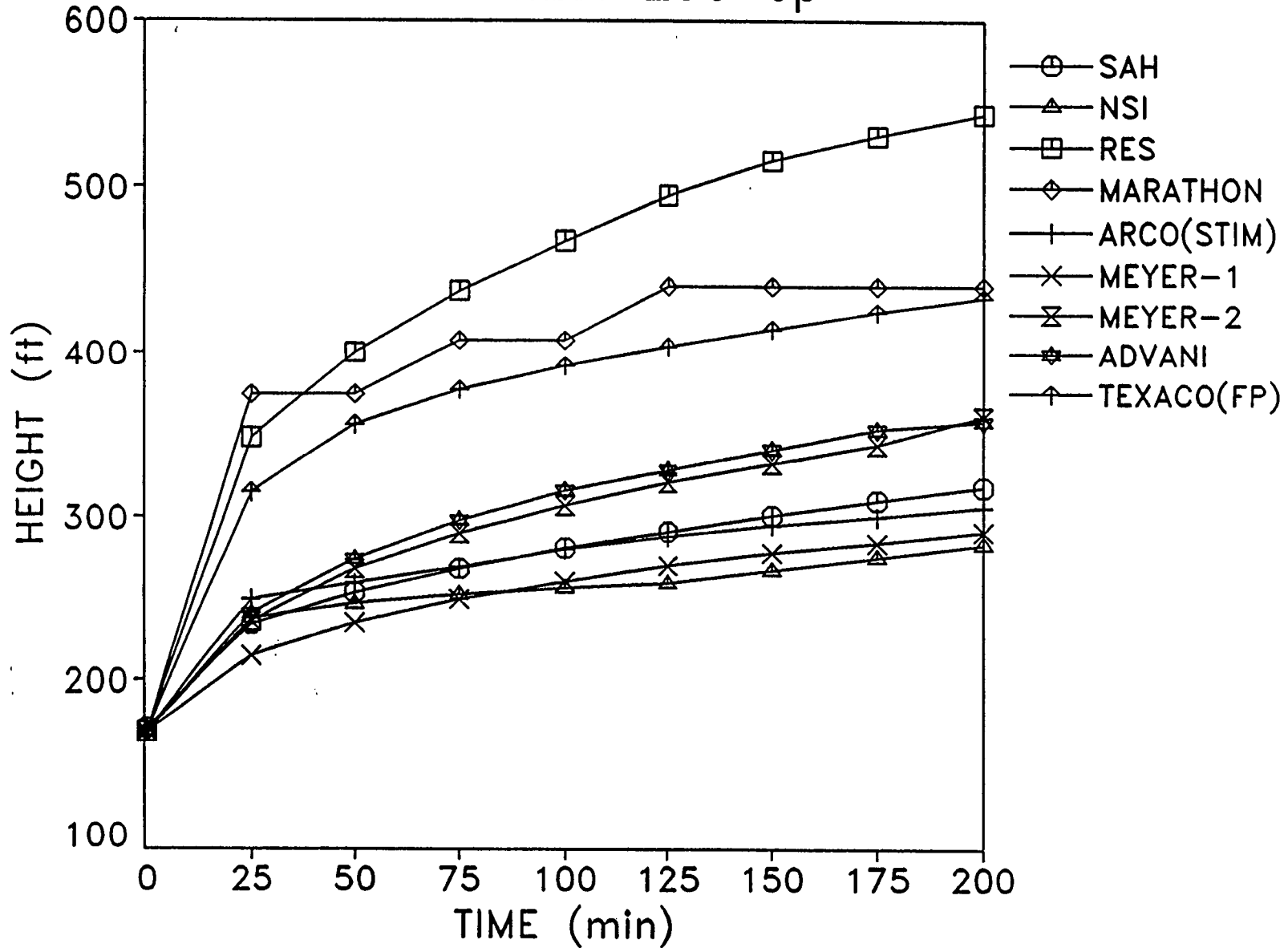


Figure 25. Height vs time for 3-layer Newtonian fluid

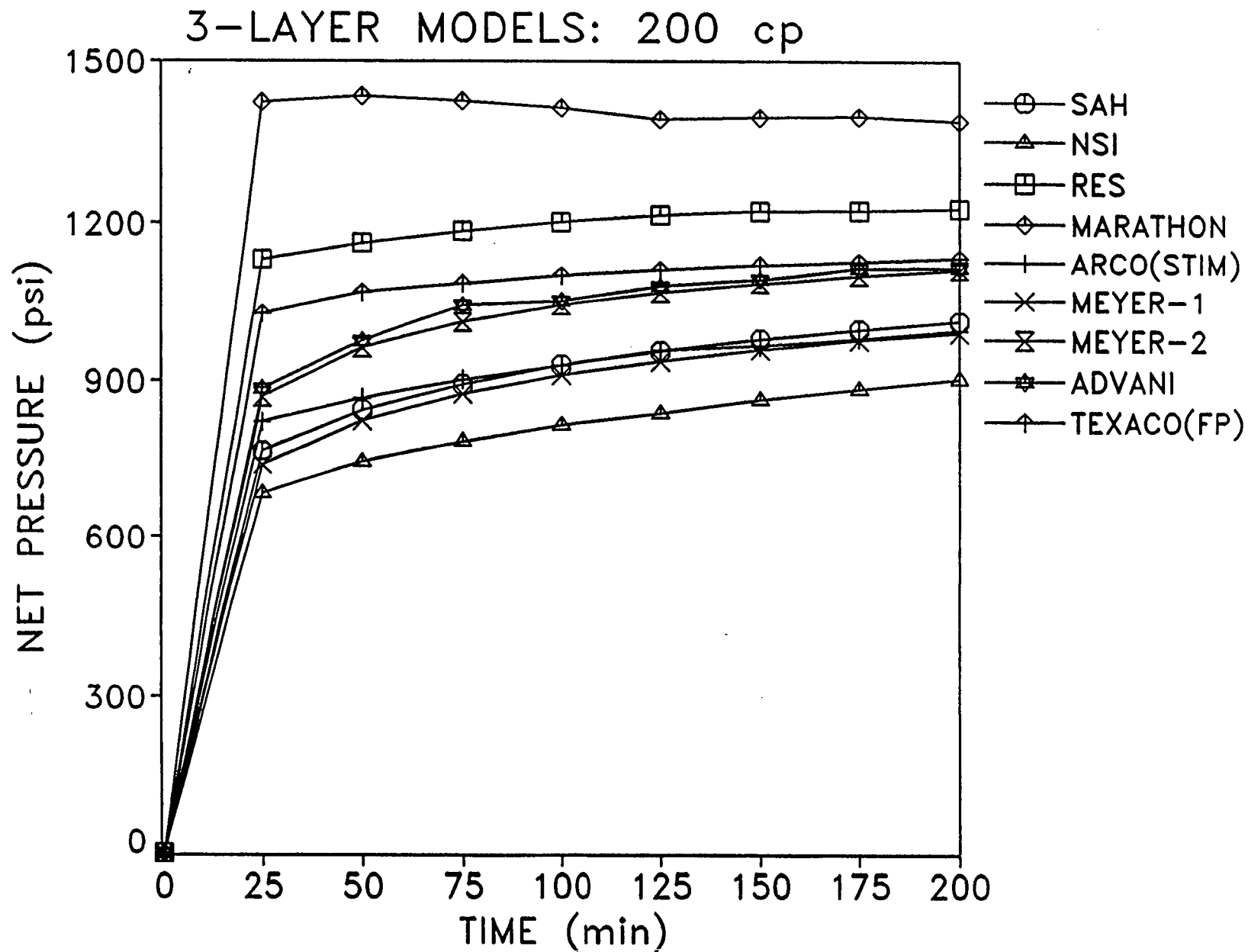


Figure 26. Pressure vs time for 3-layer Newtonian fluid

FRACTURE HALF LENGTH

5-LAYER MODELS

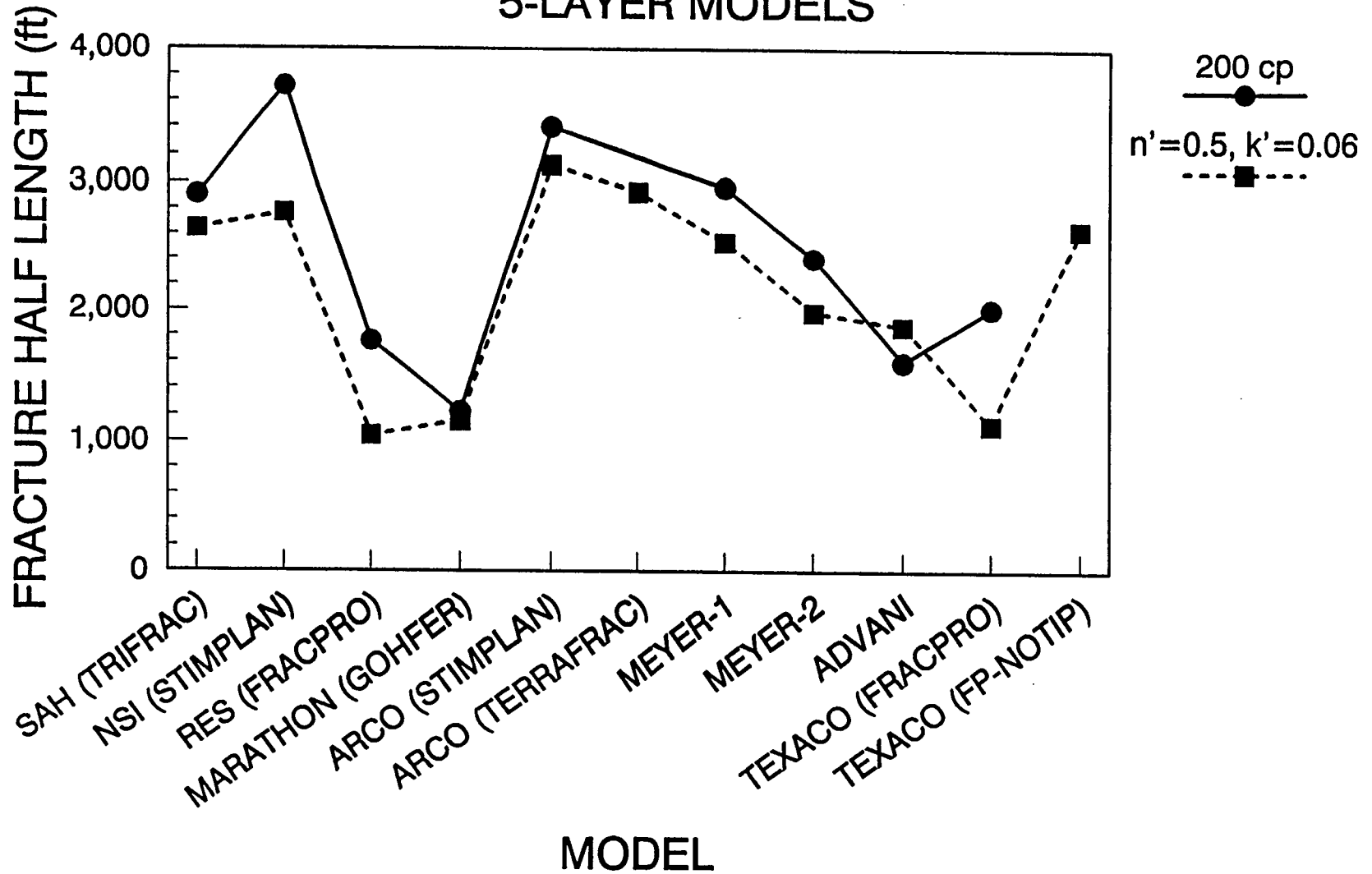


Figure 27. Length comparison for 5-layer cases

FRACTURE HEIGHT

5-LAYER MODELS

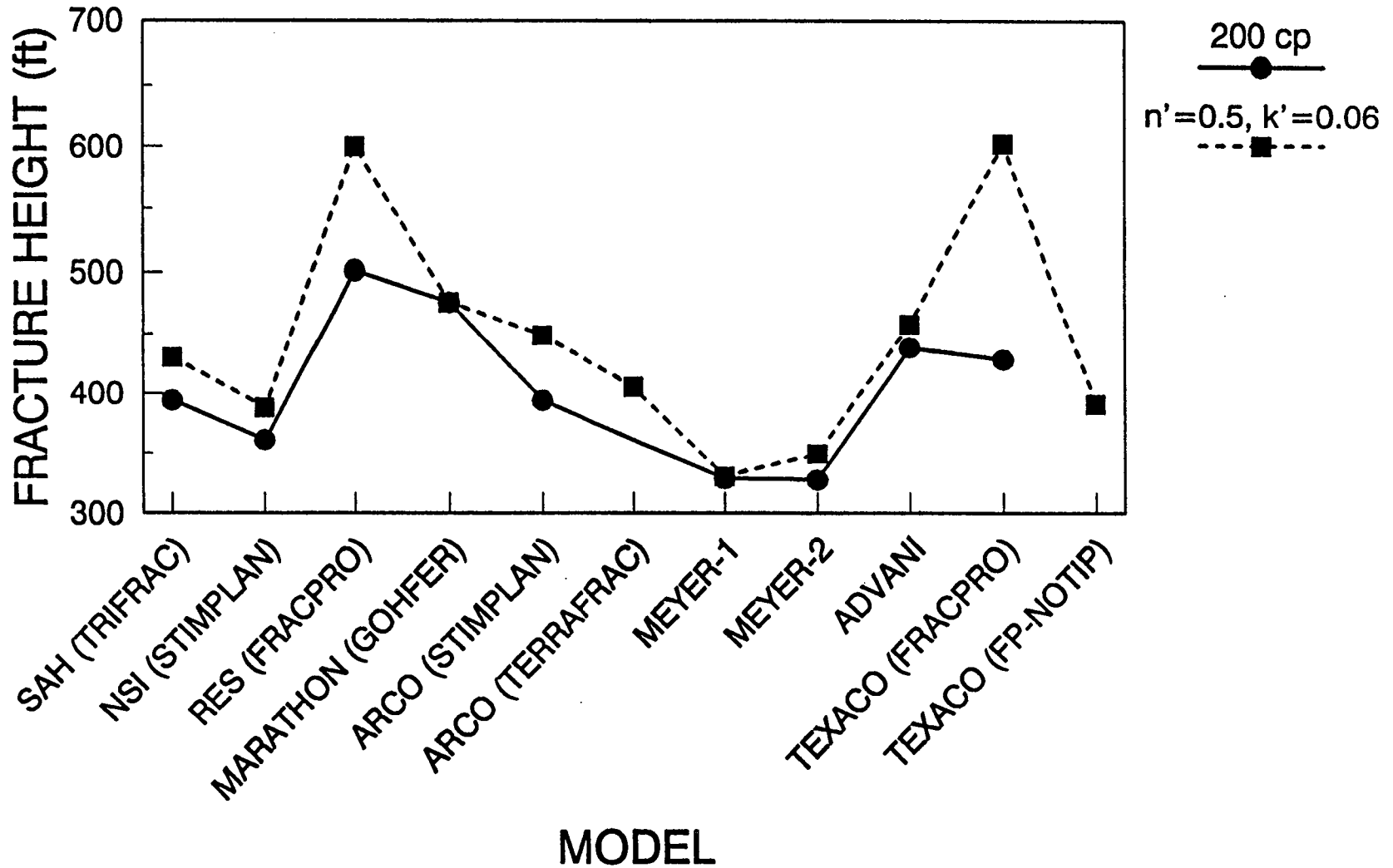


Figure 28. Height comparison for 5-layer cases

FRACTURE NET PRESSURE

5-LAYER MODELS

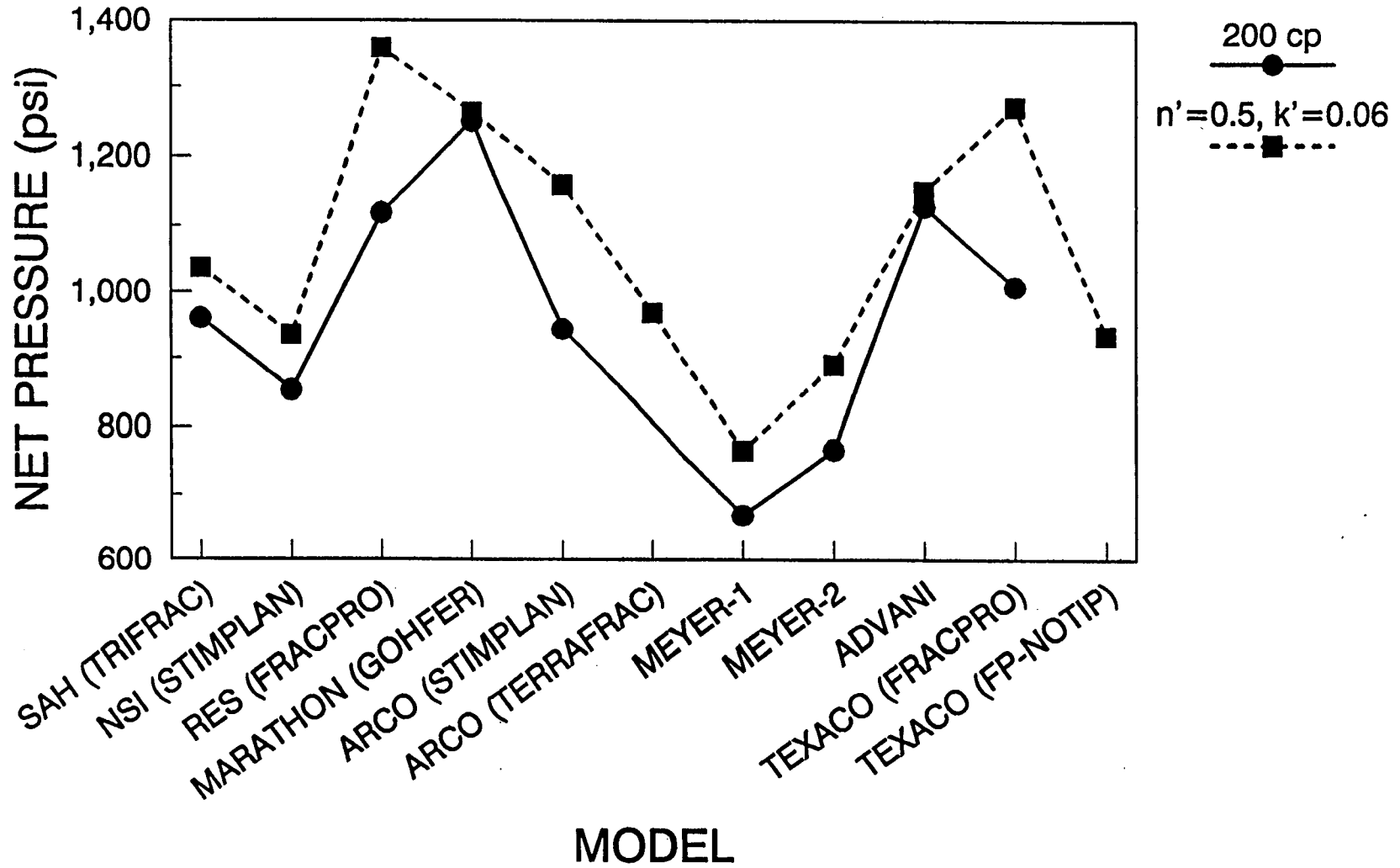


Figure 29. Pressure comparison for 5-layer cases

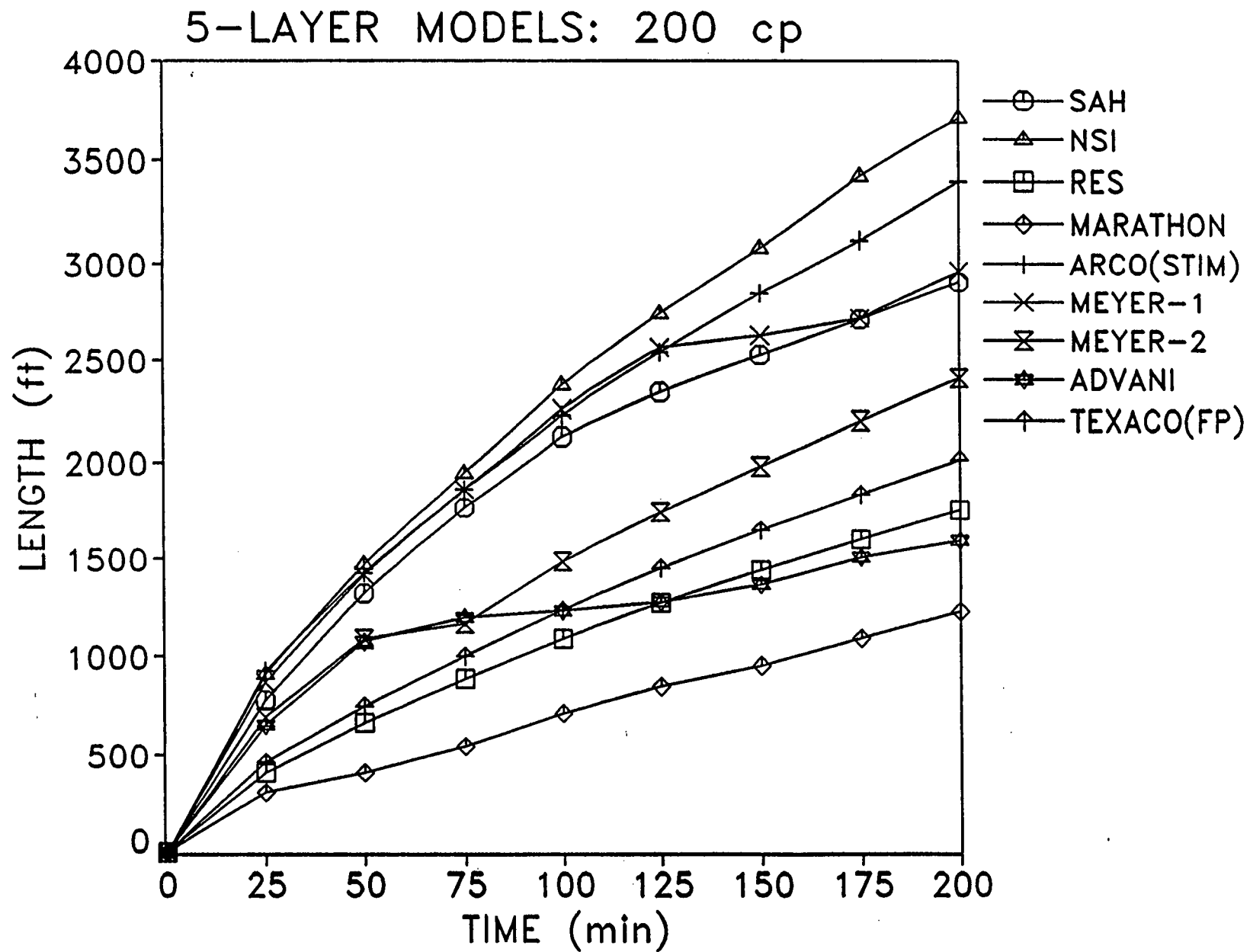


Figure 30. Length vs time for 5-layer Newtonian fluid

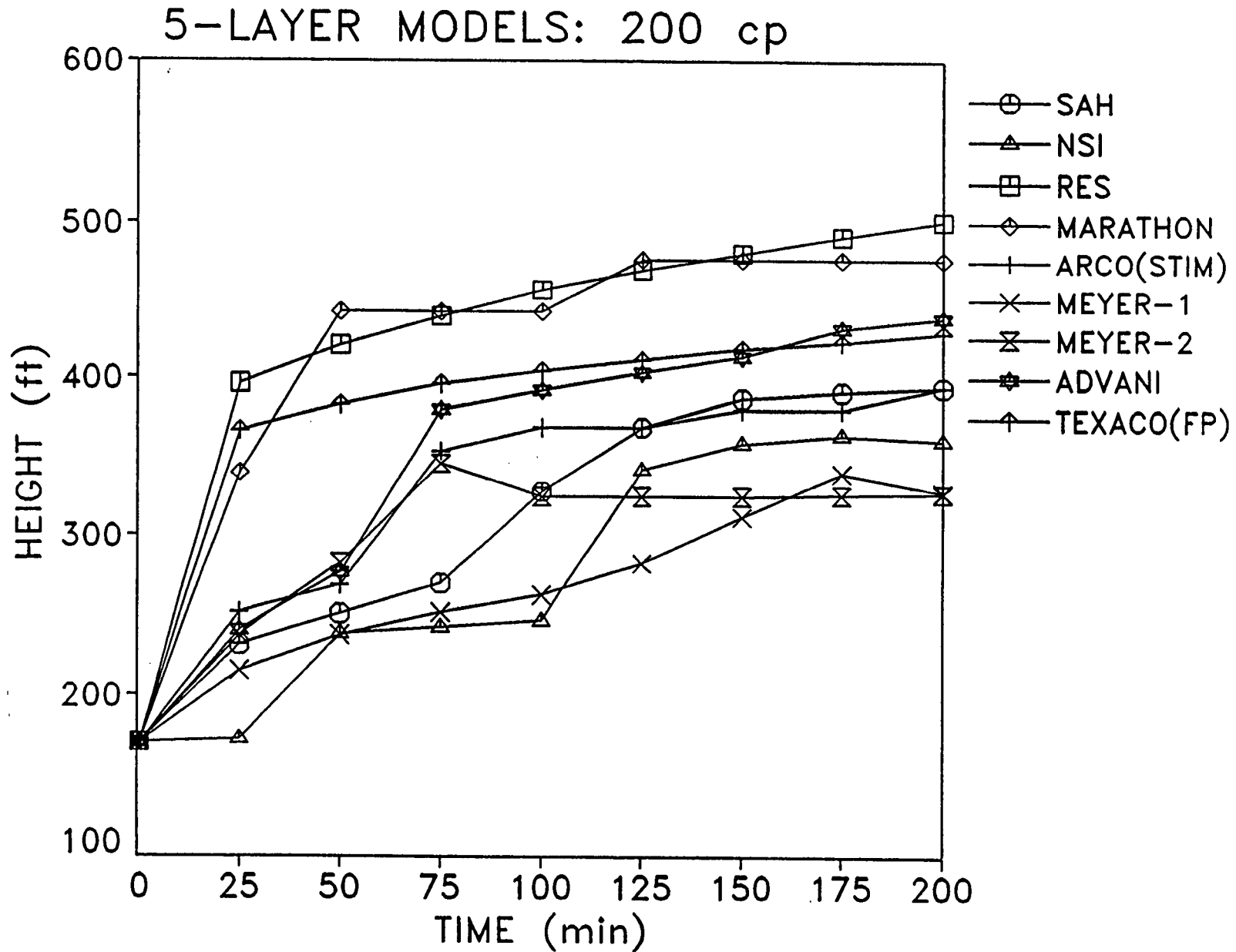


Figure 31. Height vs time for 5-layer Newtonian fluid

5-LAYER MODELS: 200 cp

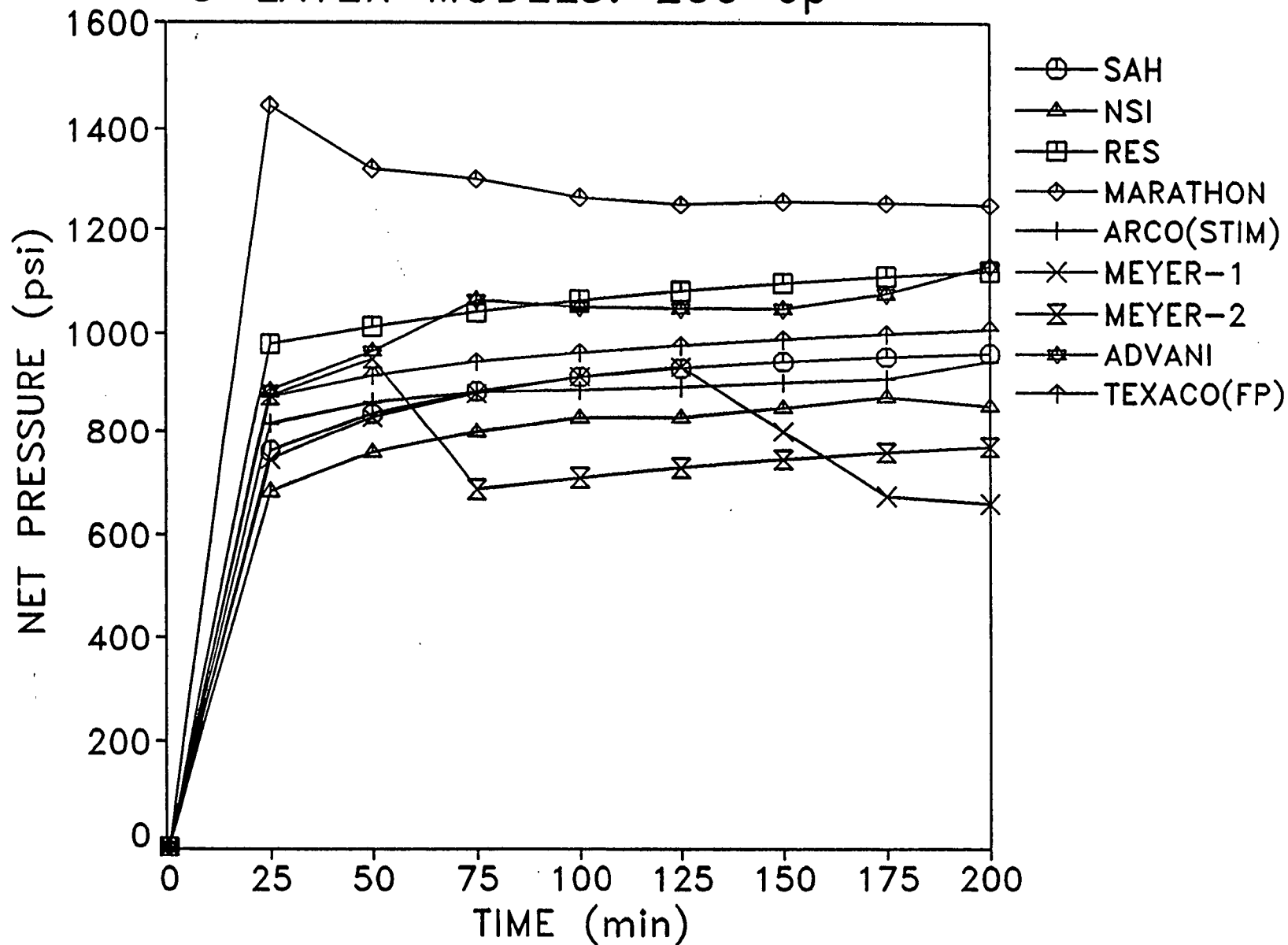
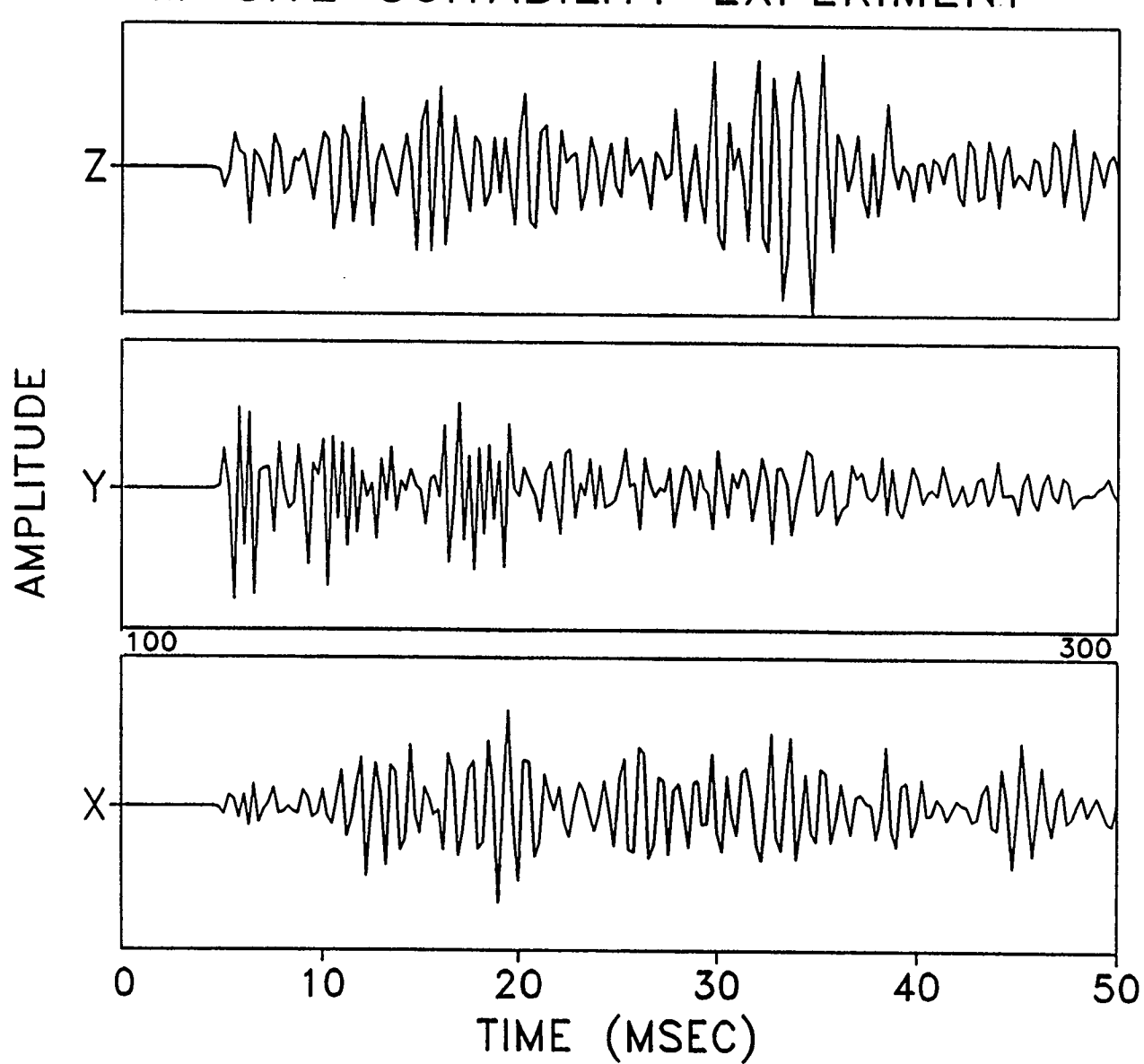


Figure 32. Pressure vs time for 5-layer Newtonian fluid

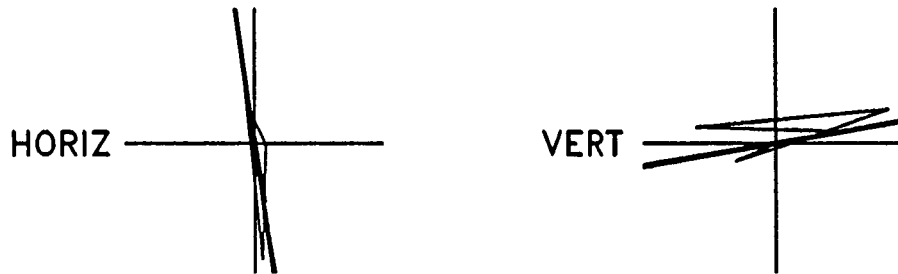
M-SITE SUITABILITY EXPERIMENT



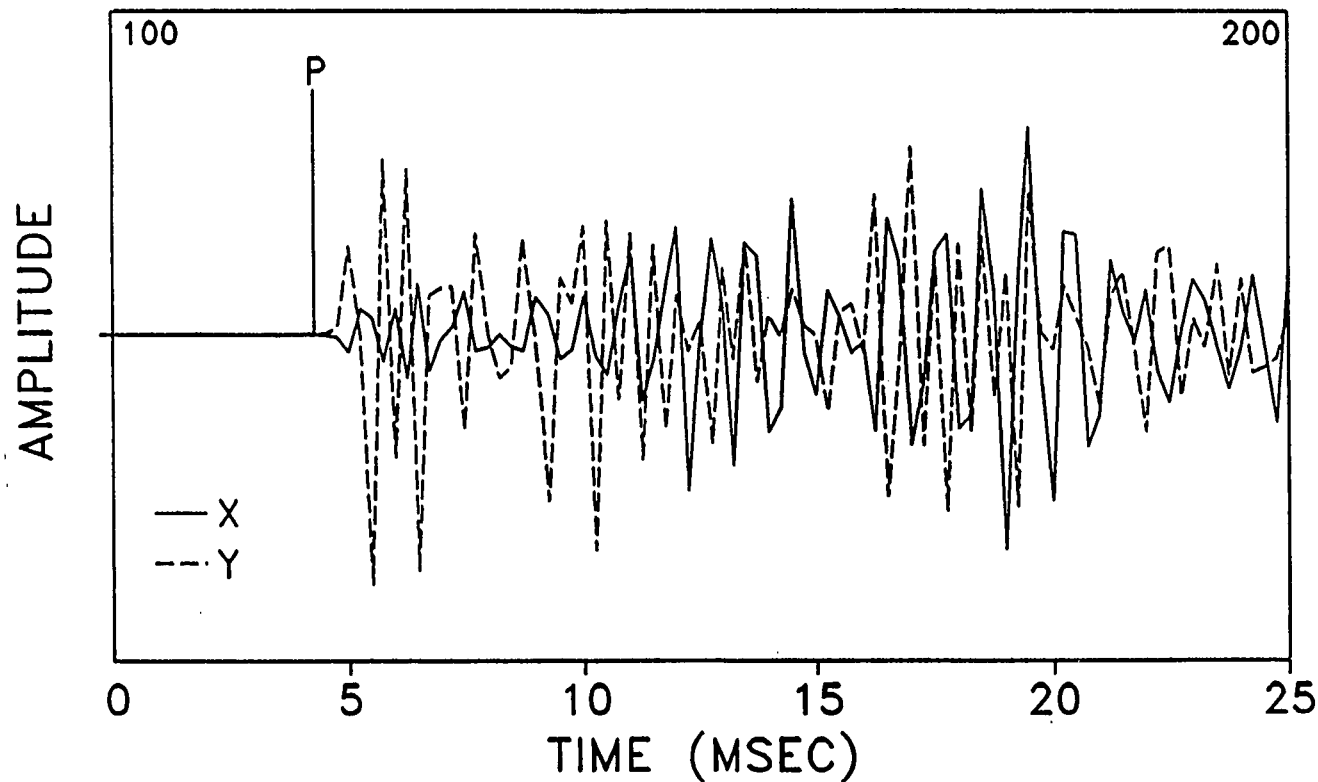
MWX-2
10/13/92
MSPRF2 4.DAT
SCALE=21.8
SAMP INT:
0.250 ms
1200 PTS

Figure 33. Perforation event - all traces

M-SITE SUITABILITY EXPERIMENT



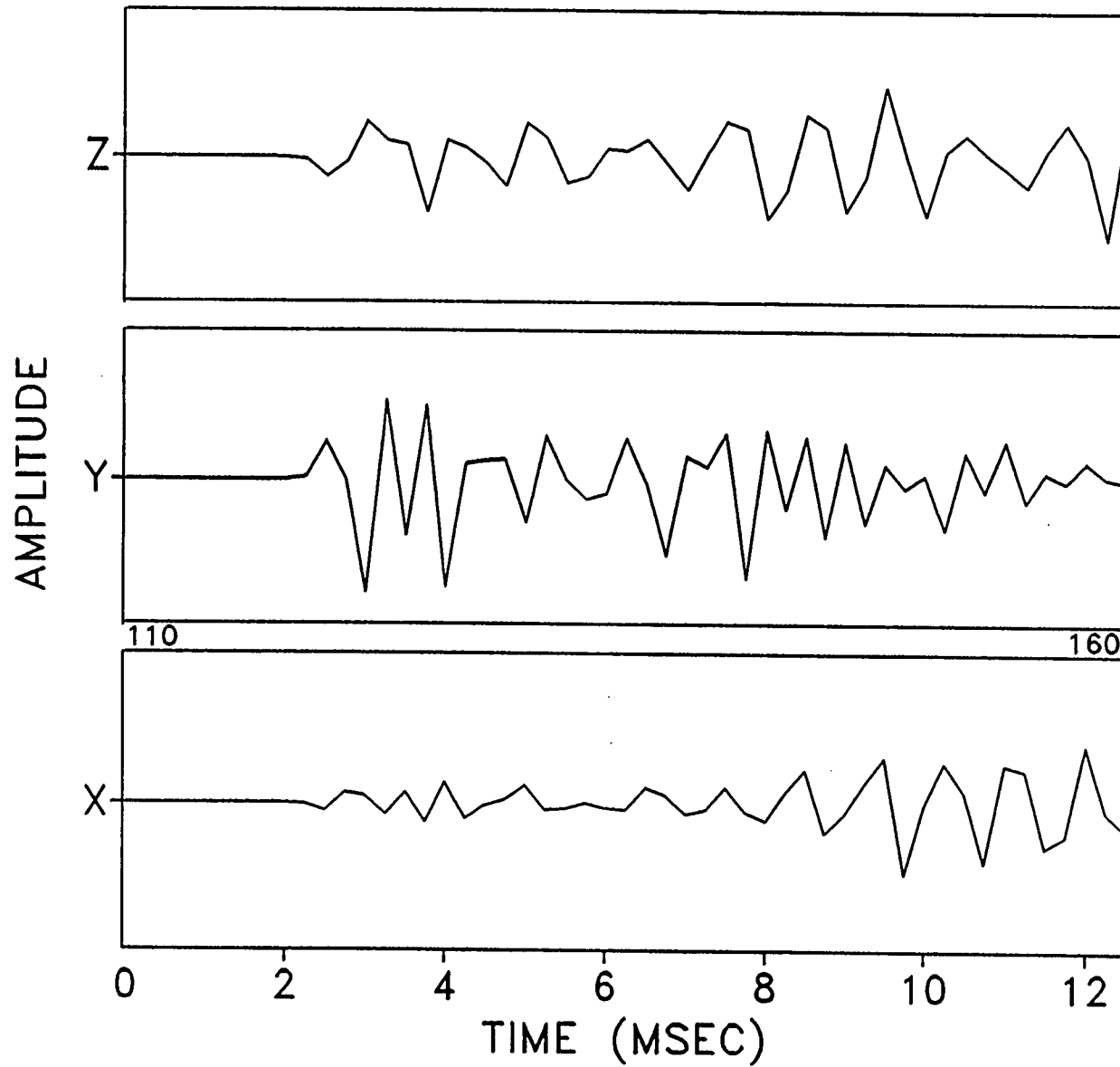
HODOGRAM
P: 117: 4.25 ms
TO 126: 6.50 ms
H: -81.8 SD: 11.6
V: 10.1 SD: 15.5
RMS H: 81.7 V: 16.4
VEL FAC: 25.0
DISTANCE: -731



MWX-2
10/13/92
MSPRF2 4.DAT
SCALE=21.8
SAMP INT:
0.250 ms
1200 PTS

Figure 34. Perforation event - hodograms

M-SITE SUITABILITY EXPERIMENT



MWX-2
10/13/92
MSPRF2 4.DAT
SCALE=21.8
SAMP INT:
0.250 ms
1200 PTS

Figure 35. Perforation event - all traces, expanded view

HISTOGRAM OF MICROSEISMIC SIGNALS

M-SITE BREAKDOWN/BALLOUT 10/14/92

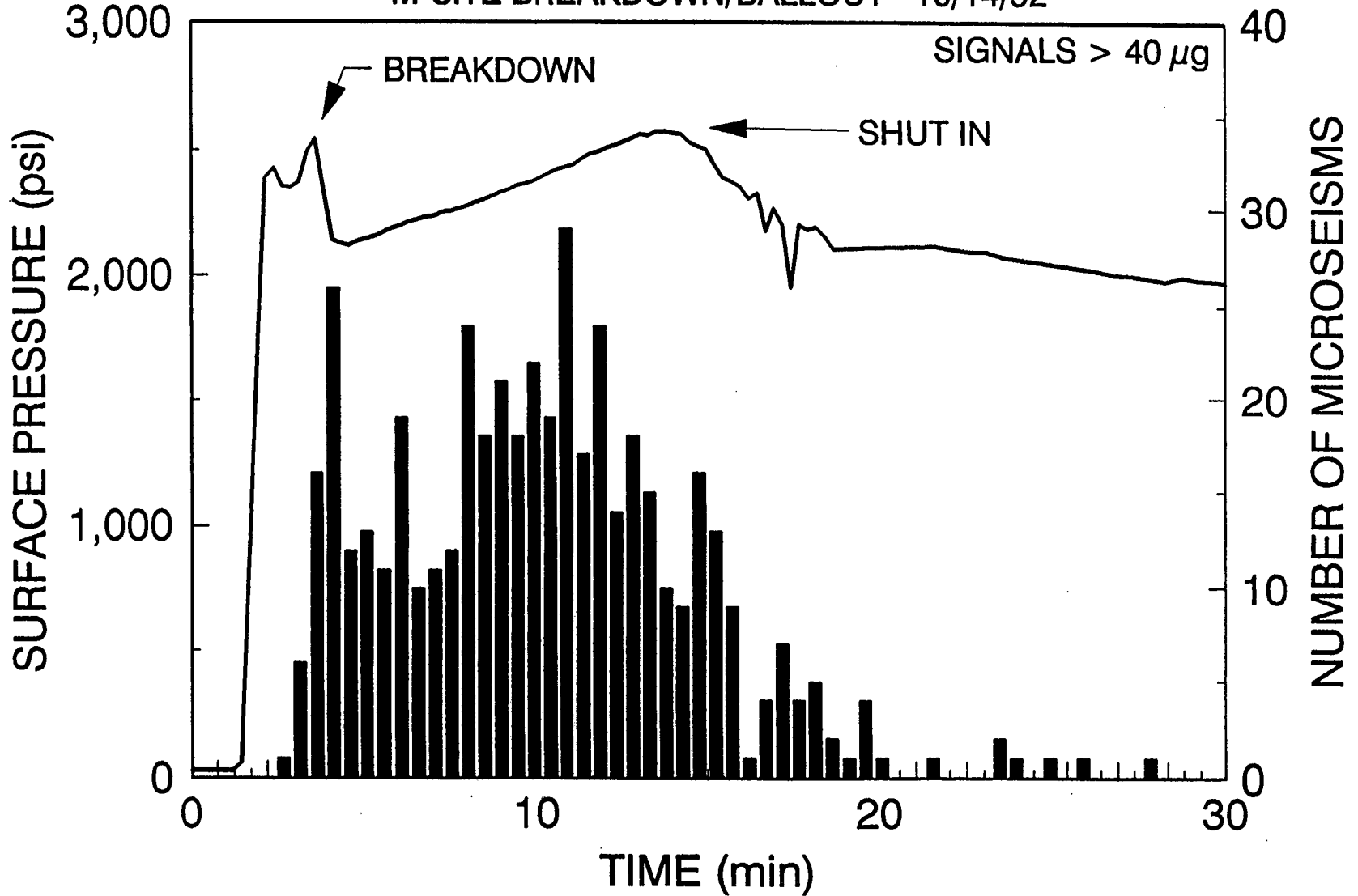


Figure 36. Histogram of events correlated with pressure during breakdown

HISTOGRAM OF MICROSEISMIC SIGNALS

M-SITE STEP RATE TEST 10/14/92

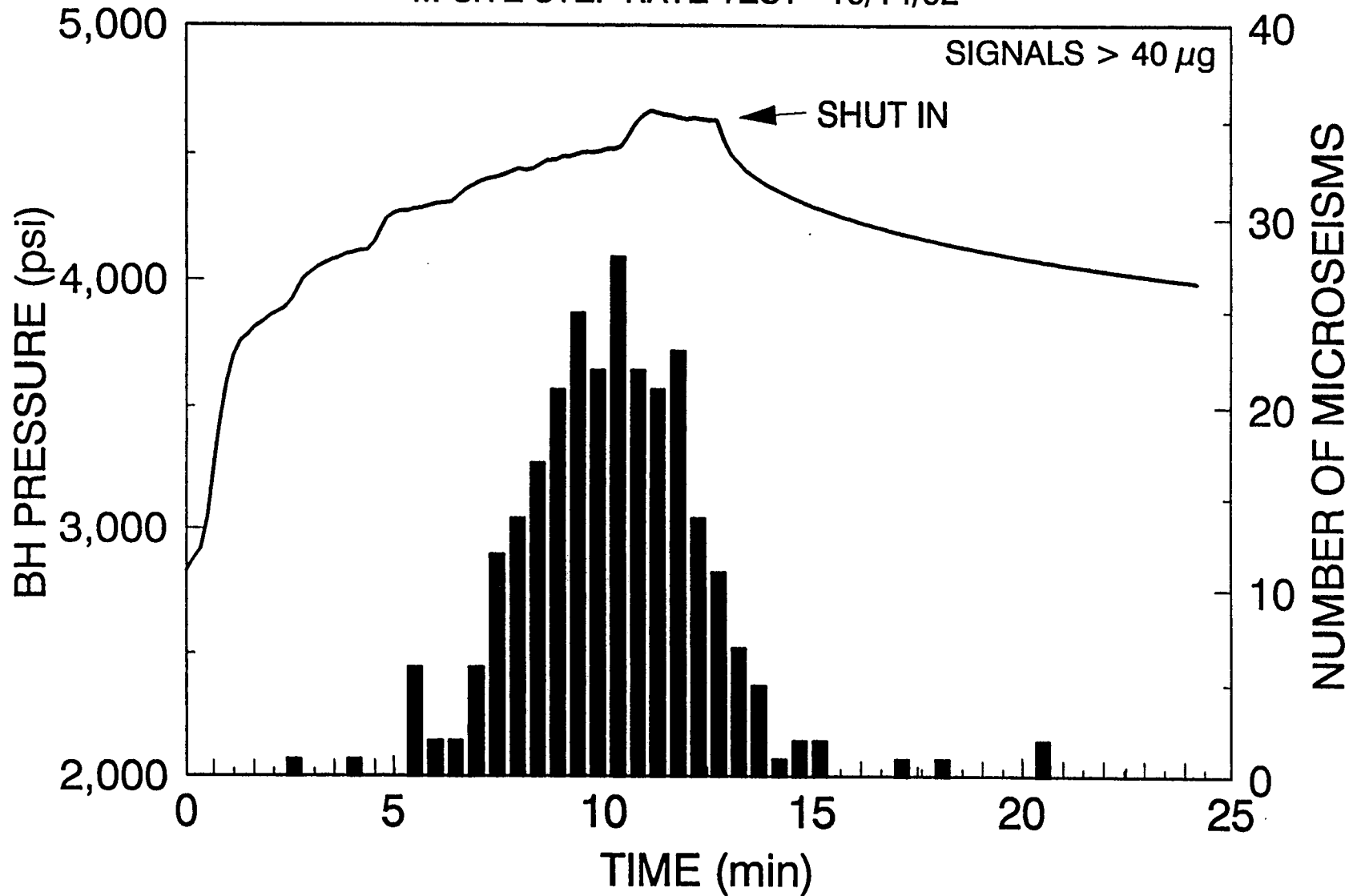


Figure 37. Histogram of events correlated with pressure during step-rate test

HISTOGRAM OF MICROSEISMIC SIGNALS

M-SITE KCL MINIFRAC 10/14/92

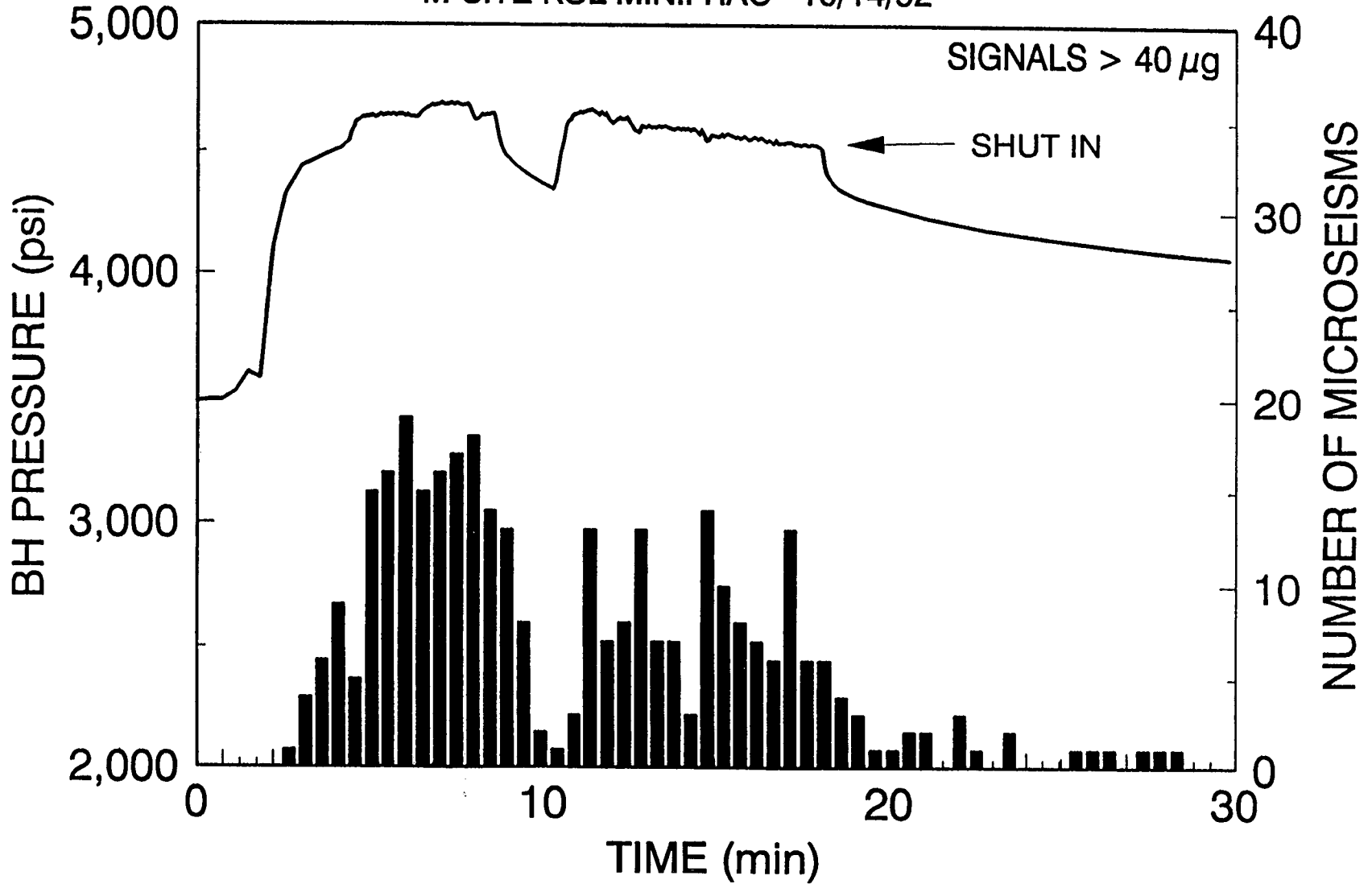


Figure 38. Histogram of events correlated with pressure during KCl minifrac

HISTOGRAM OF MICROSEISMIC SIGNALS

M-SITE GEL MINIFRAC 10/15/92

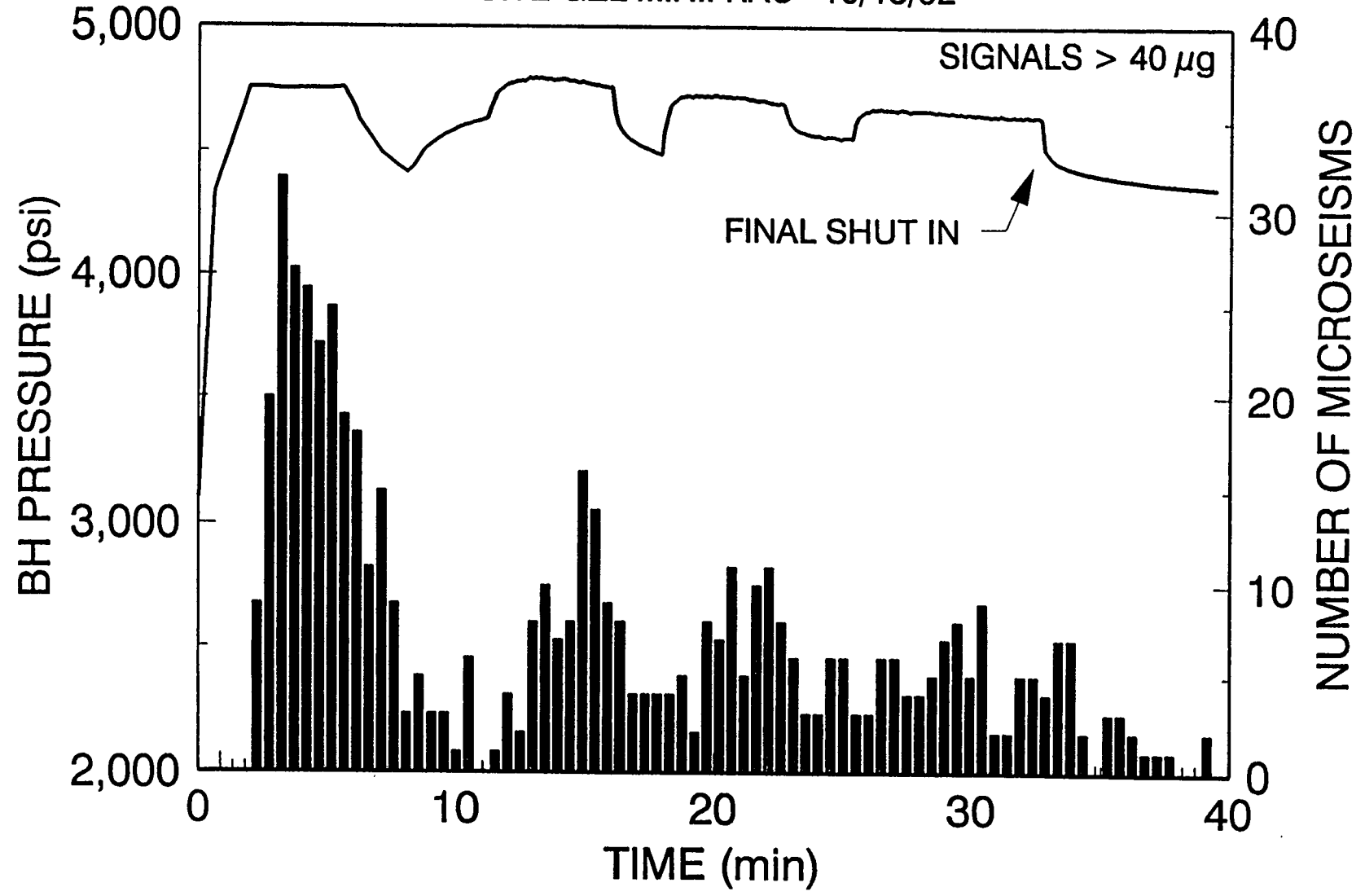


Figure 39. Histogram of events correlated with pressure during gel minifrac

PLAN VIEW OF MICROSEISMIC LOCATIONS

M-SITE EXPERIMENTS 10/14-15/92

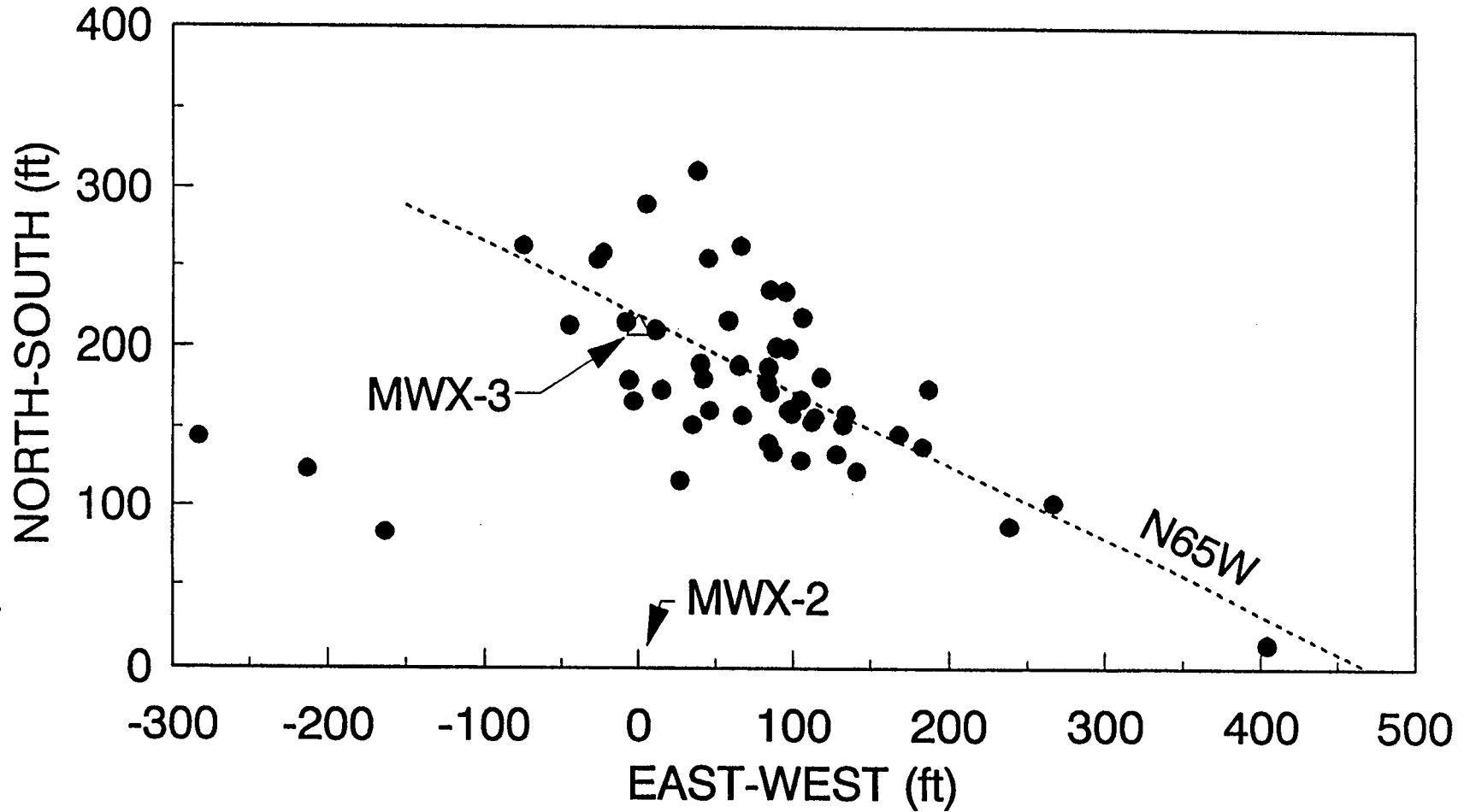


Figure 40. Plan view of microseismic locations

SIDE VIEW OF MICROSEISMIC LOCATIONS

M-SITE EXPERIMENTS 10/14-15/92

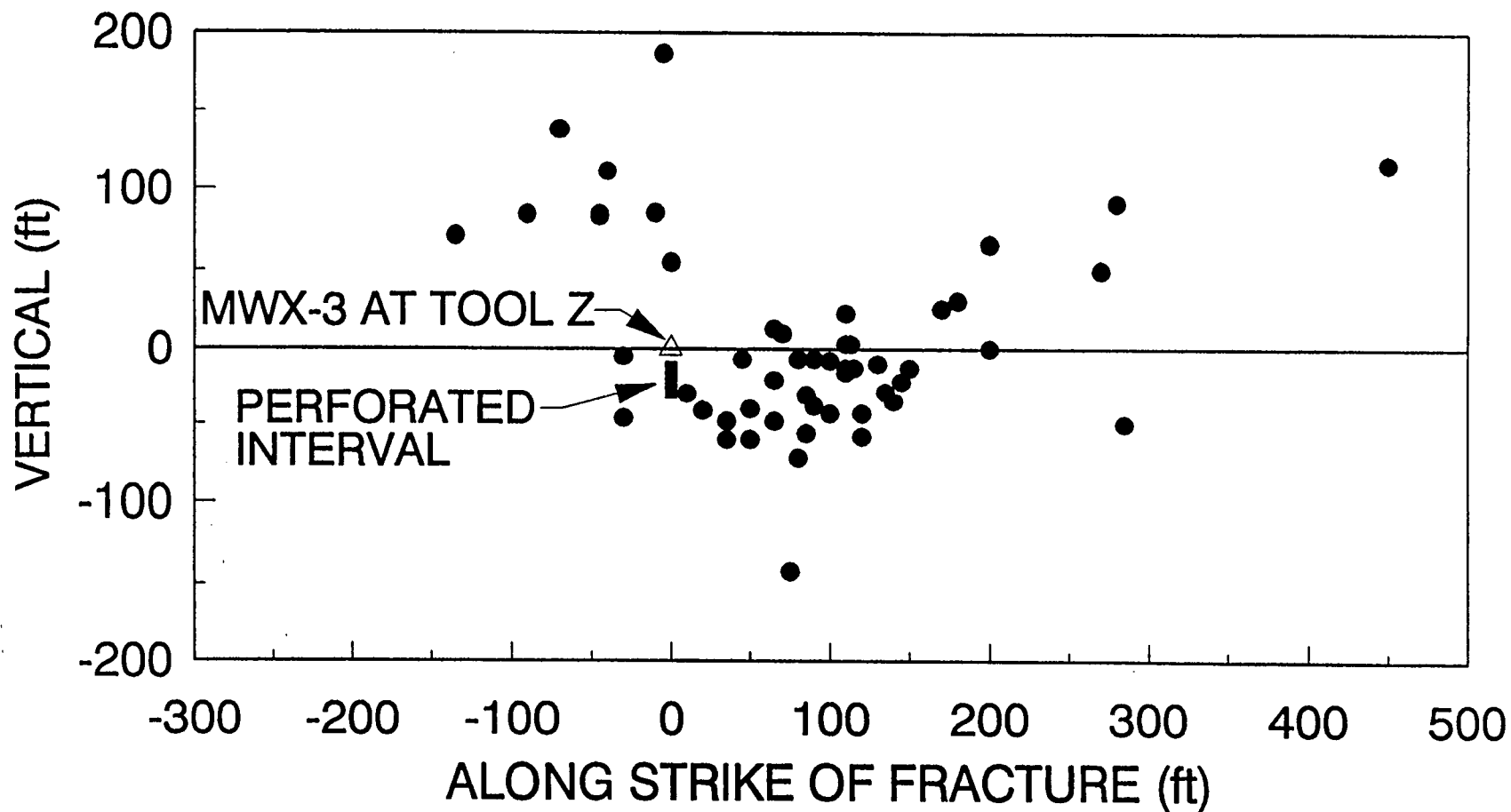
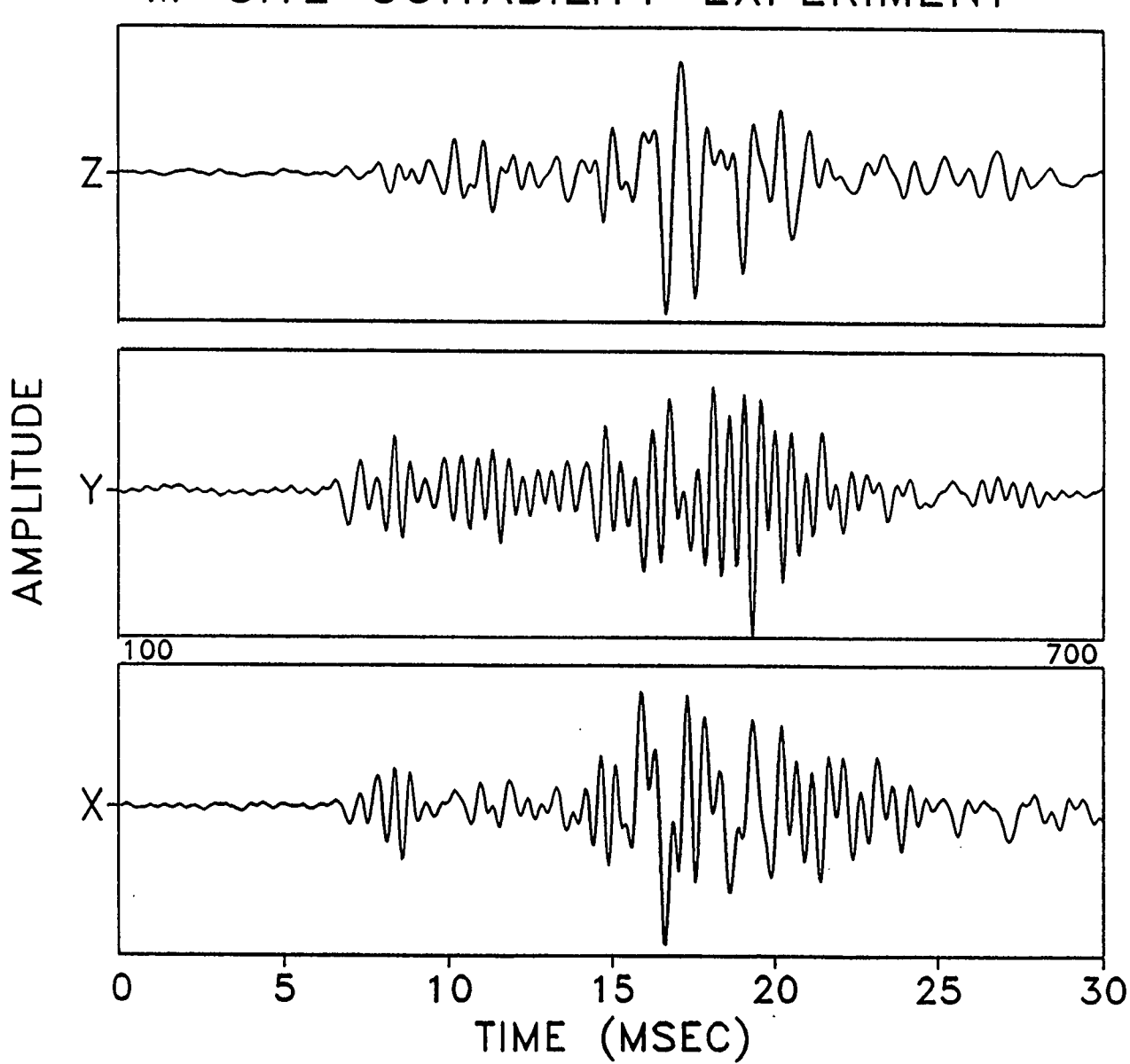


Figure 41. Side view of microseism locations

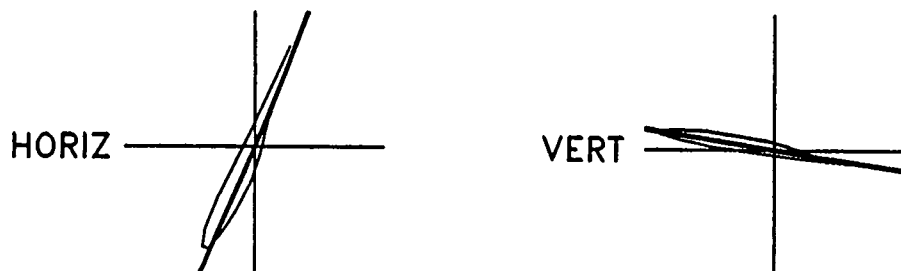
M-SITE SUITABILITY EXPERIMENT



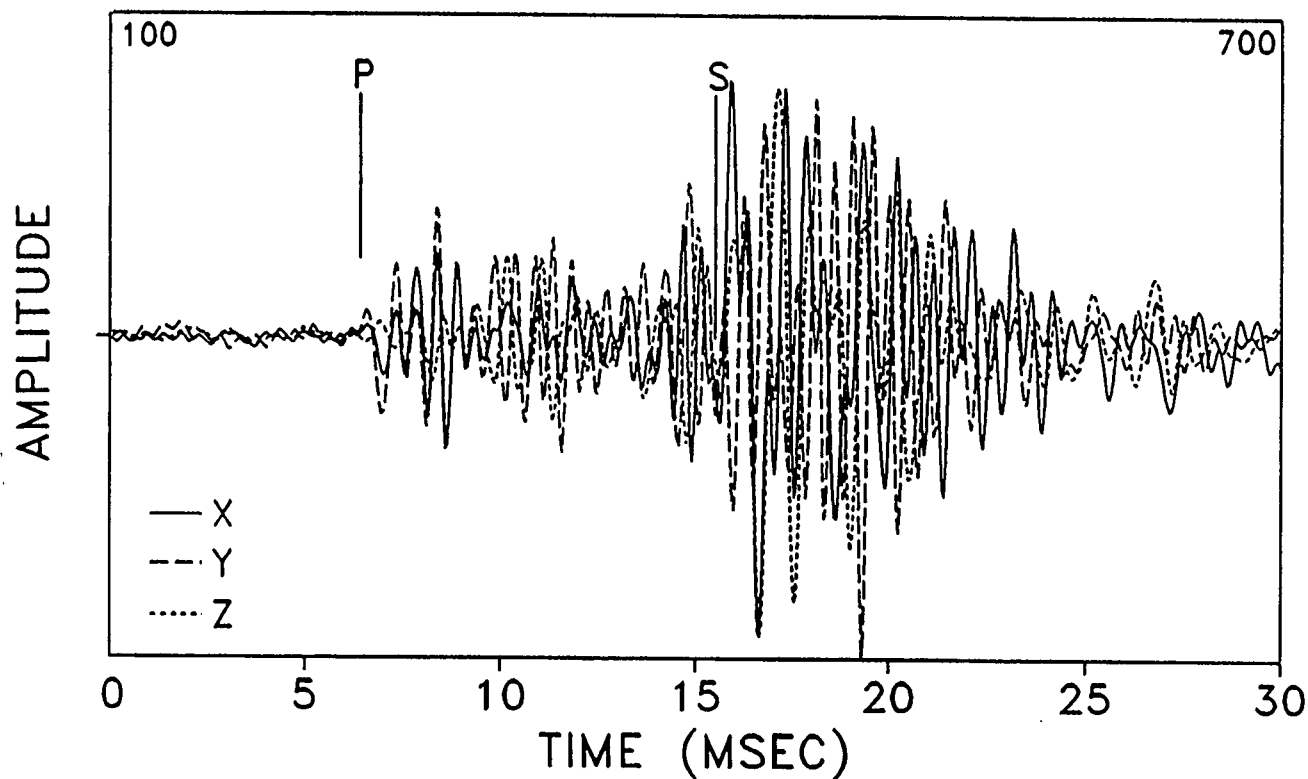
MWX-2
10/14/92
MS33.DAT
SCALE=50.6
SAMP INT:
0.050 ms
1200 PTS

Figure 42. Microseism traces for event 33, unfiltered

M-SITE SUITABILITY EXPERIMENT



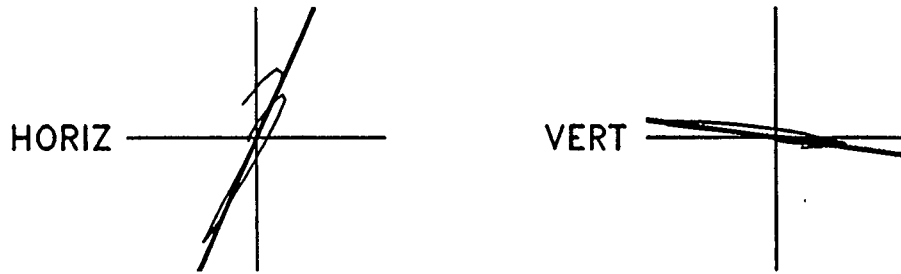
HODOGRAM
P: 228: 6.40 ms
TO 249: 7.45 ms
S: 410: 15.50 ms
H: 67.6 SD: 8.7
V: -9.1 SD: 6.5
RMS H: 66.7 V: 9.8
VEL FAC: 25.0
DISTANCE: 227



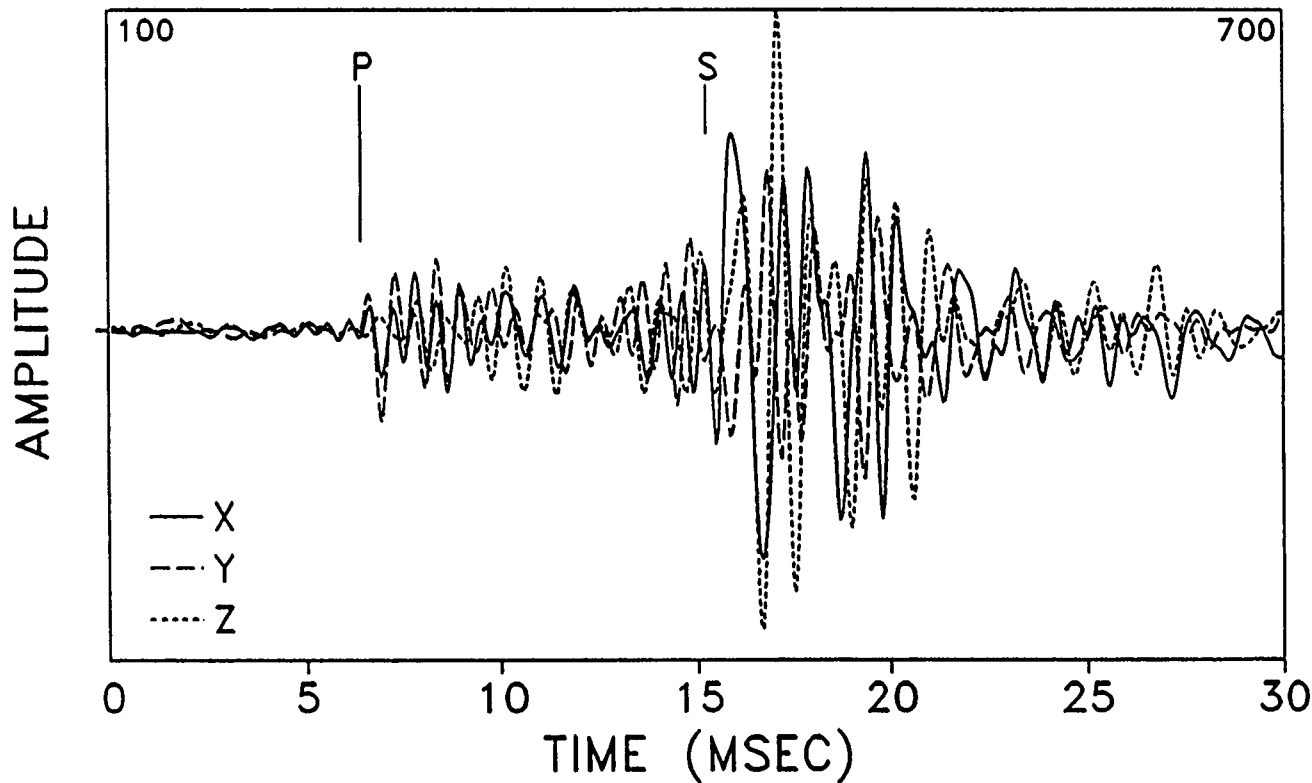
MWX-2
10/14/92
MS33.DAT
SCALE=50.6
SAMP INT:
0.050 ms
1200 PTS

Figure 43. Hodogram for event 33, unfiltered

M-SITE SUITABILITY



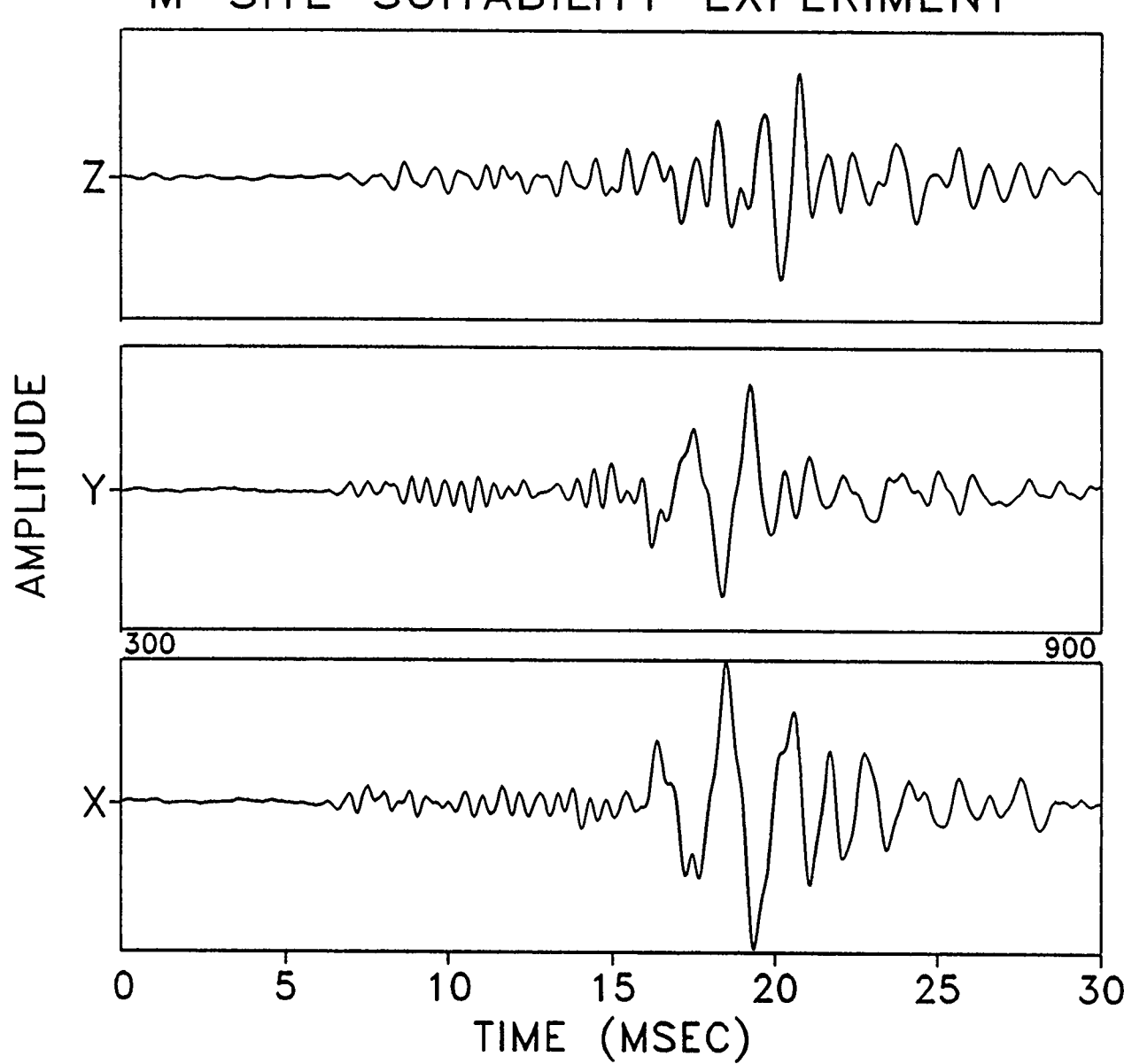
HODOGRAM
P: 228: 6.40 ms
TO 250: 7.50 ms
S: 405: 15.25 ms
H: 66.0 SD: 14.0
V: -7.9 SD: 7.6
RMS H: 64.0 V: 8.6
VEL FAC: 25.0
DISTANCE: 221



MWX-2
10/14/92
MSF33.DAT
SCALE=46.3
SAMP INT:
0.050 ms
1200 PTS

Figure 44. Hodogram for event 33, filtered

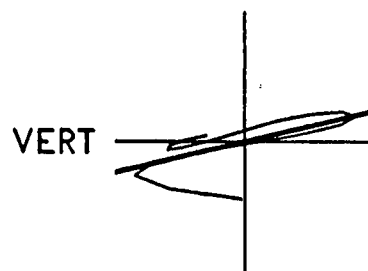
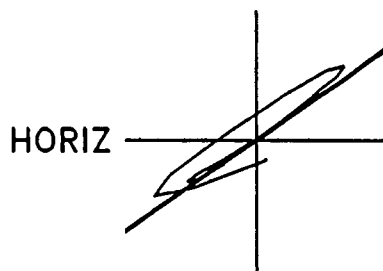
M-SITE SUITABILITY EXPERIMENT



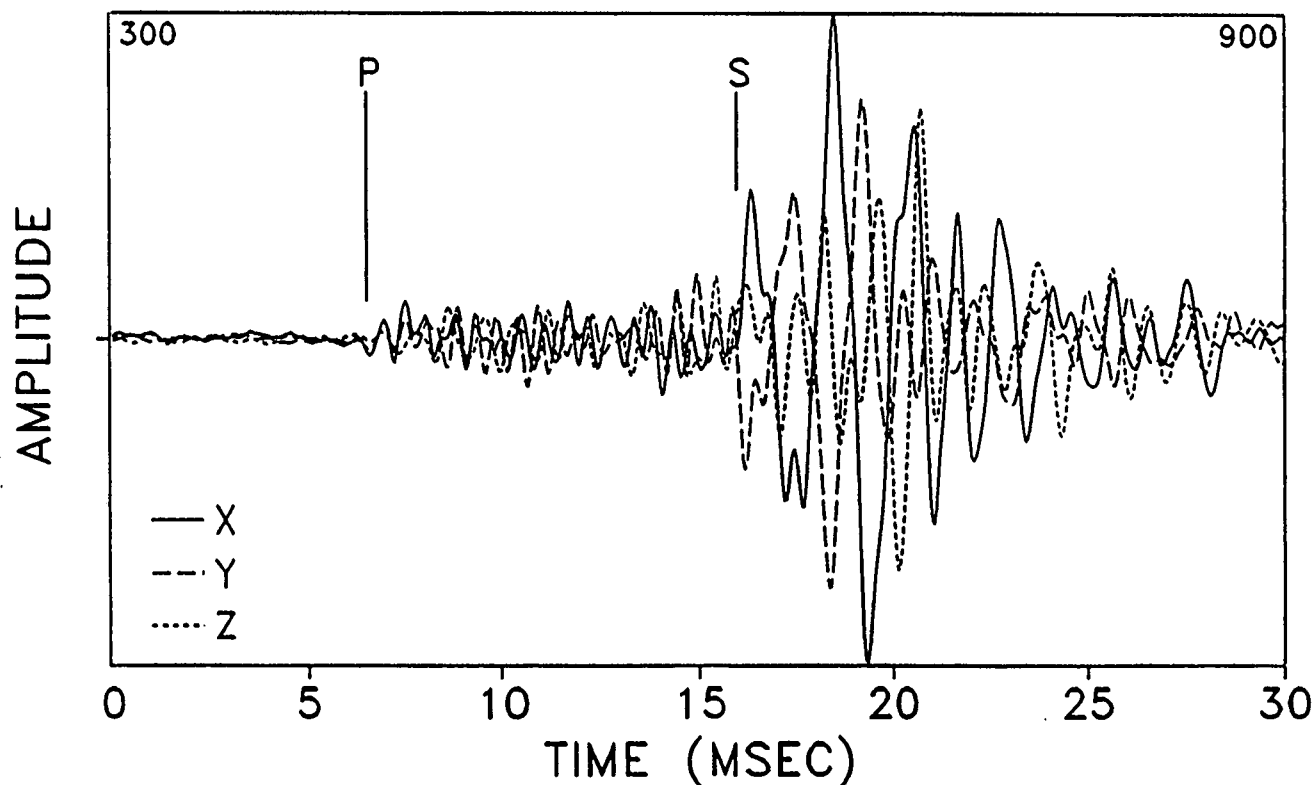
MWX-2
10/14/92
MS34.DAT
SCALE=76.7
SAMP INT:
0.050 ms
1200 PTS

Figure 45. Microseism traces for event 34, unfiltered

M-SITE SUITABILITY EXPERIMENT



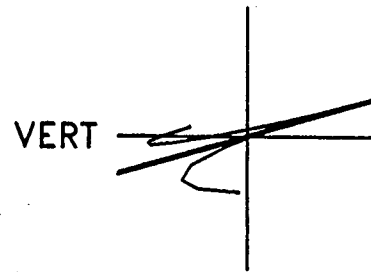
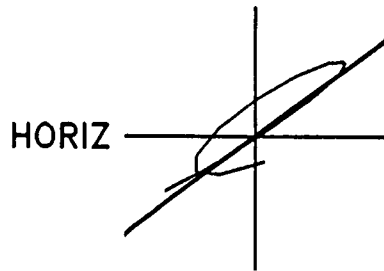
HODOGRAM
P: 430: 6.50 ms
TO 448: 7.40 ms
S: 620: 16.00 ms
H: 35.3 SD: 12.9
V: 13.5 SD: 17.1
RMS H: 36.1 V: 19.3
VEL FAC: 25.0
DISTANCE: 237



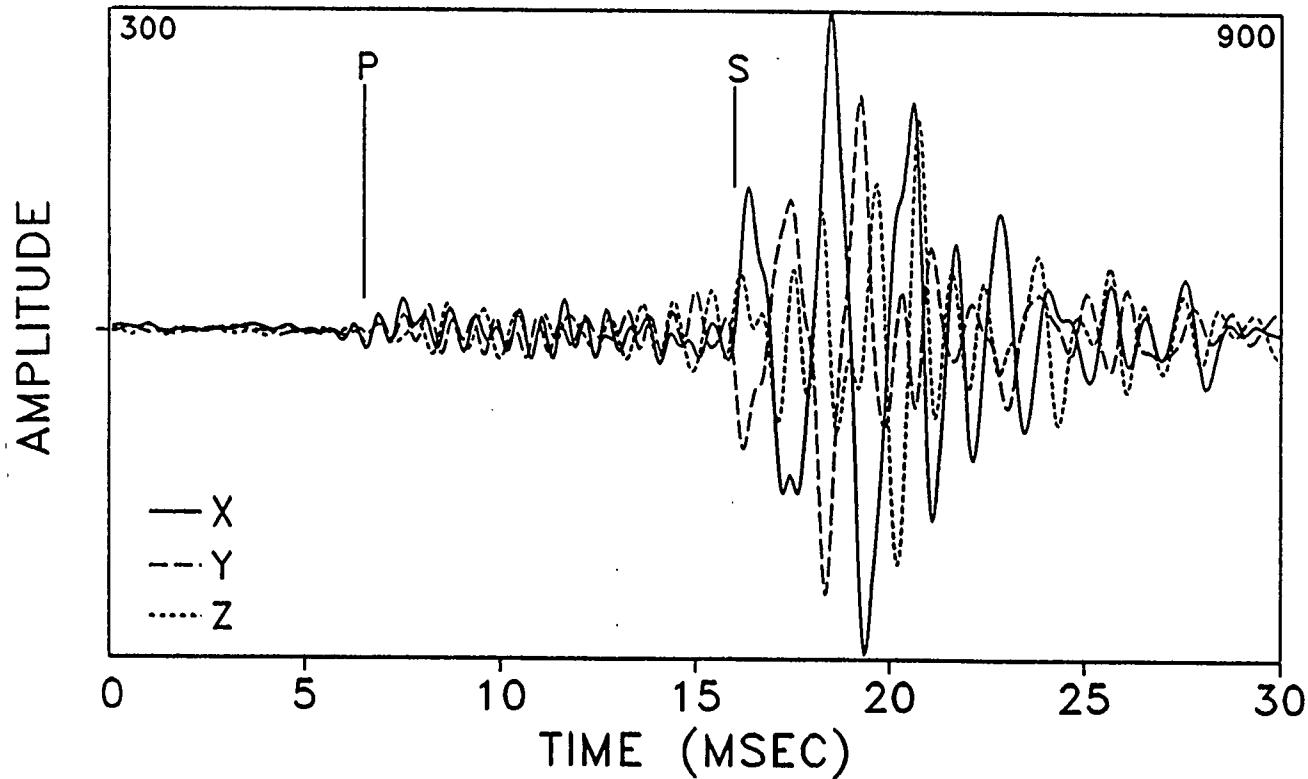
MWX-2
10/14/92
MS34.DAT
SCALE=76.7
SAMP INT:
0.050 ms
1200 PTS

Figure 46. Hodoaram for event 34. unfiltered

M-SITE SUITABILITY EXPERIMENT



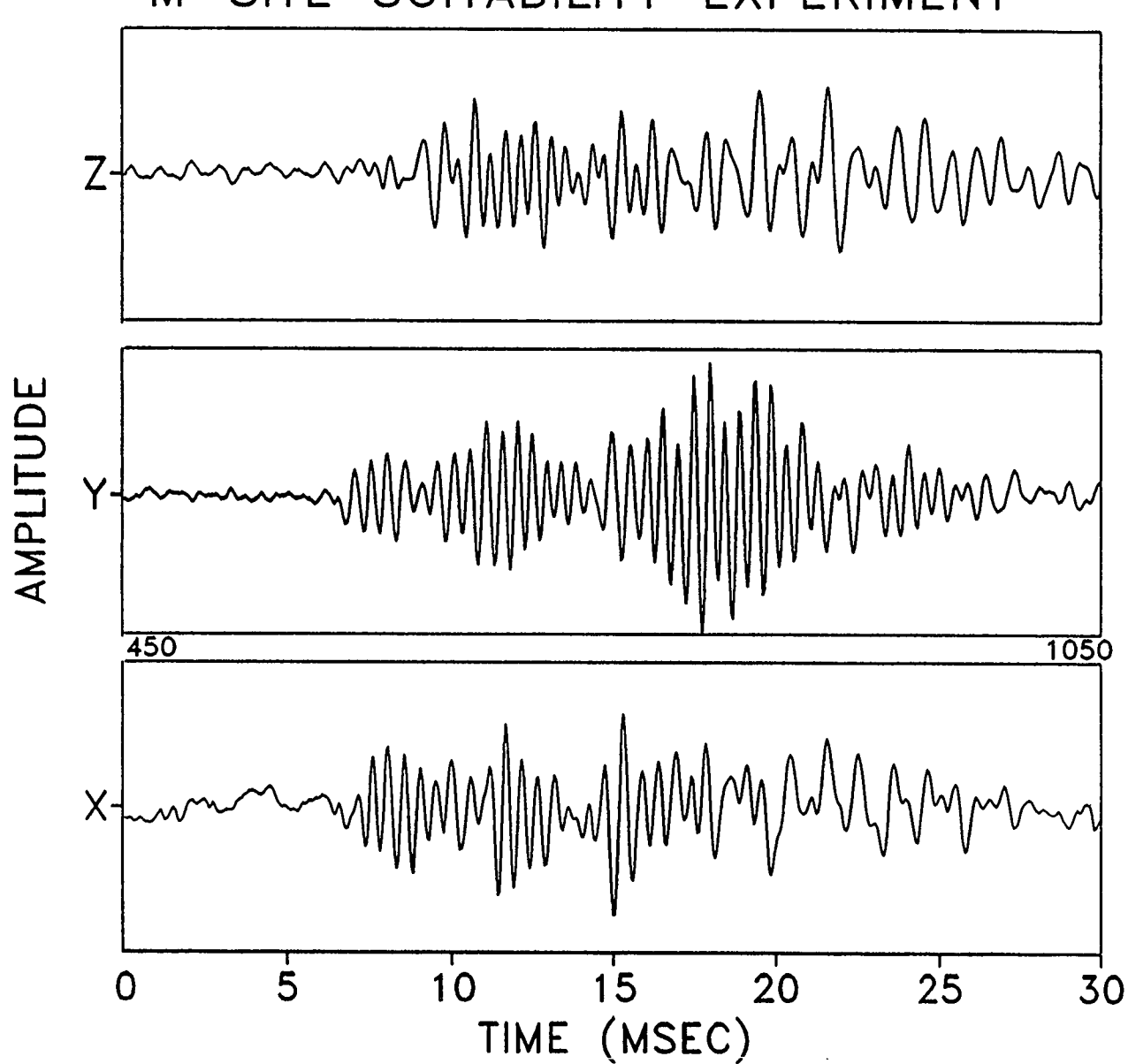
HODOGRAM
P: 430: 6.50 ms
TO 448: 7.40 ms
S: 620: 16.00 ms
H: 36.8 SD: 16.2
V: 16.3 SD: 17.8
RMS H: 37.5 V: 21.2
VEL FAC: 25.0
DISTANCE: 237



MWX-2
10/14/92
MSF34.DAT
SCALE=76.0
SAMP INT:
0.050 ms
1200 PTS

Figure 47. Hodogram for event 34, filtered

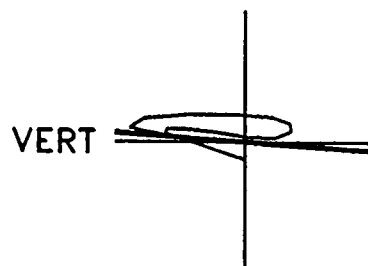
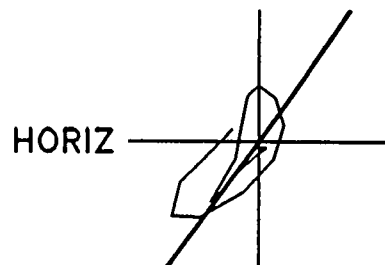
M-SITE SUITABILITY EXPERIMENT



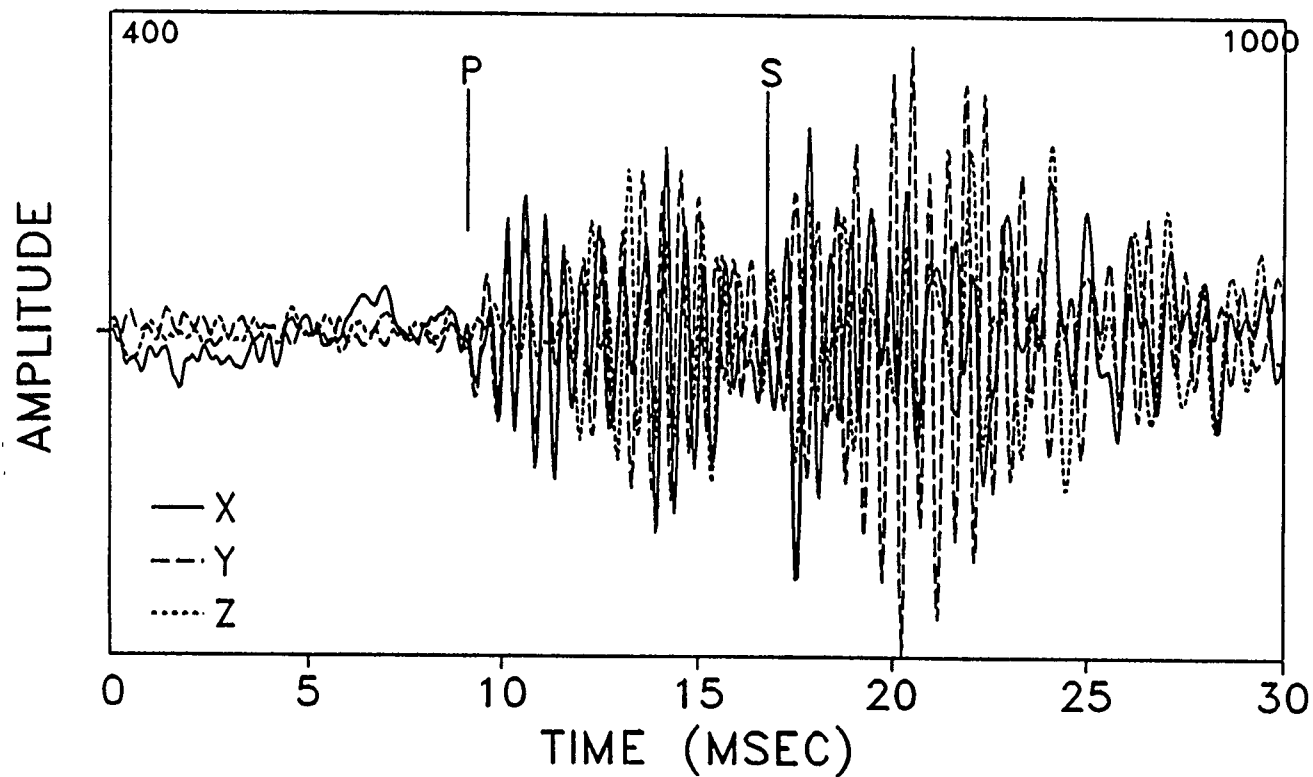
MWX-2
10/14/92
MS4.DAT
SCALE=8.8
SAMP INT:
0.050 ms
1200 PTS

Figure 48. Microseism traces for event 4. unfiltered

M-SITE SUITABILITY EXPERIMENT



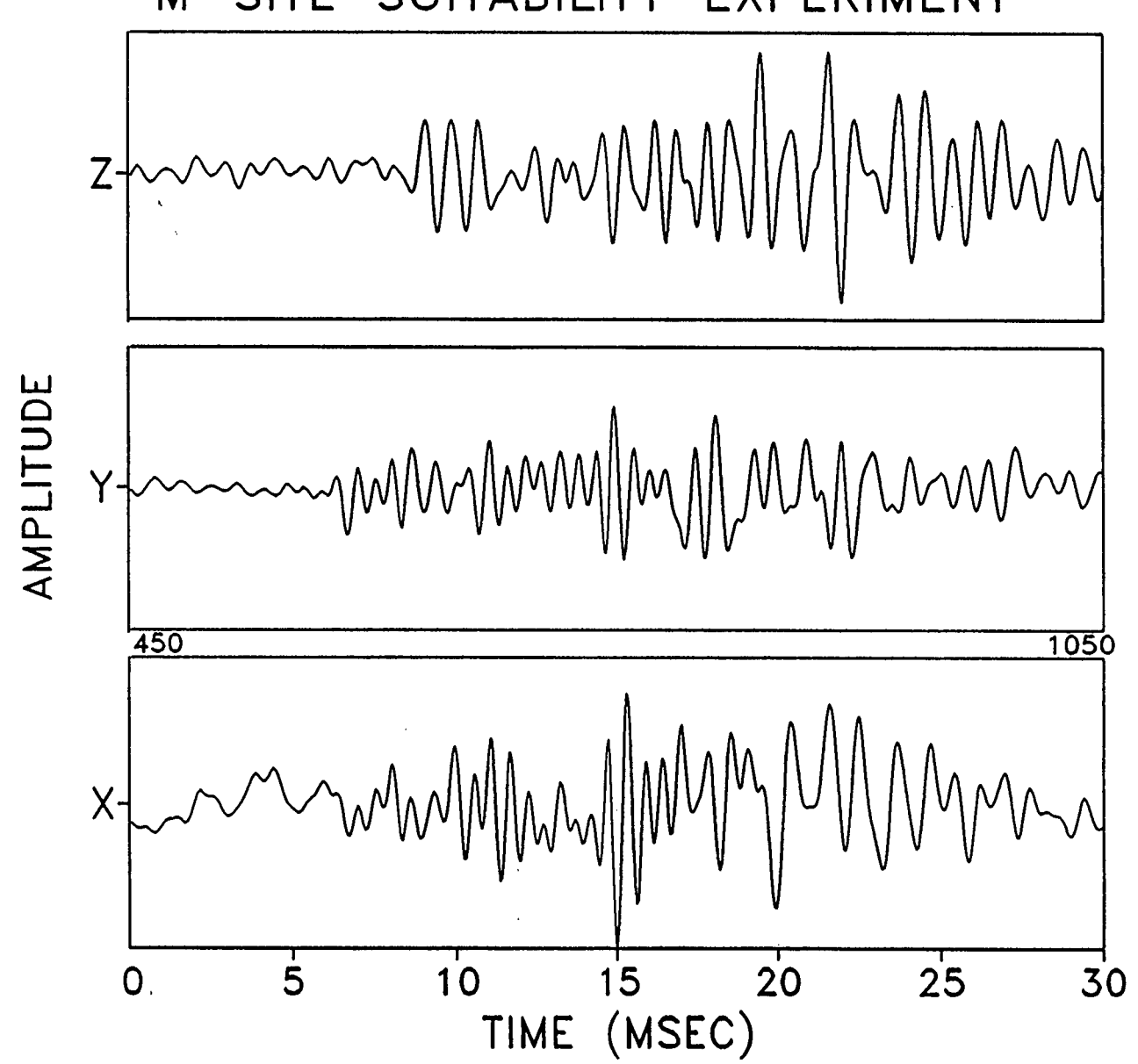
HODOGRAM
P: 582: 9.10 ms
TO 602: 10.10 ms
S: 735: 16.75 ms
H: 54.7 SD: 26.9
V: -4.1 SD: 22.3
RMS H: 49.7 V: 15.6
VEL FAC: 25.0
DISTANCE: 191



MWX-2
10/14/92
MS4.DAT
SCALE=8.8
SAMP INT:
0.050 ms
1200 PTS

Figure 49. Hodogram for event 4, unfiltered

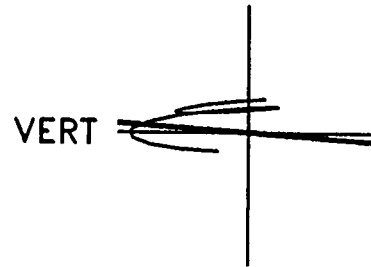
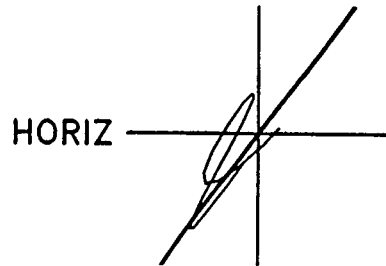
M-SITE SUITABILITY EXPERIMENT



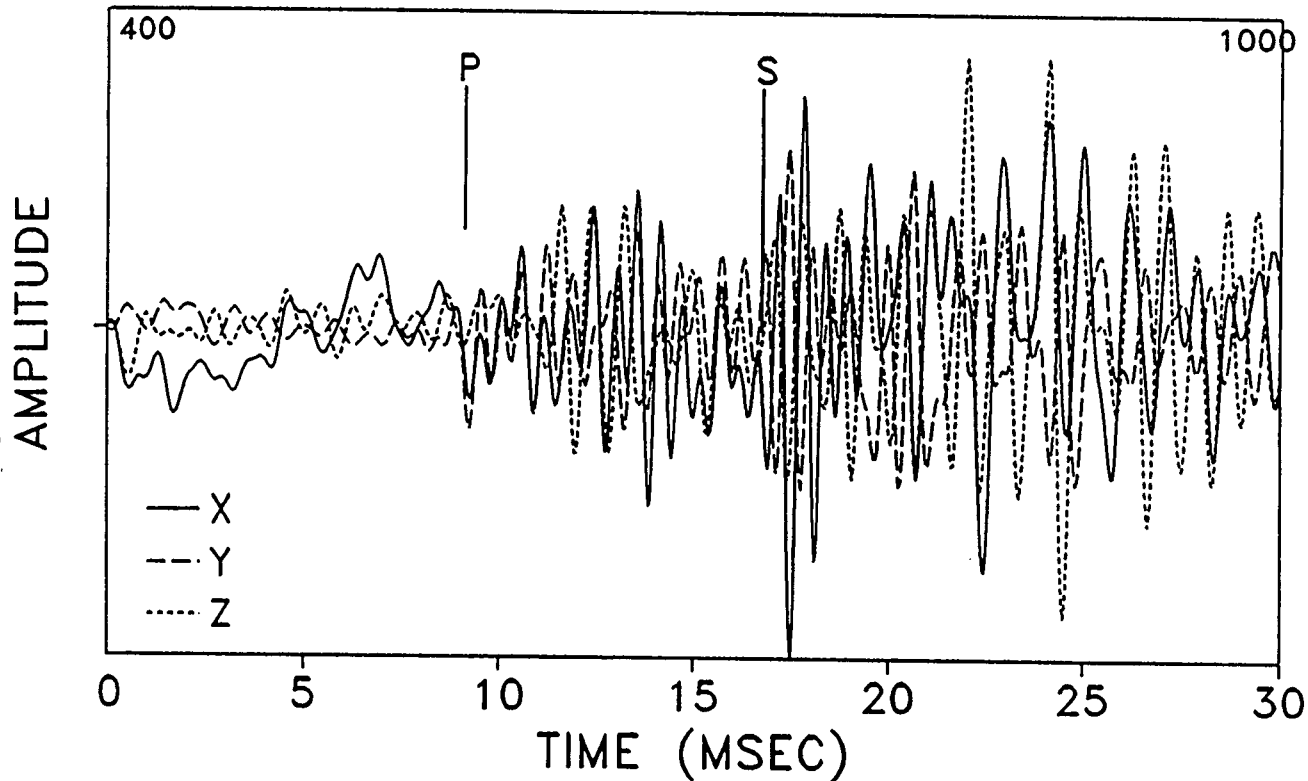
MWX-2
10/14/92
MSF4.DAT
SCALE=5.3
SAMP INT:
0.050 ms
1200 PTS

Figure 50. Microseism traces for event 4, filtered

M-SITE SUITABILITY EXPERIMENT



HODOGRAM
P: 582: 9.10 ms
TO 602: 10.10 ms
S: 735: 16.75 ms
H: 53.6 SD: 23.7
V: -4.0 SD: 29.5
RMS H: 52.2 V: 19.8
VEL FAC: 25.0
DISTANCE: 191



MWX-2
10/14/92
MSF4.DAT
SCALE=5.3
SAMP INT:
0.050 ms
1200 PTS

Figure 51. Hodogram for event 4, filtered

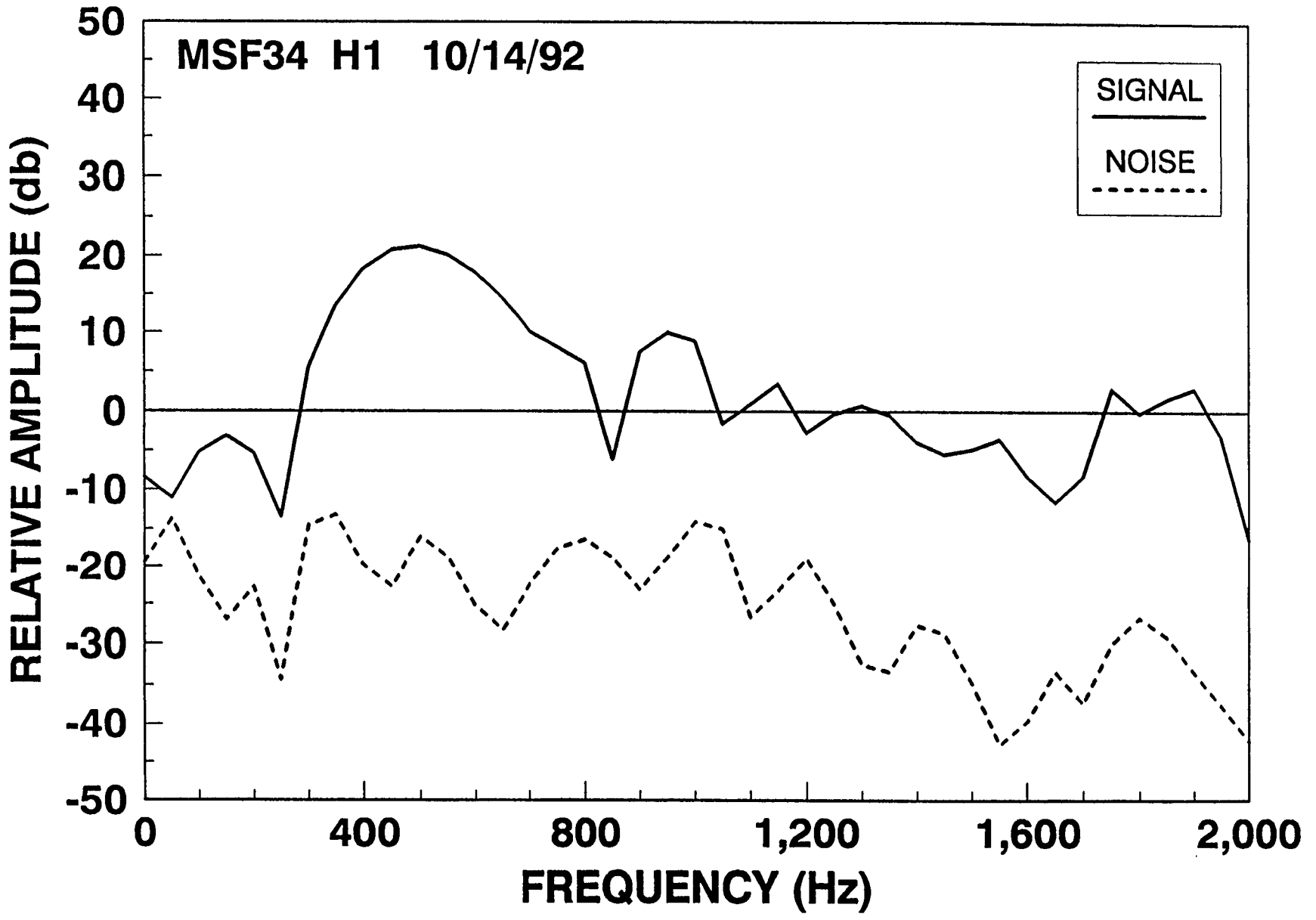


Figure 52. Spectral content for event 34, horizontal channel #1 (x)

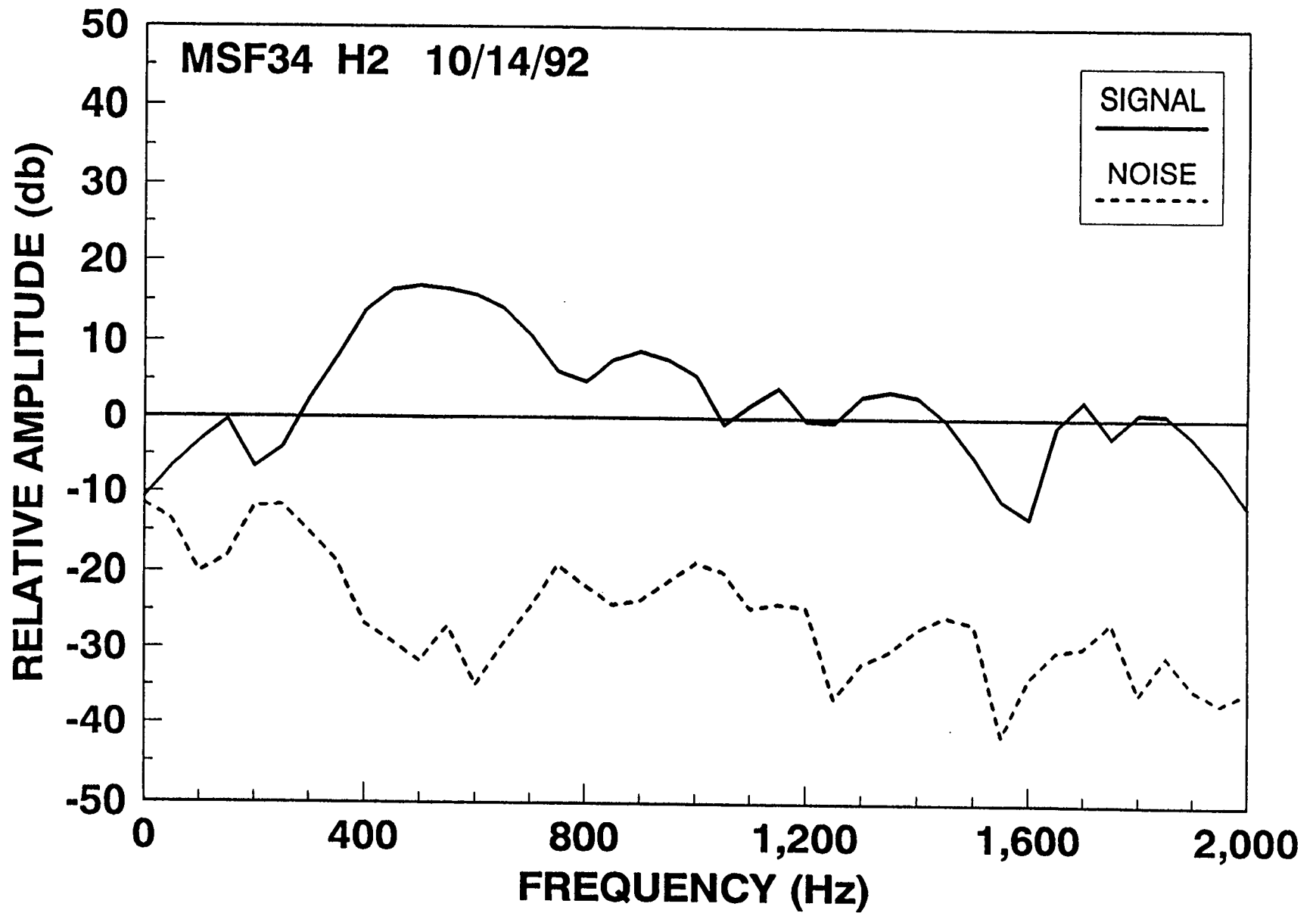


Figure 53. Spectral content for event 34, horizontal channel #2 (y)

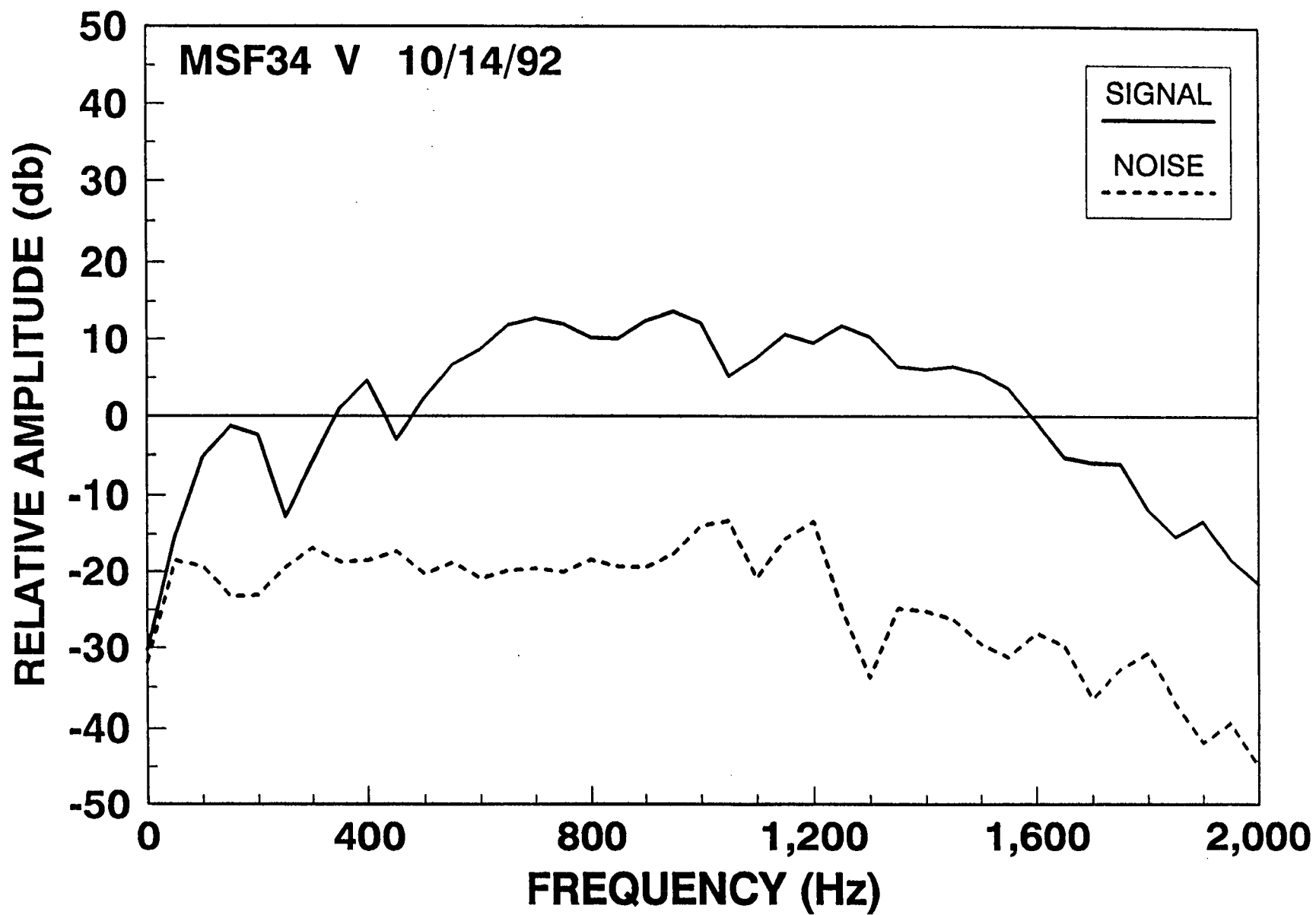


Figure 54. Spectral content for event 34, vertical channel (z)

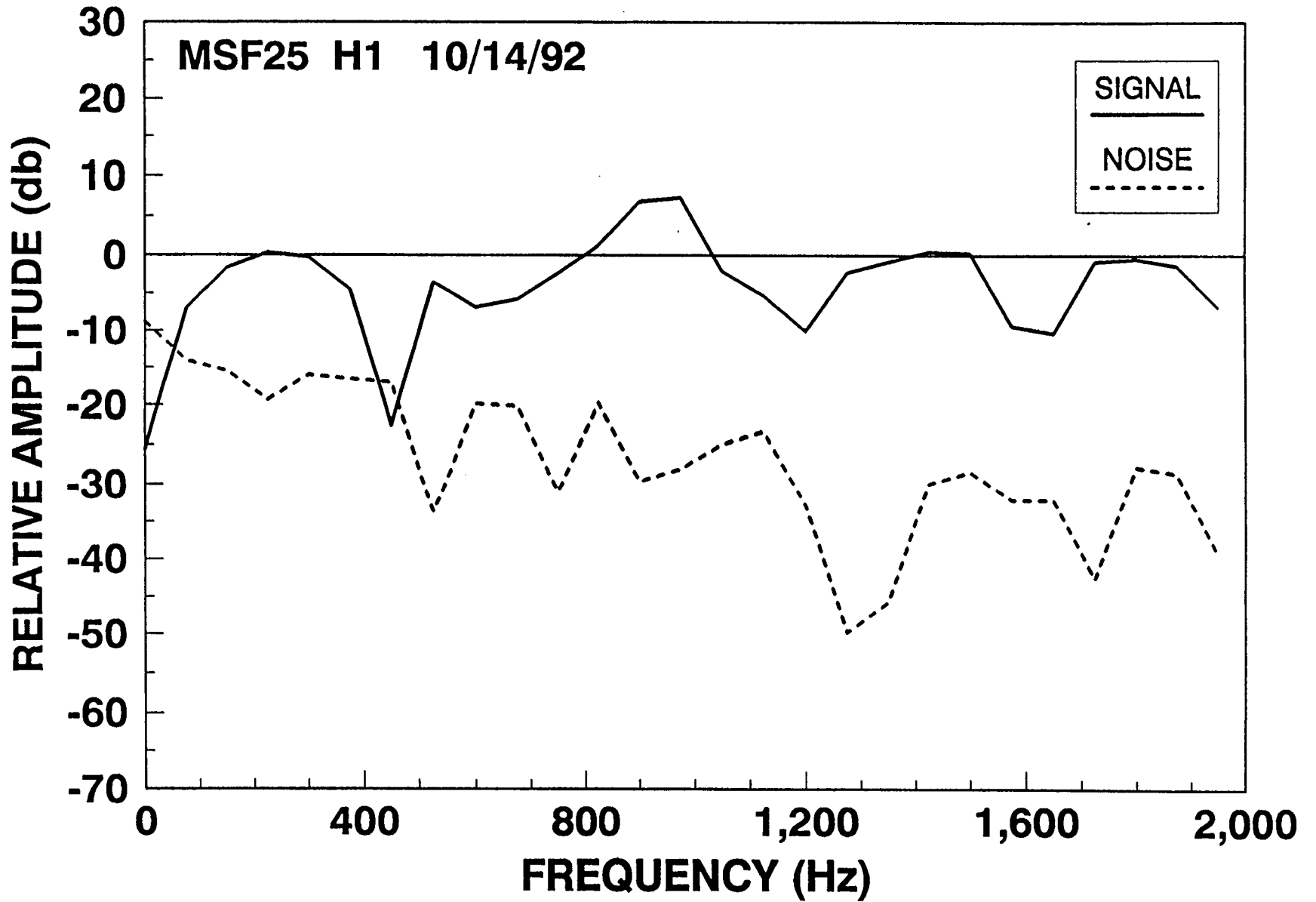


Figure 55. Spectral content for event 25, horizontal channel #1 (x)

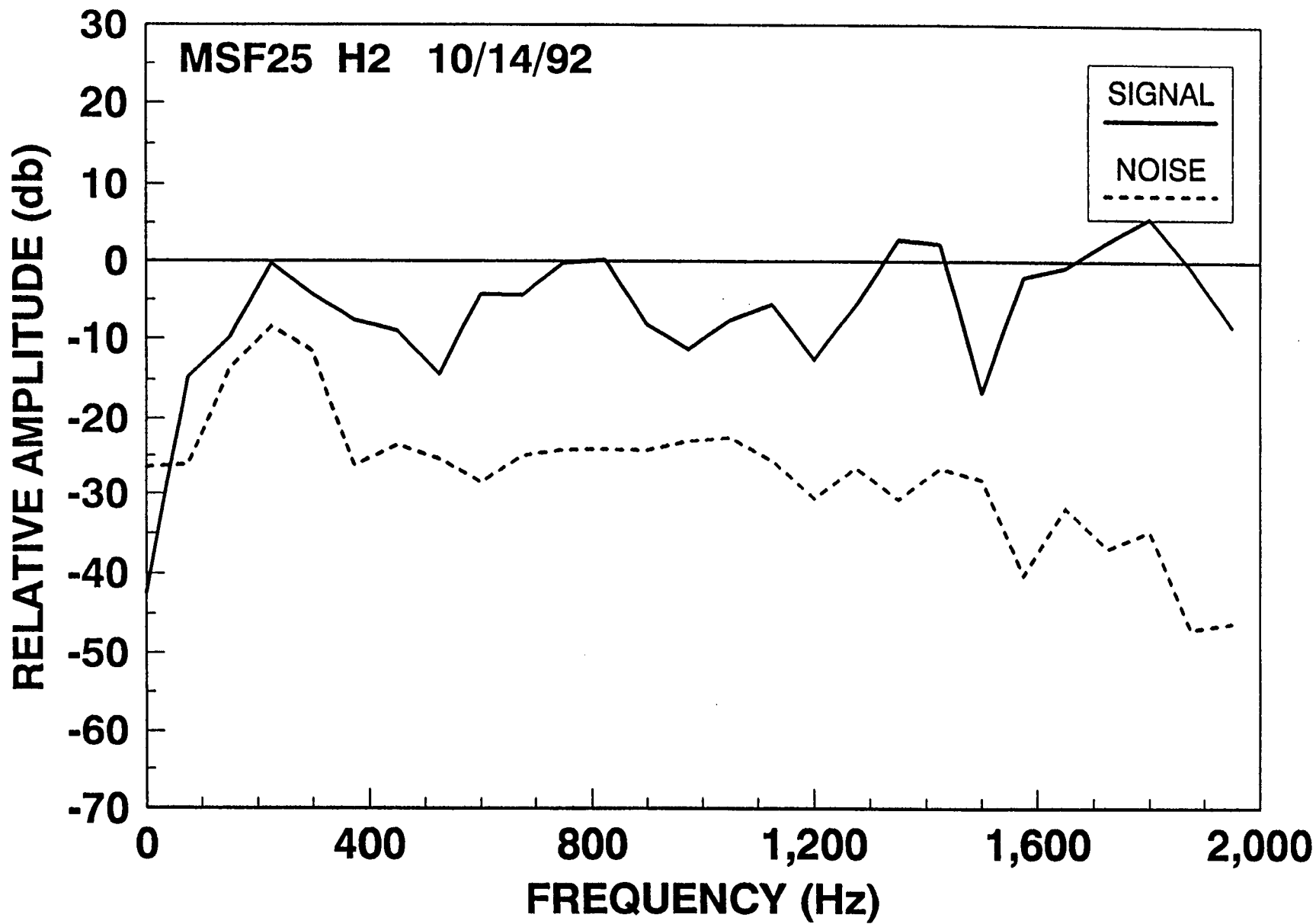


Figure 56. Spectral content for event 25, horizontal channel #2 (y)

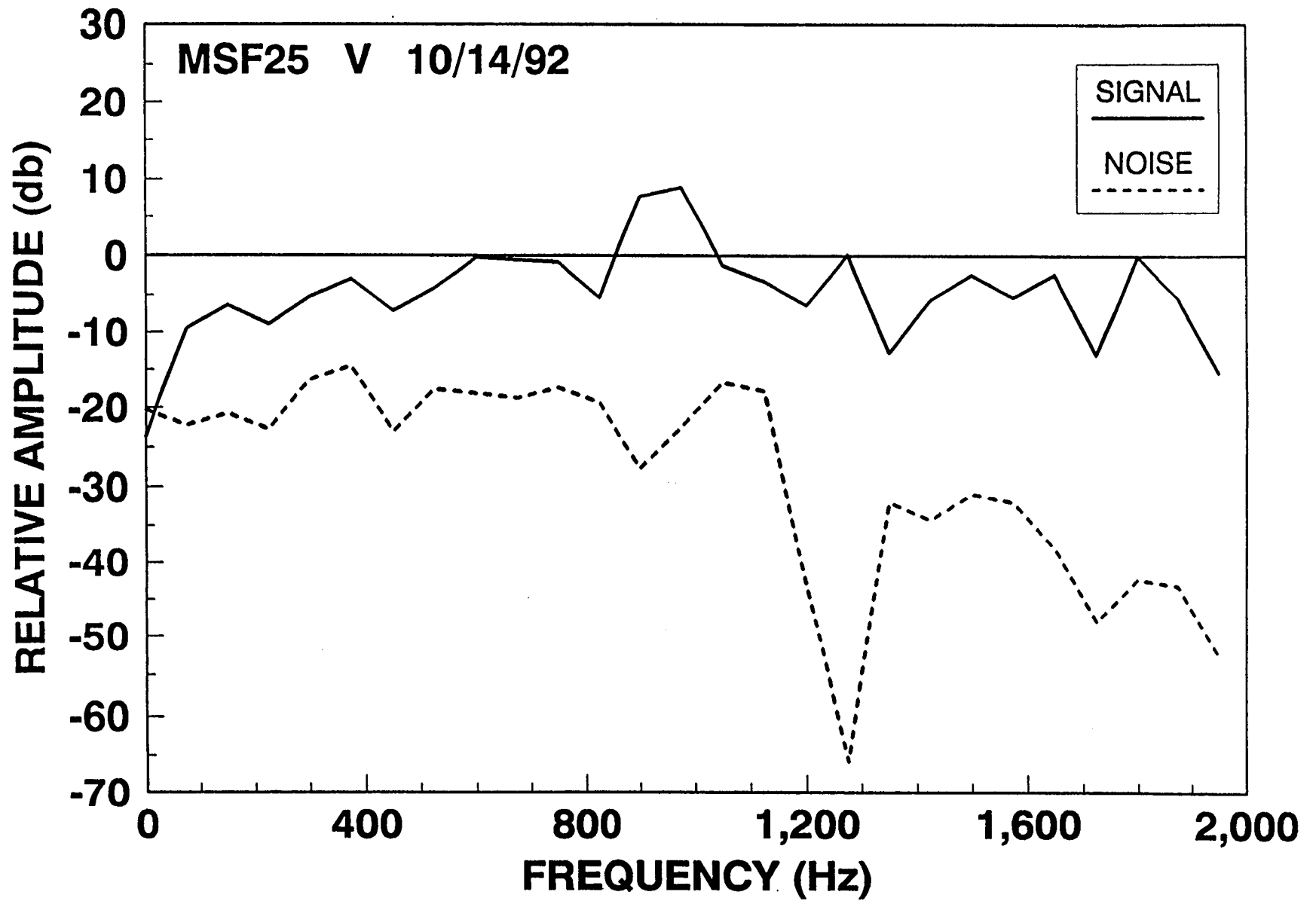


Figure 57. Spectral content for event 25, vertical channel (z)

THIS PAGE INTENTIONALLY LEFT BLANK